# Laser Cladding with metallic powders

**Simone Zanzarin**
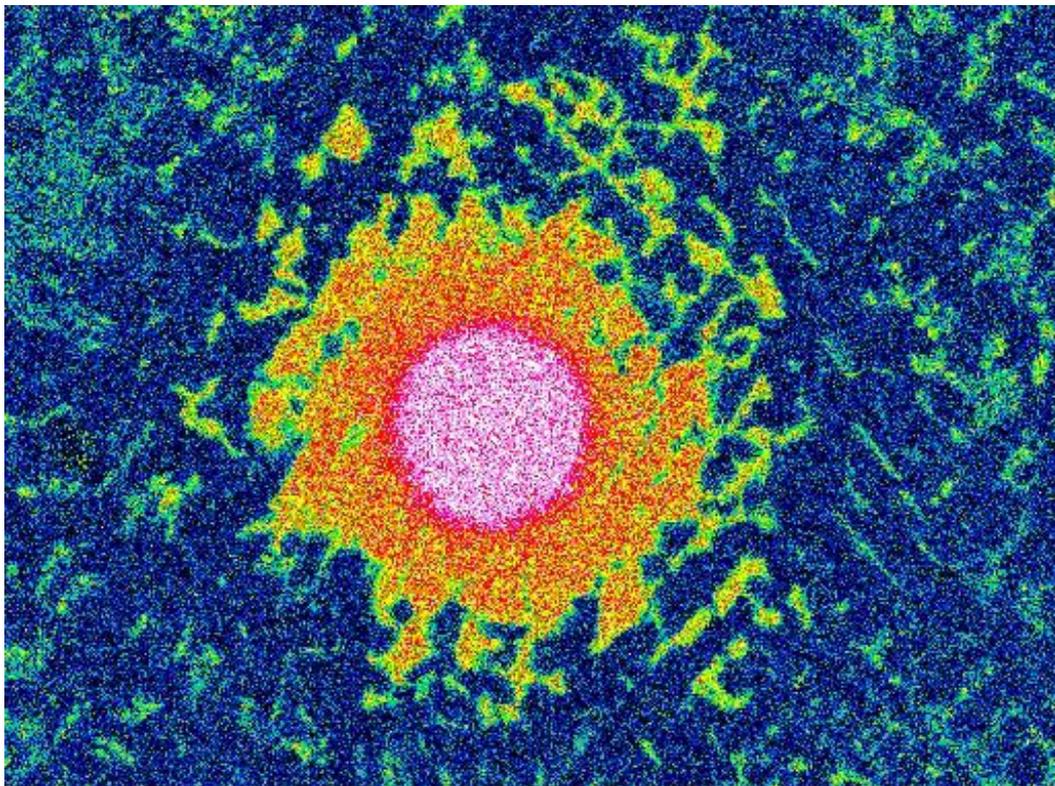
**November 2015**

# Laser cladding with metallic powder

**Simone Zanzarin**
E-mail: zanzarin.simone@yahoo.it

**Approved by:**

**Prof. Alberto Molinari, Advisor**
Department of Industrial Engineering
University of Trento, Italy.

**Ph.D. Commission:**

**Prof. Antonella Motta,**
Department of Industrial Engineering
University of Trento, Italy.


**Prof. Emanuela Cerri,**
Department of Industrial Engineering
University of Parma, Italy.


**Prof. Nuno M. Neves,**
Department of Polymer Engineering
University of Minho, Portugal.

**University of Trento**
**Department of Industrial Engineering**

**November 2015**

*To my family*

# Index

**Introduction**

**Chapter 1: Laser cladding**

**Chapter 2: Experimental procedures**

**Conclusions**

**Appendix**

# Introduction

Laser cladding is an emerging technology in the field of surface engineering. The high energy density, versatility and selectivity of the laser beam allow the production of high quality thick metallic coatings with fusion bonding to the substrate and low dilution. The characteristics of this technology enable also its application in rapid prototyping and component repairing.

The properties and thus the quality of laser cladding coatings are extremely sensitive to the choice of the laser cladding equipment, materials and process parameters and, consequently, since they are highly sensitive to the complex of the  physical phenomena occurring in the cladding process.

The definition of models for the description of the process and for the prediction of the characteristics of the coatings becomes thus fundamental.

For these reasons Höganäs AB, one of the world biggest powder manufacturer, and the Department of Industrial Engineering of the University of Trento started a cooperation to study and optimize the laser cladding process and the coating properties as a function of the powder characteristics and of the processing conditions.

With this aim, various metallic powders, and mixtures of metallic powders and hard reinforcement particles, have been employed to produce coatings with the High Power Diode Laser Cladding technology with coaxial powder injection. Three main processing parameters have been identified (laser power, scanning speed and feeding rate), and these parameters have been varied in an opportune operating window.

This PhD thesis can be divided into three parts. In the first part of the work, the influence of the powder material and the main processing parameters on geometrical features and dilution of the clads is investigated and discussed. Physical and analytical model that allow the explanation of the process and the prediction of the clad geometry and dilution is discussed. Using these models, useful tools for cladding operators and engineers are proposed.

In the second part of the work, the energetic balance of the process is presented. Energetic redistribution in laser cladding process is analysed in detail, and quantification of process efficiency and energy losses is given. The influence of the processing parameters and the chemical/physical properties of the materials is considered throughout the various experiments performed.

In the last part of the work, some selected properties of the coating produced in different processing conditions are analysed. In specific, the variation of the chemical composition of the clad due to substrate dilution is considered, and its effect on the characteristics of the coatings is discussed.

# Chapter 1

# Laser cladding

## 1.1 Introduction to laser cladding

Wear, together with corrosion and fatigue, are the three principal processes limiting the useful life of engineering products. They and their combined effect have annually a huge economic impact on industries since they cause maintenance, repair and material costs for part replacements as well as losses due to plant shutdowns. Moreover, to reduce and control wear and corrosion is important for other reasons, such as to extend the lifetime of machinery and bio-system, to make devices more efficient, to conserve poor material resources, to save energy and to improve safety. For these reasons, methods of reducing degradative phenomena have always been under development.

Historically these aims have been achieved in different ways: by design variations, selecting improved bulk materials or altering the material by alloying, by utilizing lubrication techniques to prevent wear, by changing the environment through desiccation and use of inhibitors or by cathodic and anodic protection against corrosion [1-3].

A possible solution to reduce wear, corrosion or fatigue is given by the field of surface engineering, which includes surface modification, alloying and coating methods. Surface is widely recognized as the most important part in many engineering components, since at the surface most failures originate, either by wear, fatigue or corrosion. Application of wear/corrosion-resistant coatings is up to now one of the most widely used means of protecting components, and has the advantage of changing the chemical composition of the surface. This allows designing composite systems made of coating and substrate having particular features:

- multi-material structures having performances which cannot be achieved by either the coating or the substrate alone (for instance, thermal barrier coatings);
- systems able to provide resistance against given service conditions having cheap and less noble base materials and more expensive and nobler coating alloys on the surface [1,2,4-7].

There is a wide variety of techniques to manufacture coatings, and proper selection can be based on their different features such us component size and accessibility, capital costs, productivity, energetic efficiency of the process, substrate and coating materials selection, pre- and post-treatments required, coating integrity, coating thickness attainable, bonding mechanism, processing temperatures, substrate distortion and so on. The coating processes can conveniently be divided, depending on the state of the depositing phase, into four generic groups: gaseous, solution, molten or solid (Figure 1.1).
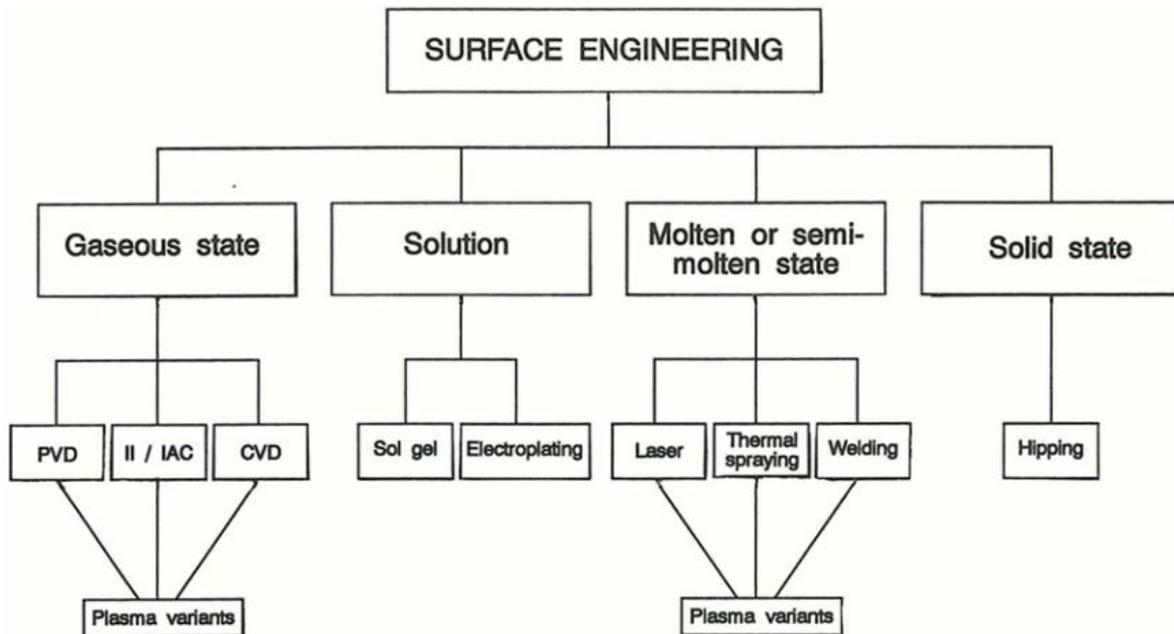
*Figure 1.1. Classification of surface engineering techniques depending on the state of the depositing phase [5].*

Another common way to classify these methods is based on the coating thickness they can produce: for instance, ion implantation, ion assisted coating, electroless and electrolytic plating, chemical and physical vapour deposition are common methods to produce thin films of a few micron thickness, whereas thermal and cold spraying, friction surfacing, electrochemical plating and overlay welding are representative methods to manufacture thicker coatings, having thicknesses ranging from a few hundred microns up to several millimetres (Figure 1.2).
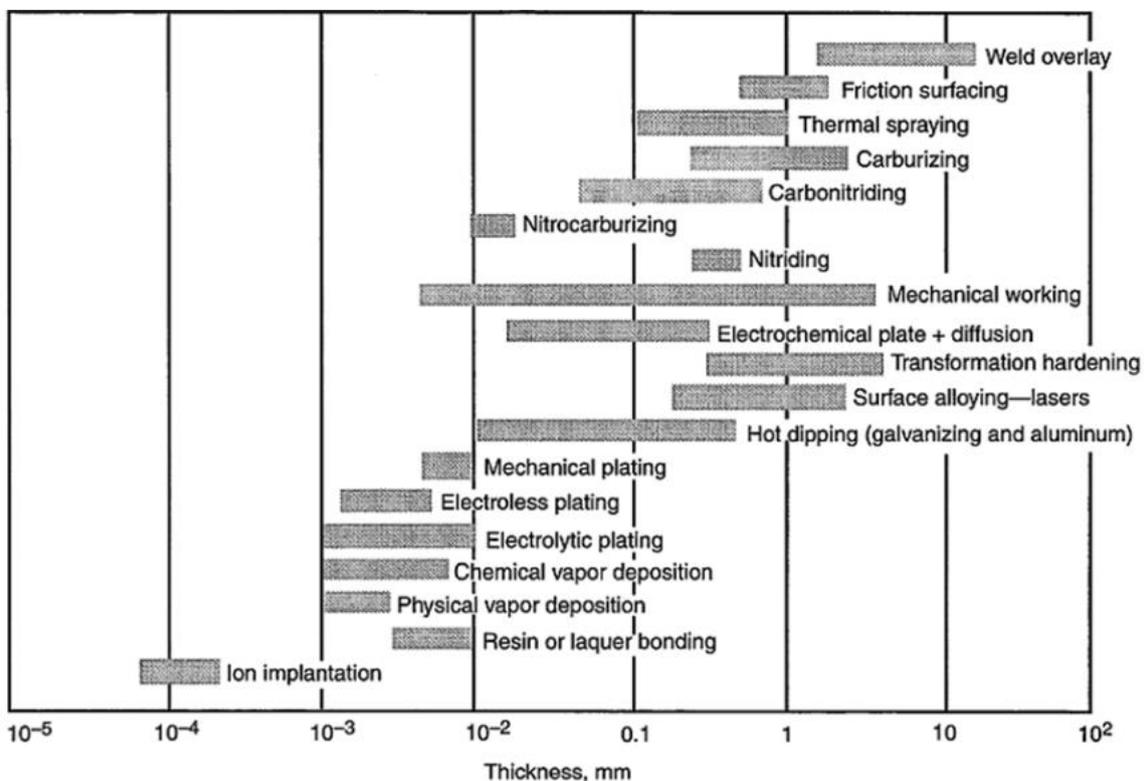


*Figure 1.2. Thickness ranges of various surface engineering treatments [2].*

3

This distinction is important to ensure the optimum performance of the coating: for instance, intense mechanical stresses are critical for thin layer, whereas they may be adequate to decrease friction coefficient and to resist corrosion and some form of wear; thick protective layers are usually preferred for high surface stress conditions or intense wear [1,2,5,7-9].

Belonging to the latter group, laser cladding has recently gained an increased importance in a variety of industrial sectors such as automotive, aerospace, navy, defence and many others.

Similar to overlay welding, laser cladding is a coating technique where a laser heat source is utilized to fuse and deposit a layer of a selected material on a substrate in order to form a defect-free protective coating, fusion bonded to the base material, with maximum coating material efficiency and minimum dilution (i.e. contamination due to the substrate material that has been melted and has mixed with the clad). The additive material can be deposited to the substrate by several methods: in form of powder or paste, that can be either injected during the process or pre-placed, or by wire/strip feeding. The process can be schematically described as follows: the laser beam scans the surface creating a melt pool with the fused coating material and, partially, the substrate material. Once laser irradiation stops or laser moves, solidification occur due to rapid heat transfer to the bulk and the coating is formed. During the process, a shielding gas is always used to protect the molten material from the atmosphere [8-12].

Compared to the conventional heat sources, the use of the laser allows to reach orders of magnitude higher energy densities, because a highly concentrated optical energy can be sharply focused on a well-confined zone of the surface of the base material. Owing to these characteristics, a very thin layer of base material is melted together with the coating material leading simultaneously to a controlled minimal dilution by the substrate and nevertheless a very strong fusion bonding between substrate and coating, which is a unique feature of laser cladding. The fusion bonding, together with the epitaxial growth of the coating microstructure from the substrate, guarantee excellent adherence. The use of a laser source causes other benefits: high energy density of the laser allows short interaction times between heat source and base material, leading to high solidification and cooling rates. High solidification and cooling rates generate fine grained microstructures which frequently contain non-equilibrium phases and supersaturated solid solutions, and limit both microsegregation and dissolution of externally added reinforcements. Distortion and metallurgical changes of the substrate are reduced due to the low heat input into the base material. Since the laser energy is applied locally, laser cladding is well-suited to the treatment of small areas, to repair tooling (especially on critical contacting surfaces), to produce functionally graded parts (for instance, thermal barrier coatings) by injecting different materials during the fabrication, and to create "smart structures" by embedding objects such as sensor and magnets during production [8,9,11,12].

Despite its advantages over conventional fabrication technologies, laser cladding presents also some drawbacks: the combination of the highly concentrated energy of the laser and high scanning speed generates strong thermal gradients, which make the production of crack-free coating with brittle material quite a hard task, due to generation of tensile residual stresses on the coating. Other disadvantages are the limited energetic efficiency of the cladding process due to the high reflection of laser light from the metallic melt pool surface, the high investment costs of the laser equipment and the lack of control over the cladding process, which is given by the high sensitivity of laser cladding to small changes in the operating parameters as well as to process disturbances [8,9,11,12].

From a historical point of view, the huge potential of laser cladding and similar techniques was reported in mid-70's, some years later the construction of the first working laser – the ruby laser – made in 1960 by Dr. Theodore Maiman. In fact, the first patent referring to laser cladding was published on April 1976 by the Avco Everett Research Laboratory [13]. The patent describes a method of applying a metal coating by the fusion of a metallic rod or wire through a laser beam. Later on, the

number of publications and patents regarding laser cladding in different forms (with wires, rods and pre-placed powders, with dynamical feed of wires and, few years later, with powder feeding) began to grow. Industry started to utilize laser cladding in early-80's: the first reported uses were hard-facing of Nimonic turbine blade interlock shrouds for the RB-211 jet engine at Rolls Royce (1981) and of nickel-base alloy turbines of JT8 and JT9 engines at Pratt and Whitney (1983) [14-17]. In the following years laser cladding technology was introduced in the automotive industry by companies such as Fiat, Toyota and Mercedes Benz for the engine valve seat coating, and was also used in components repair market (to re-build worn turbine vanes, tip of turbine blades and turbine bolts) and in rapid prototyping process (stereo lithography) [11]. Some important milestones in laser and laser cladding technology are reported in Figure 1.3.
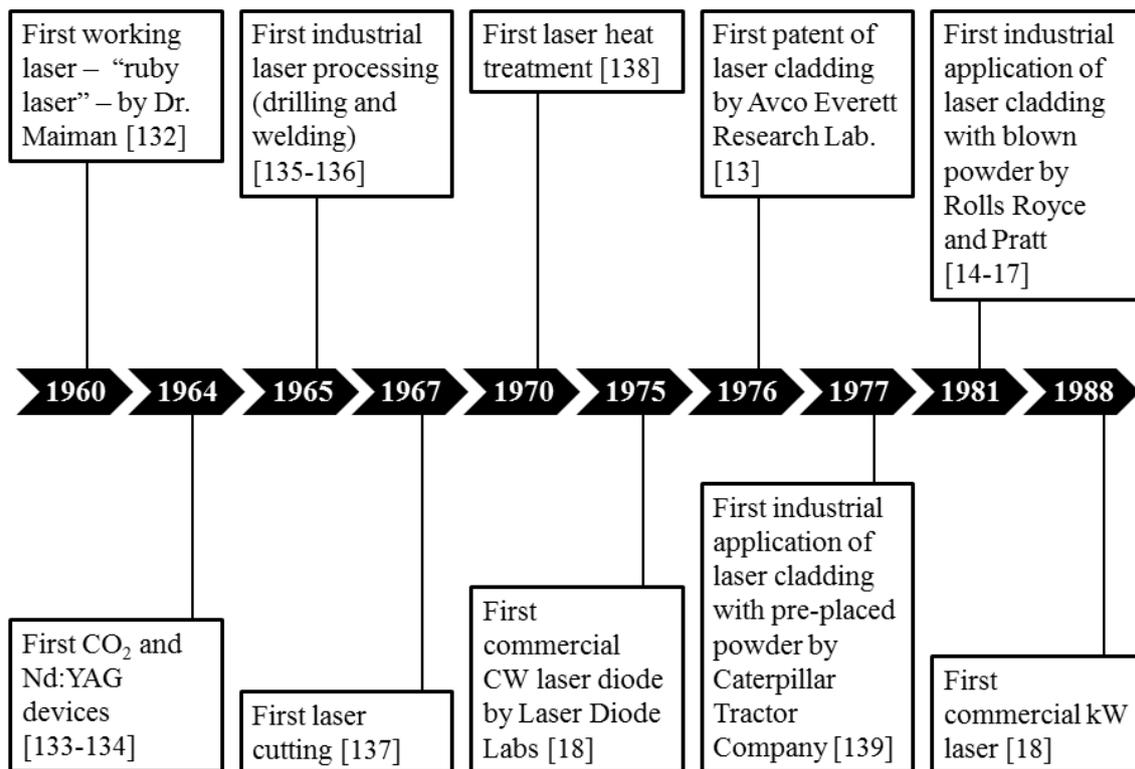


*Figure 1.3. Important milestones in laser cladding.*

In spite of these commercial applications, laser cladding did not receive wider industrial acceptance since the low productivity and the low energetic efficiency of the process, both of them due to the nature of the existing lasers. However, with the developments of the new lasers, more powerful (in the range of kilowatt and more) and with shorter wavelength, situation has changed and laser cladding research grew exponentially [11,18]. In particular, high-power diode lasers showed the great potential of increasing the productivity and the cost efficiency in laser cladding processes thanks to their advantages over other laser system, such us low price, small size, high efficiency, mobility and so on. Because of the always increasing demand for high-quality coatings, which is caused by harsher service condition in industrial processes and environmental restrictions, developments in the laser cladding technology are expected to continue with more powerful and new potential laser sources (for instance, HPDL and fibre laser), novel hybrid laser cladding methods and sophisticated knowledge-based controllers.

Nowadays, laser cladding applications are the production of surface coatings, the production of entire components (rapid prototyping and tooling) and the repair and the refurbishment of damaged parts (Table 1.1).

*Table 1.1. Industrial applications of laser cladding.*

| reference | year | material | application |
|---|---|---|---|
| | | coatings | |
| [38] | 1988 | Inc625 – CrC | gas turbine airfoil thermal barrier |
| [38] | 1988 | AISI 410 | valve seat |
| [38] | 1988 | Stellite6 | seal runner |
| [38] | 1988 | Stellites | gate valve |
| [39] | 1990 | YPSZ, YPSZ – $Al_2O_3$ | gas turbine engines |
| [40] | 1992 | TiC – 90MnCrV8 | tools and moulds |
| [41] | 1993 | Ni-base superalloys | turbine entry temperatures (TETs) |
| [42] | 1993 | WC – 20Ni4Mo | teeth of rock bids, cutting tools |
| [43] | 1997 | Ni-base alloys | mining machine parts |
| [44] | 1998 | Zn – Al | propeller and drive shafts, engine components |
| [45] | 2000 | Al – Ti | cutting tools, inserts, diffusion barriers in semiconductor technology |
| [46] | 2002 | Al – Cu alloy | automotive industry |
| [47] | 2003 | Ni – $Cr_3C_2$ | well drilling and oil extraction equipment |
| [48] | 2005 | Al/Si – TiC | automotive industry |
| [49] | 2009 | Cr – $CrB_2$, Mo – MoB | automotive, aerospace, paper and plastic industries |
| | | multi material fabrication | |
| [19] | 2000 | Cu – Ni | building block for temperature-insensitive structures |
| [23] | 2003 | TiC – Ti | propulsion system and airframe of space planes |
| [24] | 2003 | Cu – Ni | engine components, ceramic turbine components, direct metal tools, biomaterials in artificial human implants, drug delivery devices, armour and armament components |
| [25] | 2005 | 316L – Stellite12 | 3D objects |
| [22] | 2005 | H13 – Ni/Cr alloy – TiC | mould inserts |
| [26] | 2007 | 316L – Stellite12 – FeCu – WC/Co – CuSn – bronze | elements of cooling systems in International Thermonuclear Experimental Reactor (ITER) |
| | | solid freeform fabrication | |
| [20] | 1996 | 316L | injection moulding tools |
| [34] | 1997 | H13 tool steel | moulds and dies |
| [33] | 1998 | CPM 15V tool steel | rotary cutting dies |
| [29] | 1998 | Ni-base superalloy | airfolds |
| [21] | 1998 | 316L | blade integrated disks |
| [30] | 2000 | Ni-base superalloy | airfolds |
| [27] | 2000 | Ti6Al4V | large aerospace components |
| [28] | 2002 | Ti6Al4V | hollow motorcycle engine stems |
| [32] | 2002 | CPM 9V tool steel | rotary cutting dies |
| | | refurbishing | |
| [21] | 1998 | Ni-base superalloy | turbine blade |
| [21] | 1998 | Stellite6 | torsion shafts |
| [21] | 1998 | Al – Si | cylinder heads and blocks |
| [21] | 1998 | Stellites | injection moulds and extruder parts |
| [21] | 1998 | Rene 80, Inc625 | turbine parts |
| [21] | 1998 | 316L | turbine blades |
| [37] | 1999 | Ni-base superalloy | turbine blade |
| [30] | 2000 | Ni-base superalloy | turbine blade |
| [36] | 2002 | Ni-base superalloy | turbine blade |
| [35] | 2002 | WC – NiCrB | oilfield and forestry industries |

The leading metallic coating application is the coating of commercial aircraft gas turbines. It has been used also in the sector of spacecraft components and for the production of surfaces for industrial parts, such as shafts used in drilling tools, engine valve seats, tool hardfacing, hydraulic pump components and moulds [11]. Multi-material fabrication has also been achieved with laser cladding process: examples of produced functionally graded materials with special functionalities are structure with overall negative coefficient of thermal expansion, injection moulding tools with embedded copper heat sink and other particular structures [19-26]. Regarding the solid freeform fabrication, different types of components, ranging from thin-walled structure to highly complex bulk objects, have been produced, including large aerospace components, hip implants and hollow motorcycle engine steams, airfoils, injection moulding tools, blade integrated disks, injection moulding dies and rotary cutting dies [20,21,27-34]. Parts repair and refurbishing, which is one of the major application of laser cladding, has been principally done on damaged turbine blades. Other repaired components with this technique are moulds and engine cylinder heads and blocks [30,31,35-37].

## 1.2 Lasers for laser cladding

Laser materials processing involves a broad range of power densities, interaction times and transport phenomena. Figure 1.4 presents operational regimes and associated transport phenomena for various processing techniques, [50-52].
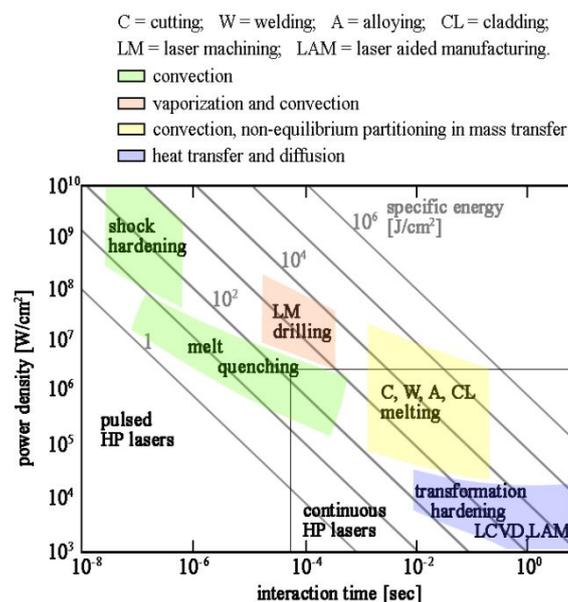


*Figure 1.4. Process map for various laser applications in materials processing [50].*

To perform laser cladding process, the fusion of the coating material and of a thin layer of substrate while avoiding evaporation is needed. Thus, it is necessary to guarantee the proper amount of power density and interaction time. These requirements limit the types of laser that can be used. Among the many laser systems available on the market, the most commonly used in the laser cladding process are $CO_2$ lasers, lamp-pumped Nd:YAG lasers, diode-pumped Nd:YAG lasers and high-power diode laser

(HPDL). In the last decade, fibre laser have also been adopted. Table 1.2 summarizes the most important characteristics of the commonly used laser in laser cladding [11,53-56].

*Table 1.2. Important characteristics of the commonly used laser in laser cladding.*

| characteristics | $CO_2$ | Nd:YAG lamp-pumped | Nd:YAG diode-pumped | HPDL | fibre |
|---|---|---|---|---|---|
| wavelength [µm] | 10.64 | 1.06 | 1.06 | 0.65 – 0.94 | 0.34 – 2.10 |
| wall-plug efficiency [%] | 5 – 10 | 1 – 4 | 10 – 12 | > 50 | > 30 |
| maximum power [kW] | 45 | 4 | 5 | 15 | 50 |
| average power density [W/cm²] | $10^6 – 10^8$ | $10^5 – 10^7$ | $10^6 – 10^9$ | $10^3 – 10^5$ | $10^6 – 10^{10}$ |
| service period [hour] | 1000 – 2000 | 200 | 5000 - 10000 | 5000 - 10000 | 100000 |
| beam parameter product [mm·mrad] | 12 | 25-45 | 12 | 100 – 1000 | 0.3 – 1.1 |
| fibre coupling | no | yes | yes | yes | yes |

$CO_2$ lasers are relatively inexpensive. They have good beam quality, which is expressed by the low value of the beam parameter product (BPP), and can provide very high power. The principal drawback of $CO_2$ lasers is the light emission wavelength (10.64 µm), that is longer than the wavelength of Nd:YAG and HPDL light: this causes technological and economical limits. As shown in Figure 1.5, the interaction between metals and the laser light is function of the laser wavelength: in specific, metals are less absorptive at 10 µm than at 1 µm.
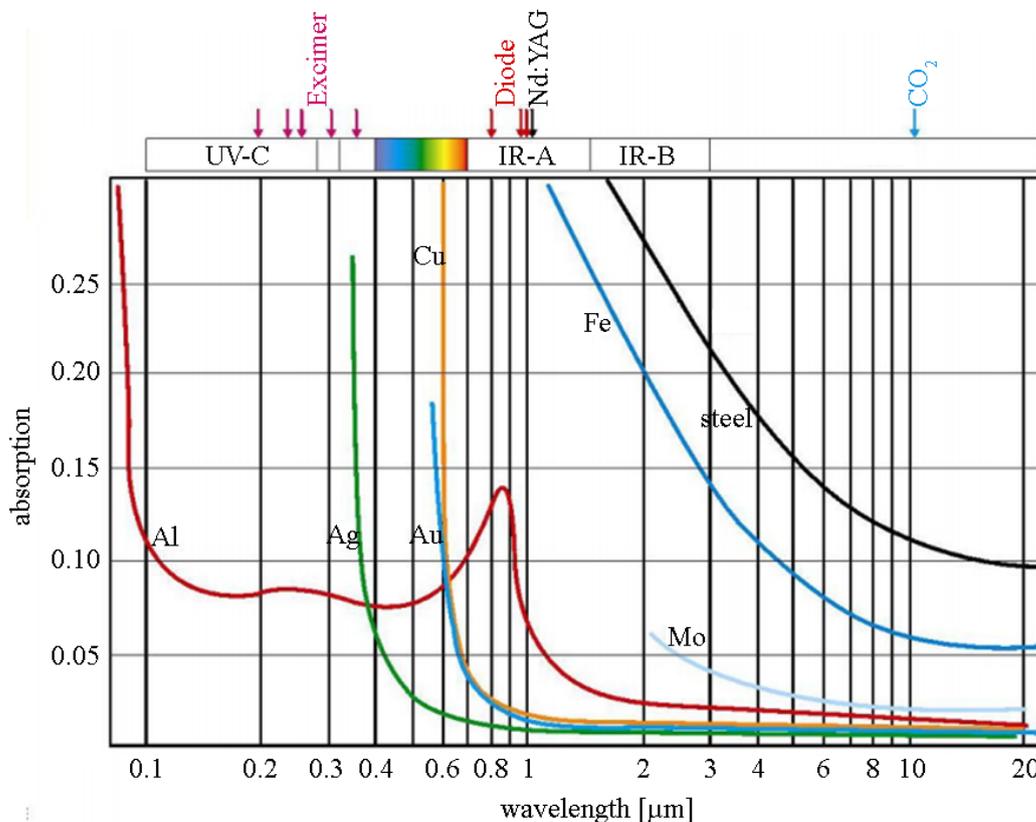


*Figure 1.5. Correlations between laser absorption and beam wavelength for different metals.*

This leads to a limited energetic efficiency of the process $(5 - 25\%)$. Moreover, due to its wavelength the laser beam delivery through a fibre optic cable is not possible. As a result, the manoeuvrability of a motion system along with a $CO_2$ laser is limited and its use for the production of complex part is restricted [11,57].

Nd:YAG solid-state lasers have shorter wavelength $(1.06\ \mu m)$. Lamp-pumped Nd:YAG laser is a relatively inexpensive type of laser with a power range up to 4 kW. In comparison with $CO_2$ lasers, fibre-coupling is possible, and the energy absorption by the metallic melts reaches values up to 60%. The disadvantages regarding efficiency and beam quality have been solved by another type of Nd:YAG solid-state laser, using laser diodes for excitation. The wall-plug efficiency of diode-pumped Nd:YAG lasers ranges from 10% to 12%, and the beam quality is also improved considerably. The technical parameters of these systems correspond to those of the $CO_2$ laser, but with the advantage of the fibre-coupling and the improved absorption. The main disadvantage of the diode-pumped Nd:YAG laser is the significantly higher price compared to $CO_2$ laser [11,57].

High power diode lasers (HPDL) are particularly compact and with their characteristic hat profile of power distribution, they are tailored for laser cladding applications. HPDL beam has low beam quality, but its cross-section can have different shapes (round, rectangular and linear). Both the wall-plug efficiency and the energy absorption by the melt-pool can be higher than 50%. Compared to a same power output $CO_2$ laser, the deposition rate can be higher. [58]. Since the costs per kilowatt of laser power are much lower compared to those of the diode-pumped Nd:YAG and the $CO_2$ lasers, high power diode lasers are the preferred tool for laser cladding.

The latest generation of lasers are fibre lasers. These solid-state laser are in the power range up to 50 kW and their features are high beam quality and a focus diameter of about 10 μm, high brightness, irradiation mode easy to pulse, high efficiency and moderate investment costs [57].

## 1.3  Laser cladding process

As discussed in the previous paragraph the interaction between laser and material leads to different processes (Figure 1.6).
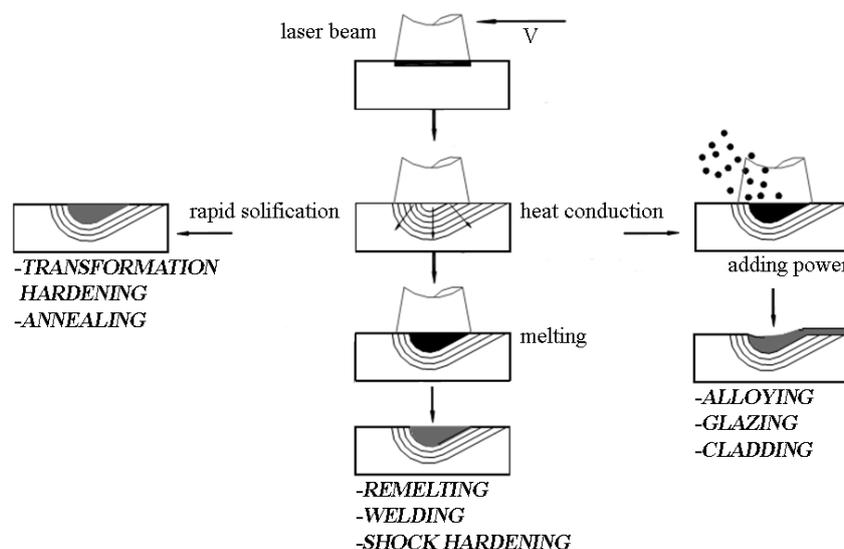


*Figure 1.6. Schematic of different laser material processing techniques [11].*

Laser transformation hardening, laser remelting, laser welding and laser shock hardening are based on a microstructural change of the surface layer. Alternatively, in laser cladding and alloying the addition of the coating material to the melt pool generates a coating layer called "clad" with a different chemical composition on the top of the base material. Chemical composition and features of the clad depend on type and amount of material added, as it can be seen in Figure 1.7.
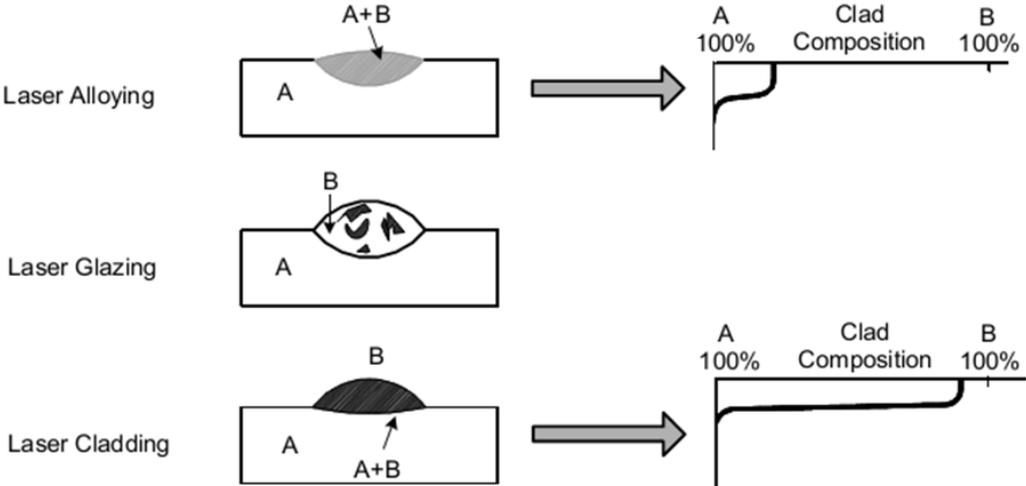


*Figure 1.7. Different microstructures and chemical compositions of laser alloying, glazing, and cladding [11].*

In laser alloying, only a small amount of filler material is fed into the melt pool. For this reason, a complete and homogeneous mixing of additive and base material throughout the melt region is achieved. Laser cladding is similar to laser alloying, except that dilution by the substrate is minimized and much more addition of filler material to the substrate surface is required. The additive material can be deposited to the substrate principally by two methods: by fusing the additive material already pre-placed on the surface of the base material (two-step process) or by feeding it dynamically to the laser-generated melt pool (one-step process) (Figure 1.8).
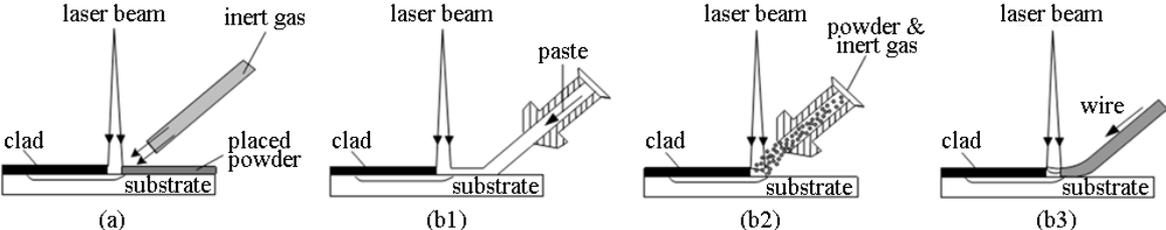


*Figure 1.8. Different methods of laser cladding: (a) two-step laser cladding, (b) one-step laser cladding with (b1) paste, (b2) powder injection and (b3) wire feeding [11].*

## 1.3.1 Two-step laser cladding process

In a two-step laser cladding process, the first step consists in the deposition of the coating precursor on the substrate material, while the second step consists in the melting of the pre-placed layer through laser irradiation. The precursor material can be supplied in different forms: powder or paste, wire,

chip, strip or foil, etcetera [8,11]. Among these, laser cladding with preplaced powder is one of the simplest and most common method [51]. Powders are usually applied in form of slurry made of powder, water and a binder, which is often an alcohol (for instance PVA). The purpose is to guarantee both powder agglomeration and a good bonding between the pre-placed powder layer and the substrate. This prevent the removal of the powder particles due to the inert gas flowing during the second step of the process and thus ensures the good quality of the final coating. Water and organic binder evaporate by drying process at elevated temperature and by laser melting process respectively. This may cause porosity in the final coating [8]. Alternatively, powder pre-placing can be accomplished by some conventional coating technique such us thermal spraying or electroplating [8].

The physical process of laser cladding with pre-placed powder has been widely described in literature [51,59-61]. As shown by Powell [60], when laser irradiation begins the surface powder particles start to heat up, but no heat conduction is allowed between particles due to the limited interparticle contact. Subsequently, the irradiated particles melt and, in the molten state, they can conduct heat to the neighbouring particles: this allows the molten front to propagate through the insulating powder layer (Figure 1.9,a). Once the melt touches and wets the substrate (Figure 1.9,b,c,d), the chilling effect of the substrate leads to a reversal in the melt front propagation. As a result, solidification of the melt begins (Figure 1.9,e) but the melt-liquid interface does not propagate into the body of the substrate unless additional laser power and/or interaction time are provided. If the laser source continues to irradiate the surface of the melt, the energy delivered might be enough to move the melt-solid interface back down through the clad layer and across into the body of the substrate (Figure 1.9,f) [61]. The final depth of the melt front is thus representative of the dilution of the cladding material.
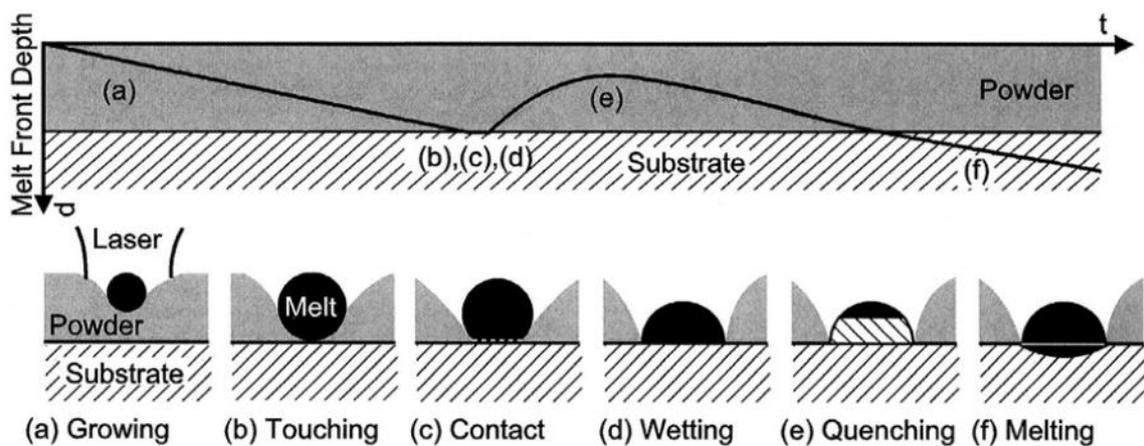


*Figure 1.9. Contact history between melt, powder and substrate [61].*

Figure 1.10 shows the variation of the melt front depth as a function of time for different laser powers: on increasing the laser power and on increasing the interaction time, which means decreasing the scan speed, the depth of melting (i.e. dilution) increases. However, it is rather difficult to provide the proper amount of power or time in order to achieve fusion bond and to prevent excessive dilution [51,62].

Even if this technology guarantees a high material efficiency, energetic requirements of the pre-placed powder method are much higher than those for the blown powder technique, as stated by Mazumder and Li [59]. For these reasons, together with the fact that two steps are needed, one-step laser cladding process is usually preferred.
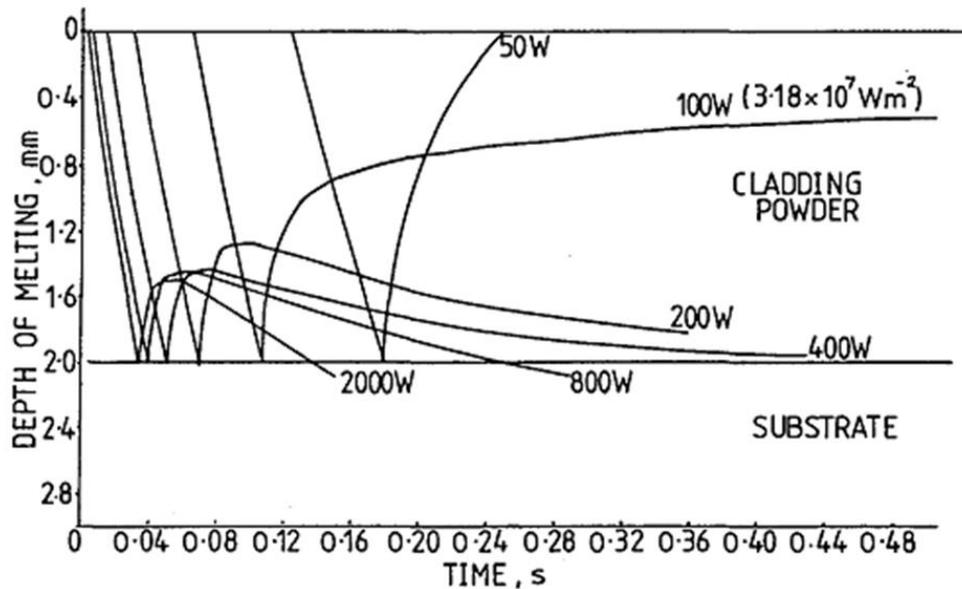
*Figure 1.10. Movement of molten front with time at various laser powers [60].*

## 1.3.2 One-step laser cladding process

In the one-step laser cladding process the precursor material is fed dynamically into the melt pool generated by the laser source. The simultaneous movement of the laser source and of the feeding system (or, alternatively, the movement of the base material) leads to the formation of the coating. Large areas or complex 3D-structures can be treated by the overlap of several beads to create a layer and by the application of consecutive layers on top of each other respectively.

Precursor material is usually in form of powder, but wire feeding, strip feeding or hybrid process are also possible.

### One-step laser cladding process with powder feeding

Laser cladding with powder feeding is the most diffused one-step method due to the wide range of materials and alloys available in form of powder and to the good coupling efficiency between powder itself and laser beam [8]. In a typical blown powder laser cladding equipment (Figure 1.11), three main components are present: the laser system, the computer numerically controlled (CNC) robotic system and the powder delivery system [62].

The purpose of the laser system is to provide the necessary energy for the process through a laser beam. As seen in Chapter 1.2, the most common focusing systems produce circular, linear or rectangular beams. Circular beams have intensity which is function of the radial distance, while linear and rectangular beams have uniform intensity. Beam shape is controlled by the optics of the focusing mirror or lens, and beam area (or spot size) can be changed by varying the working distance between the focusing device and the surface of the component. Usually laser beam is perpendicular to the substrate surface. Different configurations are possible, but this influences the energetic efficiency of the process since the laser absorption of most materials is a function of the incident angle between laser beam and melt pool surface [62,63].

12
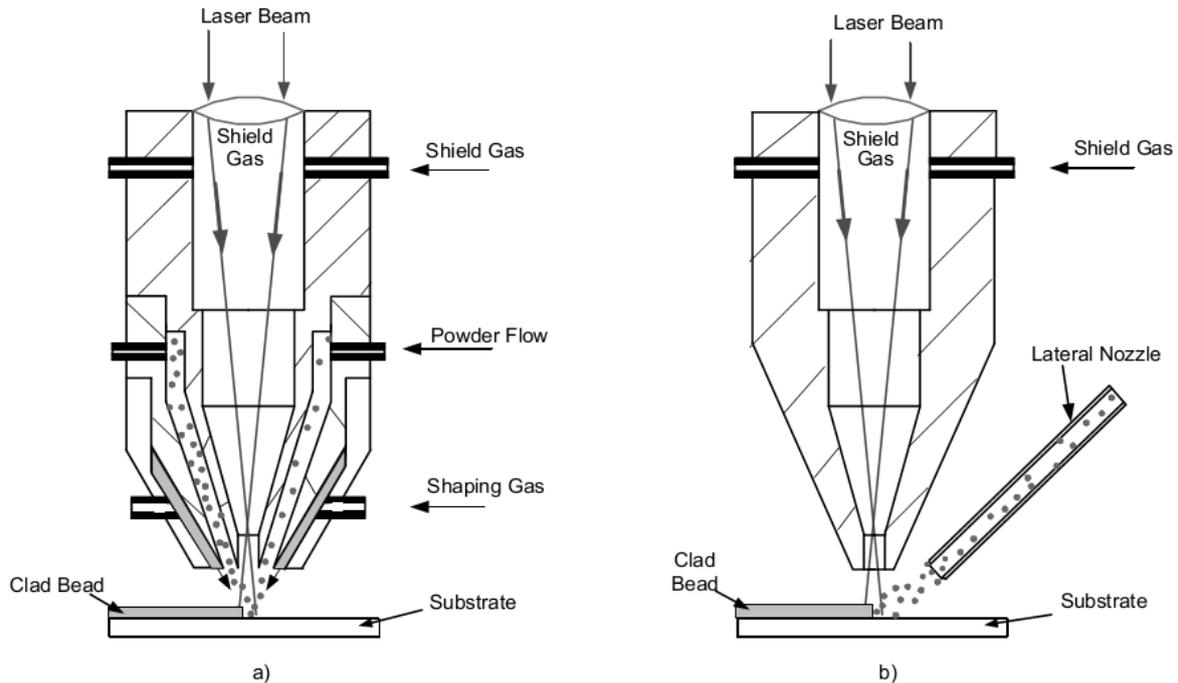
*Figure 1.11. Typical blown powder laser cladding equipment with (a) coaxial nozzle and (b) lateral nozzle [11].*

The CNC robotic system ensures the relative movement of the component and of the laser beam. Two possible configuration exist: either the specimen is fixed and the laser head, together with the feeding system, move thanks to a CNC-robot arm coupling; alternatively, the specimen is clumped to a CNC-table which moves relative to the laser-powder delivery system [62].

The powder feeding system must be capable of delivering the proper amount of powder to the interaction zone produced by the laser. The powder may be delivered by gravity or by a gas pressurized system. The latter is preferred since it allows cladding in any orientation and prevents oxidation: in fact, together with the carrier gas, a shielding gas such as helium or argon is delivered to the cladding zone to protect the molten pool from the atmosphere.

The process starts with the laser beam, which irradiates a thin layer of substrate to form a melt pool. Subsequently, powder is injected into the cladding zone, is captured by the melt pool and melts. After this, the laser-powder delivery system continues its path: the melt pool begins the solidification process along the steepest thermal gradient and clad starts to form.

The condition that determines whether the delivered powder sticks to the cladding zone to form the clad or not is defined by the type of impact. The possible types of impact are listed below, and are influenced by the laser energy absorption by the substrate and the powder particles:

- *solid powder – solid surface*: both the powder and the substrate do not absorb enough laser energy to melt and remain in a solid-state. The powder particle is deflected and get lost.
- *solid powder – liquid surface*: the powder particle, which doesn't absorb enough energy to melt, is captured by the molten pool formed.
- *liquid powder – solid surface*: the powder particle melts during injection and sticks to the solid surface of the substrate leading to powder catchment.
- *liquid powder – liquid surface*: both the substrate and the powder particle melt leading to catchment.

The catchment efficiency depends mostly on the formation of the melt pool, which allows the catchment of the powder particles injected [11,64-66]. In particular, material efficiency is strongly dependent on the melt pool dimension relative to the dimension of the impact area of the powder stream [8,67,68]. In general, material efficiency of the one-step laser cladding process with powder feeding is low, especially when compared to that of the two-step process, and remains the main disadvantage of this technique. Values reported in literature usually range between 40 and 80%. Some works report the possibility to increase material efficiency and productivity by using finer grade powder (< 53 μm)[10,69], with the additional benefit of the lower surface roughness of the final coating. Nevertheless, the use of fine powders increases the risk of vaporization and aerosol emission in the working room[70,71]; moreover the injection of these powder, that remains a critical aspect of this technology, may be compromised due to powder agglomeration and problems in powder flow in powder feeders and cladding nozzles.

The element that strongly characterizes the blown powder technique, as it can be seen in Figure 1.11, is the powder feeding system. Powder feeding can be performed in two ways: off-axially, also known as lateral feeding, and coaxially.

The off-axis nozzle provides a better powder catchment efficiency than the coaxial nozzle. Since the geometry and the alignment of the nozzle influences the material efficiency, as stated by Marsden [72], powder efficiency can be further increased by using a rather high injection angle between horizontal and nozzle (Figure1.12).
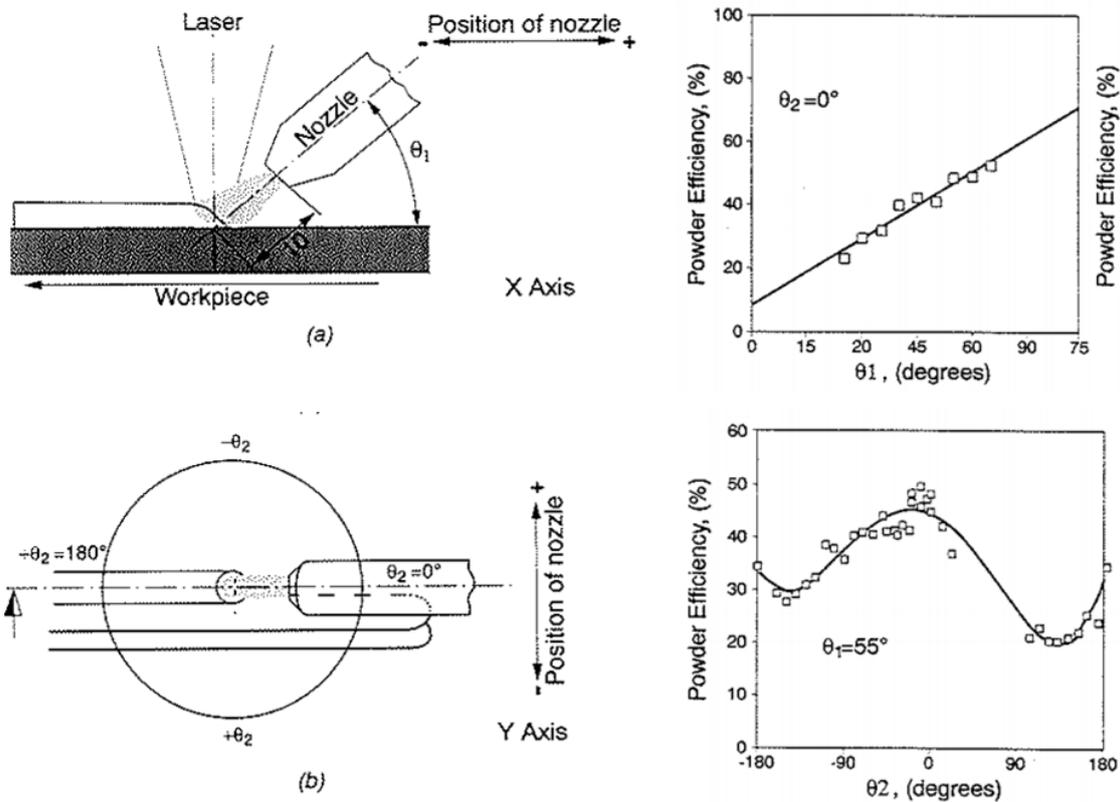


*Figure 1.12. Schematic of blown powder laser cladding showing (a) the longitudinal section with the inclination $\theta_1$ and its influence on the powder efficiency and (b) a plan view of the clad surface with the orientation $\theta_2$ and its influence on the powder efficiency [67].*

The possibility to change the position of the lateral nozzle allows to direct the powder flow to the desired part of the melt pool. Therefore, the interaction time between powder particles and laser beam

can be controlled in order to ensure the proper heating of the powder or, in case of externally added hard reinforcements, to avoid their dissolution. The main drawbacks of the off-axis feeding system is the low reproducibility of the process, since small variation in the nozzle location leads to substantial variation in clad geometry, dilution and powder efficiency, and the dependence of the process on the cladding direction.

In coaxial feeding process, powders are injected by a cone-shaped powder nozzle which surrounds the laser beam (Figure 1.11). This configuration allows the system to be independent on the cladding direction. In addition, powder-beam interaction time is rather long (longer than in off-axis cladding), leading to a more efficient preheating of the powder particles during their travel. Energetic efficiency of the process, as a consequence, is expected to be higher in the coaxial process due to the longer interaction times and multiple reflections occurring in the powder cloud [8].

***One-step laser cladding process with wire/strip feeding***

In this technology, a wire or a strip is dynamically fed into the cladding system to form the coating. There are two possible methods the wire can be melted: in the first method, the laser beam heats the wire extremity which melts and form a metal liquid droplet; the droplet falls on the component surface to form the cladding bead (Figure 1.13,a). This set-up, however, works rather erratically and generates coatings with irregular surface aspect. In the second method the wire is directly fed into the melt pool generated on the component surface by the laser beam, and melting of the wire occurs inside the melt pool by conduction (Figure 1.13,b) [73]. In this case, wire alignment becomes fundamental [74].
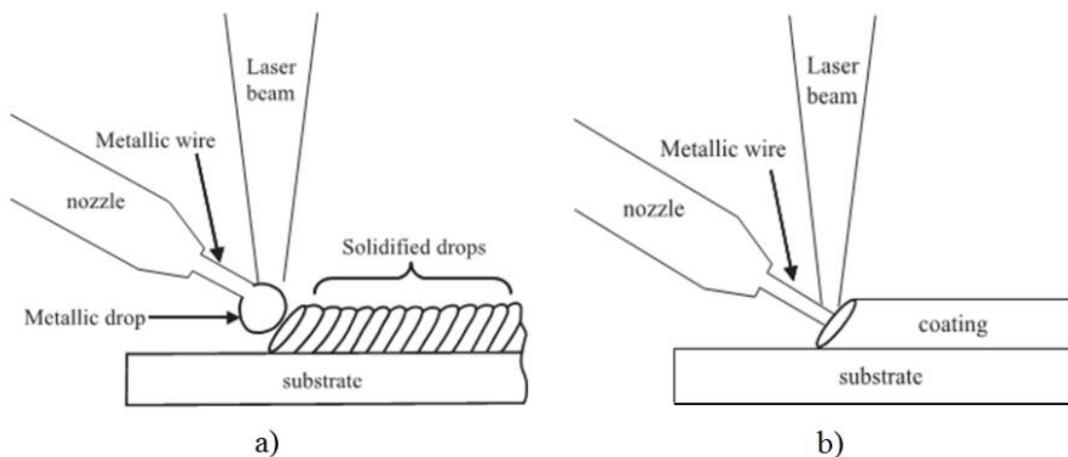


*Figure 1.13. Schematic of laser cladding with wire/strip feeding in (a) drop by drop configuration and (b) classical configuration [73].*

Wire feeding technology has always played a secondary role in one-step laser cladding technology due to a series of problems: the limited range of materials available in form of wire, the high sensitivity of the process to wire alignment and the poor coupling efficiency between the laser light and the cylindrical surface of the wire. On the opposite, the main advantages of this technique are the minimal waste of material, since usually the totality of the wire is deposited, the absence of residual powder emission that can harm human health and affect machinery and the fact that common materials are cheaper in wire form than in powder form.

As discussed, feeding direction, feeding angles and tip position of the wire play a key role in this process and are thus subject of many scientific articles. Wire can be fed from a leading direction (Figure 1.14,a), from a trailing direction (Figure 1.14,b) or from the side (Figure 1.14,c) [75].
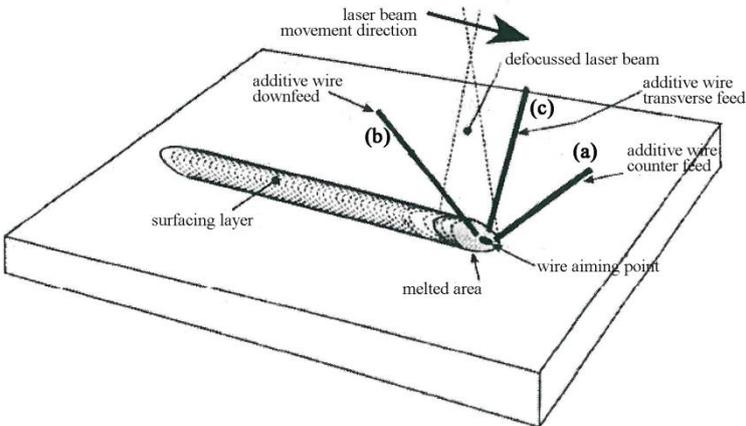


*Figure 1.14. Additive wire feeding directions: (A) trailing, (B) side and (C) leading [74].*

Feeding angle between wire and horizontal plane and wire tip position with respect to the melt pool can also be varied as shown in Figure 1.15.
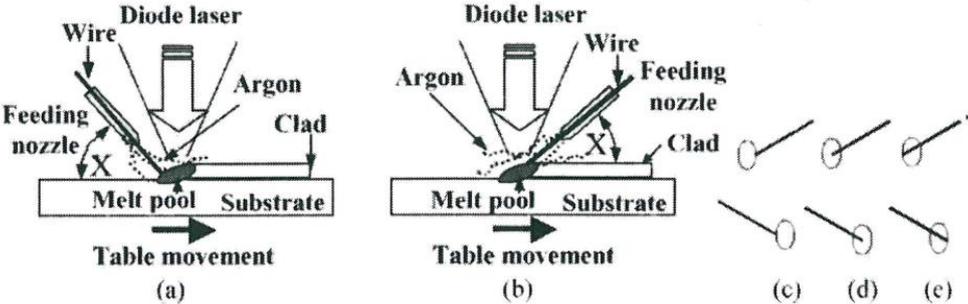


*Figure 1.15. Possibilities of wire feed angles and positions: (a) leading wire, (b) trailing wire, (c) wire tip not crossing the melt pool (d) wire tip in central position (e) wire tip crossing the melt pool [74].*

Most of the authors suggest the use of the wire feeding from a leading direction, with a rather small feeding angle and the wire tip placed at the leading edge [73,76-78].

Regarding strip feeding, the only difference between this technology and wire feeding is the better coupling efficiency of the flat surface of the strip with the laser beam when compared to the cylindrical surface of the wire. This can lead to higher energetic efficiencies and deposition rates of the process [79].

*Hybrid laser cladding process*

In the hybrid laser cladding technology, an additional heat source is utilized together with the typical cladding set-up to supply extra energy to the process. This surplus of energy, that can be supplied to the additive material and/or to the base material, is used to increase productivity (kg/h) and deposition rate (m²/h), to decrease the laser energy required or to produce better coatings.

The most efficient way to provide extra energy to the additive material is to use the laser cladding with wire/strip feeding equipment, heating up the wire/strip with induction or resistive heaters before

feeding it into the melt pool. Different works report the advantages of this hybrid process: heated wires allow to obtain the same process productivity using a lower laser heat input (i.e. lower laser power and/or higher scanning speed) [80], and to achieve higher deposition rates [81,82].

Base material heating is generally used when cladding with brittle hardfacing alloys with the purpose to decrease the steep thermal gradients created during the process thus forming crack-free coatings. An efficient and utilized method to perform base material heating is by means of induction. Examples of the production of crack-free metal matrix composites (MMCs) clad layers [83] with simultaneous increase in deposition rates [83,84] by using induction heater on base material are presented in literature.

Other possible hybrid processes include the use of combined surface technologies such as laser assisted thermal spraying, thanks to which dense multi-material structure (for instance thermal barrier coating) [85,86] or thin coatings with good features and low heat input can be created [87], or laser + PTA [84].

## 1.4 Process parameters in laser cladding

Quality and properties of laser cladding coatings can be determined by a large variety of factors such as clad geometry, microstructure, dilution, presence of defects, residual stresses, distortion, surface roughness, metallurgical changes in substrate and process efficiency. These factors, more or less important, are influenced by laser cladding process parameters and, consequently, by physical phenomena occurring in the cladding process. The chart in Figure 1.16 summarizes parameters and phenomena involved in the process, grouping them as inputs, process and outputs.

Process parameters can be classified in beam, feeding, materials and operating parameters. Beam and feeding parameters are generally fixed and are dictated by the choice of equipment, laser and optics. Materials parameters are related to the choice of additive material and substrate, and include the powder particles properties (particle size and morphology, chemical composition, thermophysical and optical properties) and the substrate properties (geometry and mass, chemical composition, surface condition, thermophysical and optical properties). Operating parameters can be changed by the laser cladding operator and their variation affects the process results. Among these, laser power ($P$), scanning speed ($V$) and feeding rate ($F$) are considered the principal parameters since they have the largest effect on the characteristics of the coating. Following, interactions present in literature of these three principal parameters with clads basic features are reported.

Height of the clad increases on increasing the feeding rate [88-90]. In laser cladding with powder feeding, the correlations between height and feeding rate ($F$) and between height and powder feed rate per unit length ($F/V$) are generally linear [41,91-94]. As well as height, the cross-sectional area of the clad ($A$) increases on increasing $F$ and $F/V$ [95,96]. Beyond a threshold value of feeding rate, the increment of A may accelerate due to multiple scattering of laser beam in dense powder cloud [96].

Laser power has a limited effect on clad height. Anyway, in literature it is reported that an increase in the laser power while other parameters are kept constant leads to an increase in bead height [51,97].

Clad width is principally dictated by the spot of the laser beam. However, a width wider than the spot size can be obtained with very low processing speeds and high laser powers [98]. In general, clad width increases on decreasing the scan speed and on increasing the laser power [77,89,98,99]. In coaxial laser cladding, these correlations are linear [91,98].

**INPUTS**

**PROCESS**

**Beam properties**
- wavelength
- polarization
- intensity
- spot dimension

**Materials properties**
*substrate properties*
- geometry
- mass
- chemical composition
- surface condition
- optical, metallurgical and thermophysical properties

*powder properties*
- particle size
- morphology
- composition
- thermophysical and optical properties

**Feeding parameters**
- feeding equipment
- direction and angle
- shielding gas
- aiming

**Operating parameters**
- laser power
- scan speed
- feed rate
- overlapping
- preheating
- cladding strategy

**Physical phenomena**
- absorption
- conduction
- convection
- diffusion
- melt pool dynamics
- oxidation
- solidification
- gas - melt pool - powder - laser beam interactions

**OUTPUTS**

**Results**
- geometry
- aspect ratio
- microstructure
- dilution
- segregation
- cracking
- porosity
- residual stresses
- surface roughness
- distortion
- metallurgical changes in substrate
- material efficiency
- energy efficiency
- productivity

*Figure 1.16. Inputs, outputs and process parameters of laser cladding by powder injection.*

Aspect ratio, which is defined as the ratio between width and height of the clad ($W/H$), is affected consequently: as clad height, aspect ratio strongly depends on feeding rate and scan speed [100,101]. Substrate melting is principally controlled by the energy available per unit mass of powder $P/F$: dilution increases on increasing the laser power [97,98,102] and decreases on increasing the feed rate [88,93,94,100]. An increase in the scan speed, especially in thin beads, tends to increase dilution [100,103-105], while for clad with higher bead heights this influence becomes less significative [8].

The comprehension of the correlations between processing parameters and clad characteristics is fundamental for the production of defect-free coatings with desired geometry, fusion bond and low dilution. Basically, once the additive and substrate materials are selected, a good laser cladding process can be guaranteed by the adequate proportion between material fed and laser energy supplied. This concept can be seen in the work of Steen et al. [106], who showed the feasibility window of a laser cladding process with a Stellite 12 powder using a 2 kW continuous-wave $CO_2$ laser in a diagram where the laser power per spot diameter (W/mm) is reported as a function of the powder feed rate (g/s). The feasibility region is always restricted by power limits, dilution and aspect ratio (or, alternatively, contact angle), and these limits can be defined by the combination of the processing parameters. For instance, Steen correlated the beginning of the non-wetting region with the combined parameter $P/VD$, where $D$ is the spot diameter. This parameter sets the energetic limits to avoid discontinuous clad tracks. Substrate melting, which is caused by an excess on energy above that

needed to melt the powder, can be correlated with *P/FD*: this parameter can give the maximum value before dilution sets in. Finally, the combined parameter *PVD/F²* is correlated with the aspect ratio: since aspect ratio must be higher than 5 to avoid inter-run porosity (or, alternatively, contact angle must be higher than 100°), the value of this parameter for which aspect ratio is 5 sets another limit on the operating region.

As shown by the work of Steen, combined parameters are always used due to mutual interactions between processing parameters and due to the complexity of the laser cladding process. One of the most appropriate way to reveal operating window and investigate correlations is thus to create a process map. An example of such map is given by the work of de Oliveira et.al. (Figure 1.17) [91].
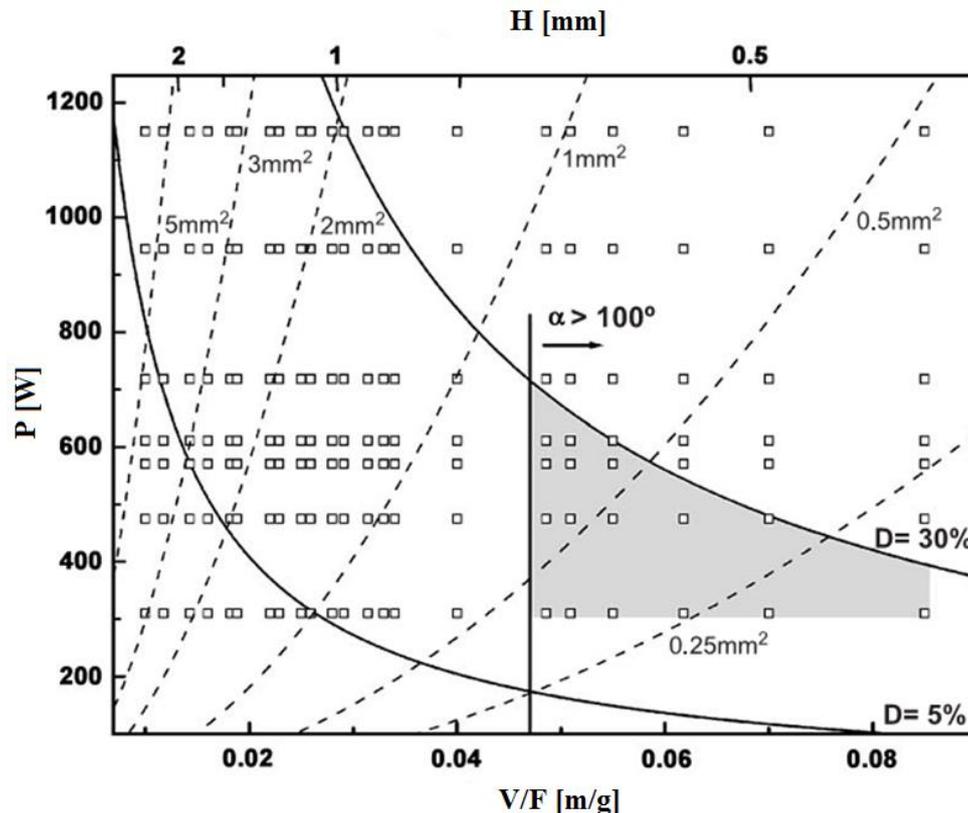


*Figure 1.17. Processing window for coaxial laser cladding where laser power (P) is reported as a function of the ratio between scan speed (V) and feeding rate (F). Vertical solid line determines the clad angle condition required for continuous coating; two solid hyperbolas terminate an area of allowed dilution and the grey area shows the optimal clad layer window [91].*

In this graph, the laser power is reported on the y-axis while the ratio between scan speed and feeding rate is reported on the x-axis. Operating window, which is represented by the light grey portion of the map, is limited by dilution (solid curves), laser power limits and contact angle (vertical solid line). Clad height (x-axis) and clad cross-sectional area (dashed curves) are also represented. All these correlation between clad properties and processing parameters can be found by regression analysis. By the way, creation of processing map requires large amount of cladding experiments and principal processing parameters must be varied up to their limits.

## 1.5 Clad characteristics

As stated above, properties of laser cladding coatings can be determined by a large variety of factors. In this section, the main characteristics of a clad are reported and discussed.

### 1.5.1 Clad geometry

The typical cross-section of a single clad bead is reported in Figure 1.18, where the most common parameters associated with clad geometry are shown. These are:

- *clad height (H)*: thickness of the clad bead above the original surface of the clad substrate;
- *clad width (W)*: width of the single clad bead;
- *clad depth (B)*: thickness of the substrate melted during cladding and added to the clad;
- *clad cross-sectional area (A)*: area of the clad cross-section;
- *HAZ depth ($B_{HAZ}$)*: depth of the heat effected zone in the substrate;
- *HAZ area ($A_{HAZ}$)*: area of the heat effected zone in the substrate;
- *contact angle ($\alpha_{wet}$)*: also known as wetting angle, is the angle between the substrate surface and the tangent to the clad surface.
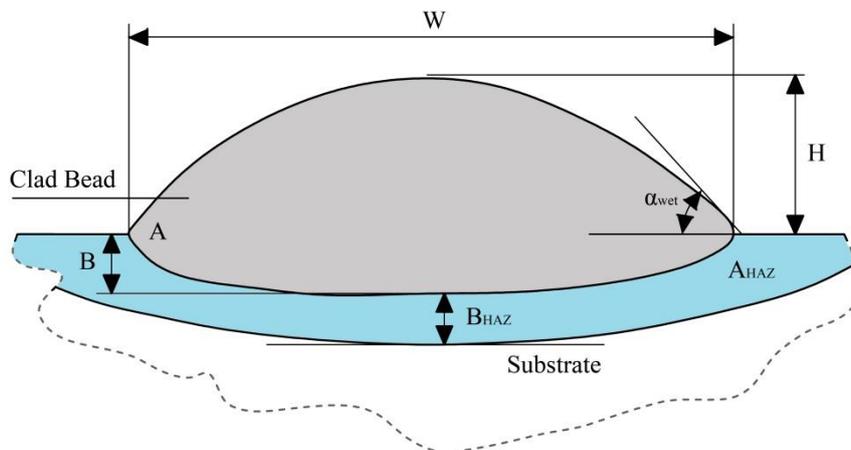


*Figure 1.18. Typical clad cross-section with most common geometrical characteristics.*

### 1.5.2 Dilution

Dilution is considered an important factor in order to control the contamination of the clad by the substrate material. In fact, even though a minimum level of mixing is necessary to guarantee a good bonding with the substrate, an excessive dilution might influence the properties of the coating negatively. Dilution may be measured in different ways. In the most common method, dilution is

given by the ratio $A_D/(A_N+A_D)$ between the cross-sectional area of the molten substrate material ($A_D$) and the total cross sectional area of the clad ($A_N+A_D$) (Figure 1.19) [103,107-109].
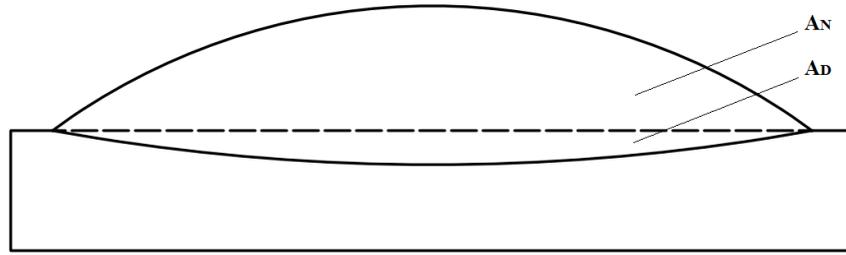


*Figure 1.19. Schematic drawing of the clad cross-sectional area showing the part of the cross-sectional area emerging from the original surface of the plate ($A_N$) and the melted cross-sectional area of the substrate ($A_D$).*

Toyserkani et al. and Zhao et al. [11,110] used the ratio $V_D/V$ between the volume of molten substrate ($V_D$) and the total volume of the deposited layer ($V$). Toyserkani et al. and Huang et al. [11,108] also correlated dilution with the ratio $B/(H + B)$ between the molten substrate depth ($B$) and the sum of the molten substrate depth and the height of the clad bead ($B + H$) (Figure 1.18). All these methods are based on the dimensional and geometrical features of the clads. As an alternative, Salehi [111] used the iron content to determine dilution ($D$) through the equation $D = (L_{Fe} - P_{Fe})/(S_{Fe} - P_{Fe})$, where $P_{Fe}$, $L_{Fe}$ and $S_{Fe}$ are the iron concentration in the supplied powder, in the clad and in the substrate respectively.

## 1.5.3  Microstructure

Functional properties and quality of coatings produced with laser cladding technology are strongly dependent on final microstructure.

The first prerequisite for a successful laser cladding process is to homogenize the melt pool, and homogenization of laser melt pool is guaranteed by convection. In fact, the large thermal gradients within the melt pool generate intense convection by Marangoni effect [112,113]. The parameter that characterize the influence of convection on liquid homogenization is the surface tension number $S$, defined by equation

$$S = \frac{\left(\frac{d\gamma}{dT}\right) \cdot Q \cdot D}{\mu \cdot V \cdot k} \qquad (1.1)$$

where $d\gamma/dT$ is the temperature coefficient of the surface tension, $Q$ is the net energy flow per area from laser beam, $D$ is he laser beam diameter, $\mu$ is the melt pool viscosity, $V$ is the scanning speed and $k$ is the thermal conductivity of the clad material. For low values of $S$ convection can be neglected: mass transport in the melt pool is predominantly diffusive, resulting to a non-homogeneous compositional distribution due to the short lifetime of the melt pool. For high values of $S$ convection has a key-role in heat and mass transfer and a homogeneous distribution of the chemical composition can be obtained. Generally, the speed of convection for metals is several order of magnitude higher than the scanning speed, resulting to an extremely rapid homogenization [9,11].

Together with melt pool homogenization, the control of the solidification process is fundamental to obtain the desired microstructure. In laser cladding process cooling rates are very high, usually in the range of $5 \cdot 10^3 – 10^6$ K/s, and solid state diffusive transformations are usually suppressed [8]. For this reason, in addition to the chemical composition and thermophysical properties of the coating alloy, final microstructure is mostly determined by the solidification process. In laser cladding solidification is frequently rapid since growth rates of the solid-liquid interface are often higher than 10 mm/s, and the typical microstructures detected in laser coatings are planar, cellular and dendritic [8,9]. For a given alloy, the solidification microstructure depends on the local solidification conditions, which are determined by the cooling rate ($R$) and the thermal gradient at the solid-liquid interface ($G$). Specifically, growth morphology of rapidly solidified layers is controlled by the parameter $G/R$. If $G/R$ is higher than a critical value ($G/R$)* a planar solidification front takes place, while if $G/R$ gets lower than this critical value the planar solid-liquid interface is destabilized and cellular or dendritic solidification occurs [60]. These solidification conditions ($G$ and $R$) are function of the size and the geometry of the melt pool, which is in turn influenced by the laser cladding processing conditions such as laser power, scan speed, feeding rate, beam diameter or temperature of the substrate [114]. In particular, as it can be seen in Figure 1.20, they can be expressed as function of the depth of the formed bead.
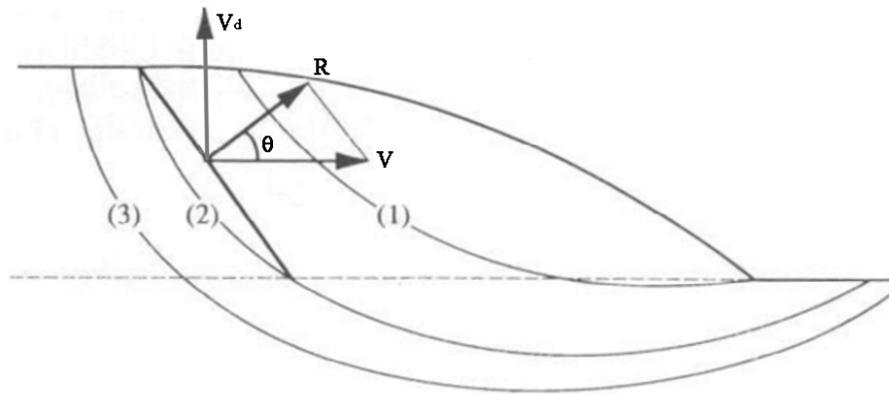


*Figure 1.20. Transverse cross-section parallel to cladding direction cut through the centreline of the clad bead showing the solidification rate (R), the scan speed (V), the angle (θ) between them and the growth rate of dendrites ($V_d$) [8].*

The correlation between the solidification rate ($R$) and the scan speed ($V$) is

$$R = V \cdot \cos \theta \qquad (1.2)$$

where $\theta$ is the angle between the scan speed vector and the normal to the solid-liquid interface. Since the angle $\theta$ is 90° at the bottom of the melt pool (i.e. $\cos\theta = 0$) while it tends to 0° at the top of the melt pool (i.e. $\cos\theta \rightarrow 1$), the solidification rate is equal to 0 at the substrate-coating interface and it increases to a constant value during most of the solidification time as the surface is approached [8,115-117]. This constant value is by the way lower than the scan speed and, as said before, is influenced by the shape of the melt pool. In contrast to $R$, the thermal gradient $G$ is at maximum at the bottom of the melt pool and it decreases progressively towards the surface [114]. According to this, the behaviour of $G/R$ along the depth of the clad bead can be schematically represented by the illustration in Figure 1.21, where the effect of $G/R$ on the microstructure of a bead cross-section is shown.
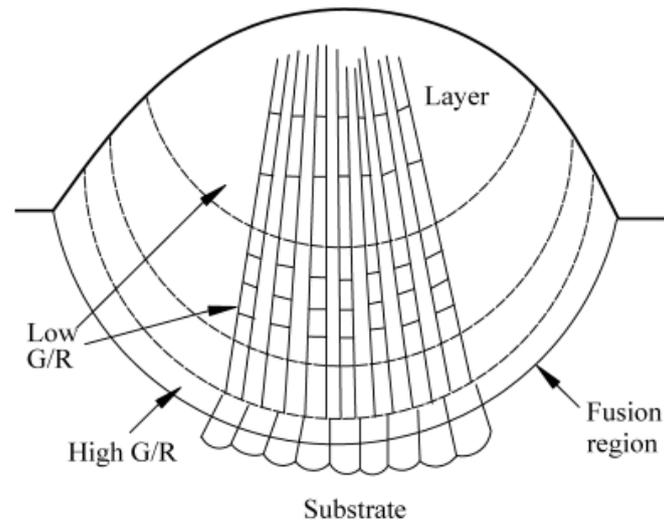
*Figure 1.21. Schematic illustration of the formation of the cladding layer and crystallographic analysis [118].*

Epitaxial solidification begin on the substrate without the need for nucleation and proceed unidirectionally towards the top. At the beginning of the solidification, at the bottom of the melt pool, a plane front solidification zone appears since the liquid metal maintains contact with the solid substrate (solidification rate is 0 and $G/R$ presents and infinite value). With the propelling of the solid-liquid interface and the accumulation of heat, $R$ increases rapidly and $G$ decreases leading to a lower value of $G/R$: the planar front evolves to a cellular, and eventually to a dendritic, interface as $G/R$ decreases. Because of the rapid variation of $G/R$, this interface is very narrow. Progressively the value of $G/R$ decreases until it reaches a value that remains constant during most of the solidification process: in this region, which follows the cellular interface zone, dendritic solidification appears. Cellular and dendritic solidifications are usually columnar in shape and tend to grow perpendicular to the coating-substrate interface (or perpendicular to temperature isotherms) since heat is mostly dissipated through the substrate and, along this direction, the steepest thermal gradient is developed. Close to the surface of the clad layer, finally, the heat is mostly dissipated through the surrounding atmosphere and $G$ is not predominant anymore: for this reason, in this region dendrites become very fine and disorientated [118].

## 1.5.4   Coating defects

The main defects that can be present in coatings produced with laser cladding are cracks and pores/voids.

Cracks in laser coatings can be divided into brittle and hot cracks. Hot cracks of laser cladding layers are similar to welding hot cracks. Also known as solidification cracks, these defects are caused by the presence of phases or impurities with a low melting temperature. They usually appear in the fusion zone near the end of the solidification. Hot cracks are generally longitudinal to the clad bead and occur along grain boundaries due to preferential segregation of solute or impurity elements. During solidification, cellular dendrite tips rapidly grow with the consequent formation of low solidification temperature liquid film. On subsequent solidification and cooling, interdendritic shrinkage cavities

may form. Low dilution and high solidification rates limit the problem of the hot cracking because less solute redistribution occurs, leading to a more uniform composition of the solidification structure [119,120].

Brittle cracks are generated during cooling, when the hot coating tries to undergo shrinkage but it is constrained by the relatively cold and rigid substrate. If the ultimate tensile strength of the alloy is exceeded by the resulting tensile stress and all the possible deformability of the working piece is utilized, brittle cracks occur. These cracks are generally perpendicular to the clad/substrate interface. To avoid the formation of such cracks, substrate preheating is an efficient solution [8].

The presence of pores or voids in the clad layer may be caused by several reasons, and it can be classified according to its position in the clad layer. Porosity inside the clad can be the result of the formation of gas bubbles entrapped into the solidifying melt pool. Internal porosity can also be present if solidification proceeds in different directions: in this case, some region of the melt can be enclosed. Upon solidification, when contraction of these enclosed region occurs, tensile stresses in the layer are generated and holes may be found. Porosity at the clad-substrate interface can be caused by minor flaws on the substrate surface (such us grease, oxides, defects and so on) that may influence the surface tension and consequently the bond between the coating material and the substrate. Finally, inter-run porosity may occur between adjacent beads in multiple-beads laser cladding. These kind of pores are usually caused by an incorrect design of the laser cladding process (too low aspect ratio) [12].

Excessive dilution and compositional non-homogeneities can also be considered as defects in laser cladding.

## 1.5.5 Residual stresses

In laser cladding, the laser beam is a very localized heat source having high intensity and short interaction times. For this reason, large thermal gradients spring between the hot molten clad layer and the relatively cold solid substrate or, in case of multiple-beads laser cladding, the adjacent bead. During the initial rapid cooling the clad material tends to shrink, but the contraction is restricted by the substrate and the adjacent bead: this leads to the formation of tensile stresses [67]. These tensile stresses are directly related to the thermal expansion coefficient of the clad material ($\alpha_C$), its Young's modulus ($E_C$) and the temperature difference between the melting temperature of the clad material and the temperature of the substrate during the process ($\Delta T$) according to the equation

$$\sigma_{th} = E_C \cdot \alpha_C \cdot \Delta T \qquad (1.3)$$

These stresses can be anyway partially relaxed by plastic deformation and creep. In the second stage of cooling, from the processing temperature down to the ambient temperature, the formation of residual stresses takes place. In this case, the magnitude and the sign of the stresses depend on the difference in temperature between melt pool and substrate during processing, the difference in the thermal expansion coefficients between coating and base material, their mechanical properties (Young's modulus and yield strength), the cooling rate, the substrate geometry and eventual solid-state phase transformation involving volume changes [67]. If no deformation of the base material and no

volume changes due to phase transformation are assumed, resultant stresses can be estimated through equation

$$\sigma = \frac{(\alpha_C - \alpha_S) \cdot (\Delta T_I) \cdot E_C}{1 - \nu_C} \qquad (1.4)$$

where $\sigma$ is the resulting residual stress, $\alpha_C$ and $\alpha_S$ are the thermal expansion coefficients of the clad and of the substrate material respectively, $\Delta T_I$ is the temperature difference between melt pool and substrate, $E_C$ is the Young's modulus of the coating material and $\nu_C$ is the Poisson's number of the coating material [121].

The difference between the thermal expansion coefficient of coating and substrate play a fundamental role in the generation of residual stresses. If $\alpha_C$ is higher than $\alpha_S$, the larger is the difference between the coefficients, the higher are the tensile stresses in the coating layer; if $\alpha_C$ is lower than $\alpha_S$, the larger is the difference between the coefficients, the lower are the tensile stresses [8].

The effect of the temperature is clear: the lower is the difference between the melt pool and the substrate, the lower are the resultant stresses. Substrate preheating, which lowers the temperature difference, has always a positive effect on decreasing the tensile stresses in the coating in any condition. Moreover, substrate preheating favours the relaxation of the evolving stresses because decreases cooling rates, which allows more time for plastic deformation and creep to occur [8].

Inhibit the formation of tensile stresses in the coating layer is always positive: tensile stresses have detrimental effect on fatigue, tensile, wear and corrosion behaviour of the coating and may jeopardize the integrity of the coating [8].

## 1.6  Energetic efficiency and productivity of laser cladding process

In laser cladding, the energy necessary for the process is supplied by the laser light. The interaction between the laser electromagnetic radiation and both the powder particles and the melt pool, which involves the absorption/reflection phenomena of laser light, are decisive to determine energetic and melting efficiencies: these affect not only the quality of the final coating, but also process productivity and thus costs. Therefore, the comprehension of the energy partitioning in the laser cladding process is of great interest [8]. In Figure 1.22, a schematic illustration of the energetic redistribution for a blown powder cladding process during its steady-state is reported.

Before reaching the workpiece, the laser beam passes through the powder particles jet and the laser light interacts with the powders: part of the energy that hits the powder is reflected off the particles surface ($E_{P,refl}$), while the rest of it is absorbed by them. As a consequence the laser beam results to be attenuated by the powder jet, and the effective laser power available at the melt pool surface is lower. When the "attenuated" laser light hits the melt pool, a fraction is reflected off the melt pool surface while the remaining part is absorbed by the cladding system. The energy absorbed by the workpiece is divided as follow: part of it is used to heat up, melt and superheat the powder and the substrate (i.e. the energy to produce the coating $E_C$, which is equal to the sum of $E_P$ and $E_S$), another part is lost by conduction from the melt pool into the substrate (i.e. energy to form the heat affected zone $E_{HAZ}$ and to heat up the base material $E_{bulk}$) and the remaining small part is lost by radiation and convection from the melt pool to the surroundings ($E_{rad}$ and $E_{conv}$) [68,122-124].
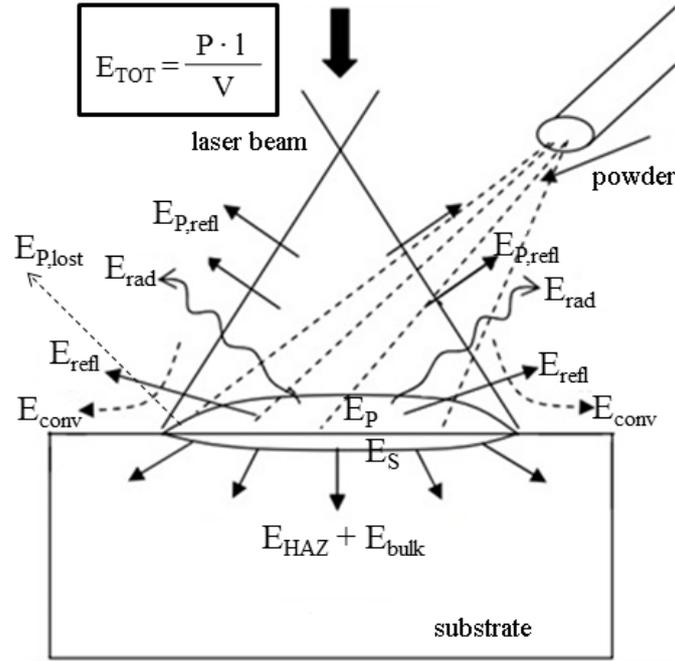
*Figure 1.22. Schematic illustration of the energetic redistribution for a blown powder cladding process during its steady-state [122].*

Reflection and absorption of laser irradiation by the melt pool surface play a key-role in the energy balance. Laser absorption by metallic surfaces strongly depends on the laser light (polarization and wavelength), the optical properties of the coating material and the angle of incidence (i.e. the angle between the laser beam and the normal to the melt pool surface, which is assumed to be flat). Absorptivity, defined as the ratio between the absorbed part of the incoming radiation and the total incoming radiation, is correlated to these factors through Fresnel's equations

$$A_p = \frac{4 \cdot n \cdot \cos\theta_{in}}{(n \cdot \cos\theta_{in}+1)^2+(k \cdot \cos\theta_{in})^2} \qquad (1.5)$$

$$A_s = \frac{4 \cdot n \cdot \cos\theta_{in}}{(n+\cos\theta_{in})^2+k^2} \qquad (1.6)$$

where $\theta_{in}$ is the angle of incidence, $n$ is the refraction index and $k$ is the extinction coefficient. The refraction index and the extinction coefficient are optical constants of the coating material and are influenced by temperature and laser wavelength [50,55,125]. In specific, they depend on plasma, laser and collision frequency [126]. In equations (1.5) and (1.6) the suffixes $p$ and $s$ denote the polarization condition of the laser beam: p-polarized light is a linearly polarized radiation having the electric field vector parallel to the plane of incidence, while s-polarized light is a linearly polarized radiation having the electric field vector perpendicular to the plane of incidence. In the case of circular polarization or with randomly polarized beams, the average absorptivity can be estimated as the average values of the p- and s-absorptivity

$$A_{av} = \frac{1}{2} \cdot \left(A_p + A_s\right) \qquad (1.7)$$

Fresnel's equations are valid for opaque medium when $(n^2+k^2)>>1$, as it is for metals at wavelength higher than 500 nm [125]. Since in these conditions transmissivity is equal to 0 [50], reflectivity can be calculated as well

$$R_p = 1 - A_p = \frac{(n \cdot \cos \theta_{in} - 1)^2 + (k \cdot \cos \theta_{in})^2}{(n \cdot \cos \theta_{in} + 1)^2 + (k \cdot \cos \theta_{in})^2} \qquad (1.8)$$

$$R_s = 1 - A_s = \frac{(n - \cos \theta_{in})^2 + k^2}{(n + \cos \theta_{in})^2 + k^2} \qquad (1.9)$$

$$R_{av} = 1 - A_{av} = \frac{1}{2} \cdot (R_p + R_s) \qquad (1.10)$$

In Figure 1.23 an example of the typical absorptivity curves obtained with Fresnel's equations are reported for iron at two different laser wavelengths ($\lambda$ = 1.06 μm for the Nd:YAG laser and $\lambda$ = 10.64 μm for the $CO_2$ laser) [127].
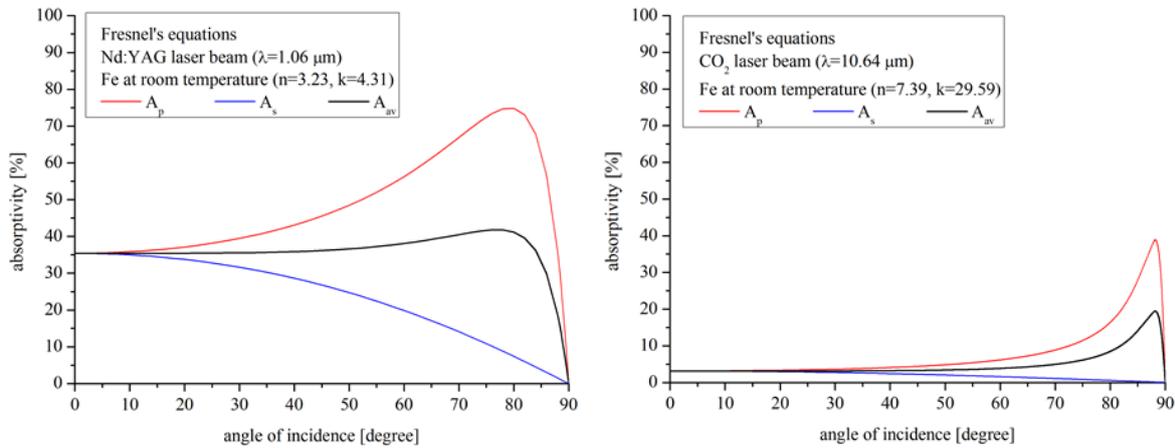


*Figure 1.23. Typical absorptivity curves obtained with Fresnel's equations for iron at two different laser wavelengths: λ=1.06 μm for the Nd:YAG laser (left) and λ=10.64 μm for the CO2 laser (right).*

From a practical point of view, in laser cladding the angle of incidence can be modified by varying the processing parameters: for instance, when powder feed increases the thickness of the coating increases consequently, leading to a more inclined melt pool (i.e. higher angle of incidence). As a consequence, when a linearly p-polarized laser beam is used, absorption increases because the incident angle approaches the well-known Brewster angle [88,99,124]. The angle of incidence can also be modified by simply varying the inclination of the laser beam with the same effect on absorption. Examples of this are reported in literature, were laser remelting tests at different angles of incidence were conducted [128,129]. With randomly polarized laser beams, anyway, such a positive Brewster effect cannot be realized and absorptivity cannot be modified significantly [8].

As said before, this behaviour strongly affects energetic efficiency and redistribution in laser cladding. According to a model developed by Pinkerton and Li [130] and confirmed by empirical results, energetic absorption tends to increase when lasers with shorter wavelength are used (HPDL rather than Nd:YAG or $CO_2$) (Figure 1.24).
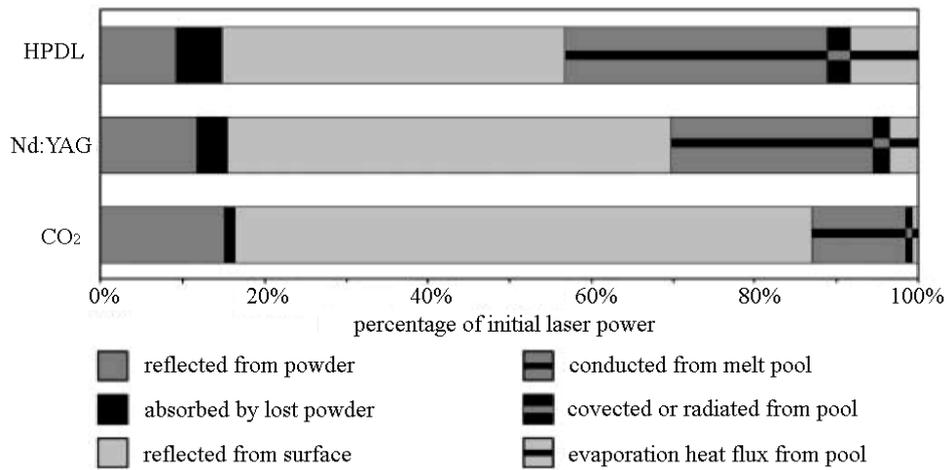
*Figure 1.24. Modelled distributions of the input laser power for HPDL, Nd:YAG and CO2 laser types [130].*

Energetic efficiency of the process, in this work estimated approximately around 15 – 50 % according to the laser source, is however lower than conventional welding processes such us PTA (50 – 70%), TIG (60 – 80%), MIG (70 – 80%), SAW and EBW (80 – 90%) [131].

Energetic efficiency have a direct effect on process productivity (i.e. deposition rate), since productivity is mainly related to the effective laser power available by the system. As shown by Figure 1.25, where deposition rates of laser cladding trials with different alloys (Fe-, Ni- and Co-based) on Fe-based substrates are reported as a function of laser power, on increasing the laser power productivity tends to increase. Moreover, short-wavelength lasers and hybrid processes favour higher deposition rates [8].
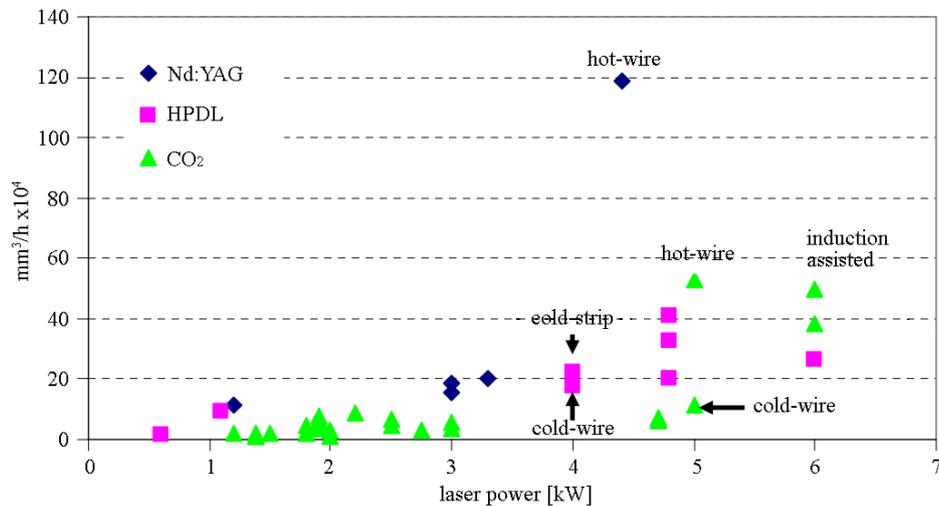


*Figure 1.25. Deposition rates expressed in $mm^3/h$ of different laser cladding processes as a function of the laser power for HPDL, Nd:YAG and $CO_2$ laser types [8].*

# Chapter 2
# Experimental procedures

## 2.1 Powders

The powders used for the present thesis work have been produced by Höganäs AB. Powders have been realized with the water-atomization process and have spherical morphology. The nominal chemical compositions of the powders utilized, provided by Höganäs AB, are summarized in Tables 2.1 - 2.3 together with their particle size.

*Table 2.1. Nominal chemical compositions of Ni-based powder used.*

| Ni-based powder | particle size [μm] | C [%] | Si [%] | Bo [%] | Fe [%] | Ni [%] | Cr [%] | Mo [%] | Nb [%] |
|---|---|---|---|---|---|---|---|---|---|
| NiBSi | 53 – 150 | ≤ 0.06 | 3.0 | 2.9 | 0.2 | bal. | - | - | - |
| Inconel 625 | 53 – 150 | ≤ 0.03 | 0.40 | - | 1.4 | bal. | 21.5 | 9.0 | 3.8 |

*Table 2.2. Nominal chemical compositions of Fe-based powder used.*

| Fe-based powder | particle size [μm] | C [%] | Si [%] | Fe [%] | Cr [%] | Ni [%] | Mo [%] | Mn [%] |
|---|---|---|---|---|---|---|---|---|
| 316L | 53 – 150 | ≤ 0.03 | 0.8 | bal. | 17.0 | 12.0 | 2.5 | 1.5 |

*Table 2.3. Nominal chemical compositions of Co-based powder used.*

| Co-based powder | particle size [μm] | C [%] | Si [%] | Fe [%] | Cr [%] | Ni [%] | Co [%] | Mo [%] | W [%] |
|---|---|---|---|---|---|---|---|---|---|
| Stellite 1 | 53 – 150 | 0.25 | 1.0 | 1.5 | 27.0 | 2.8 | bal. | 5.5 | - |
| Stellite 12 | 53 – 150 | 1.4 | 1.1 | 1.0 | 28.5 | 1.5 | bal. | - | 8.0 |
| Stellite 21 | 53 – 150 | 2.4 | 1.1 | - | 30.0 | - | bal. | - | 12.5 |

In order to study the dissolution behaviour of the tungsten carbides in a Co-based matrix, Stellite 12 and Stellite 21 powder were mechanically mixed with a mixture (65/35 vol.% respectively) of spherical and angular cast tungsten carbides having particle size ranging from 45 to 100 μm and a phase content of 61% $W_2C$ and 39% of WC. MMC powder combinations, ratios and hard particulate details are reported in Table 2.4.

*Table 2.4. Details of the MMC powder combinations used.*

| powder | wt. [%] | vol. [%] | carbide type [%] | shape [%] | phases | density [g/cm³] | carbide size [µm] |
|---|---|---|---|---|---|---|---|
| Stellite12/WC | 50/50 | ≈65/35 | fused/crushed | spherical and angular | $W_2C$ and WC (61/39 vol.%) | 16.6 | 45 – 100 |
| Stellite21/WC | 50/50 | ≈65/35 | fused/crushed | spherical and angular | $W_2C$ and WC (61/39 vol.%) | 16.6 | 45 – 100 |

## 2.2 Substrates

The substrates used for the present thesis work are grounded plates of mild steel and grey cast iron having dimensions of 100 x 35 x 10 mm. The nominal chemical compositions of the substrates utilized are summarized in Table 2.5.

*Table 2.5. Nominal chemical compositions of the substrates utilized.*

| substrate | C [%] | Si [%] | Cr [%] | Mn [%] | Ni [%] | P [%] | S [%] | Mo [%] | Fe [%] |
|---|---|---|---|---|---|---|---|---|---|
| grey cast iron | 2.9 – 3.6 | 1.8 – 2.9 | - | 0.4 – 0.7 | - | max 0.3 | max 0.1 | - | bal. |
| mild steel | 0.37 – 0.44 | max 0.4 | max 0.4 | 0.5 – 0.8 | max 0.4 | max 0.045 | max 0.045 | max 0.1 | bal. |

## 2.3 Laser cladding equipment

Laser cladding experiments have been carried out using a 4 kW Coherent Highlight 4000L direct high power diode laser (HPDL), mounted on an ABB IRB 2600 six-axis robot system. Laser operating wavelength was 808 nm. Laser beam, having a rectangular shape, was focused to a spot size of 12 x 1 mm²: 1 mm along the fast axis, i.e. scanning direction, and 12 mm along the slow axis. Intensity distribution had the classical "top-hat" profile along the slow axis.

Powder feeding have been achieved using a Thermach AT-1200 rotary powder feeder and a Coax11 coaxial type powder feeding nozzle (Fraunhofer IWS), tailored for rectangular or scanned line laser spots. Powder was fed into the melt pool, perpendicularly to the surface of the base material, from the opening of four channels on one side of the head only. The angle between the laser beam axis and the normal to the substrate surface ($\alpha_L$) was fixed at 28 degrees (Figure 2.1).

The carrier and the shielding gas used to obtain more focused powder stream and to prevent oxidation of powder particles and melt pool was argon. Carrier and shielding gas flow rates were 3.4 l/min.
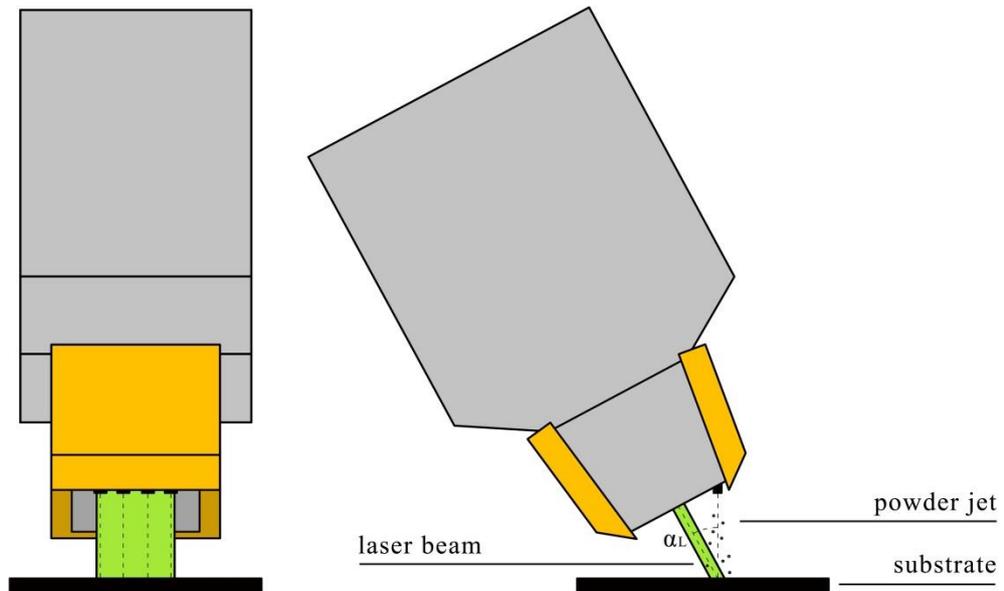
*Figure 2.1. Schematic of the laser cladding equipment used.*

## 2.4 Processing parameters

In the present work many batches have been produced by varying the three main processing parameters, i.e. the laser power $P$, the scan speed $S$ and the feeding rate $F$. Different combinations of powders and substrates have been utilized. In some cases, substrate preheating up to 400°C has been performed in a furnace or with oxy-fuel torch. Processing conditions ranges for the different batches produced are reported in Table 2.6.

*Table 2.6. Processing conditions for the different batches produced.*

| powder | substrate | preheating | P [kW] | F [g/s] | V [mm/s] |
|---|---|---|---|---|---|
| Stellite 1 | mild steel | - | 2.0 – 3.8 | 0.3 – 0.9 | 1 – 8 |
| NiBSi | mild steel | - | 2.0 – 3.8 | 0.3 – 0.9 | 1 – 8 |
| 316L | mild steel | - | 2.0 – 3.8 | 0.3 – 0.9 | 1 – 8 |
| In625 | mild steel | - | 2.0 – 3.8 | 0.3 – 0.9 | 1 – 8 |
| NiBSi | mild steel | 400°C, furnace | 2.0 – 3.8 | 0.3 – 0.9 | 1 – 8 |
| NiBSi | grey cast iron | 400°C, furnace | 2.0 – 3.8 | 0.3 – 0.9 | 1 – 8 |
| WC+Stellite 12 | mild steel | - | 2.0 – 4.0 | 0.5 | 5 |
| WC+Stellite 21 | mild steel | - | 2.0 – 4.0 | 0.5 | 5 |
| WC+Stellite 12 | mild steel | 400°C, oxy-fuel torch | 2.0 – 4.0 | 0.5 | 5 |
| WC+Stellite 21 | mild steel | 400°C, oxy-fuel torch | 2.0 – 4.0 | 0.5 | 5 |

In order to study the single-bead as well as the multiple-bead cladding condition, the following cladding strategy has been carried out: a single-bead clad of 80 mm length, partially overlapped (overlap of 6 mm) by a clad of 40 mm length (Figure 2.2).

*Figure 2.2. Typical sample produced showing the selected cladding strategy*

## 2.5 Coatings characterization

### 2.5.1 Microhardness and hardness

The microhardness tests have been performed under a Paar MHT-4 Vickers micro-indenter. A 0.1 kg load has been applied for a time of 10 s. A minimum of 8 indentations have been executed for every tested sample. The samples have been cut in order to reveal the clad cross-section and have been prepared through the classical metallographic procedure (i.e., polishing with papers and cloths and eventually etching).

The hardness tests have been carried out under an EmcoTest M4U 025 Rockwell indenter. A pre-load of 10 kg is applied for 2.5 s; then, a load of 150 kg is applied for 2.5 s (HRC). A minimum of 8 indentations have been executed for every tested sample. The samples have been prepared by surface polishing of the top of the clad.

Mean values and standard deviations have been calculated for every data batch.

### 2.5.2 Light Optical Microscopy (LOM)

A Zeiss Light Optical Microscope has been used for the optical characterization of the material microstructures. Digital images have been acquired by a Leica DC300 system connected to the microscope's optical system. The samples have been prepared through lapping and polishing with abrasive papers (220, 500, 800, 1200 and 4000 respectively) and diamond cloths (6, 3 and 1 μm respectively).

An electrolytic etching has been carried out. On the Co alloy, the electrolytic etching has been performed in a water solution of nitric acid (4,5 vol.%) and hydrogen peroxide (1,5 vol.%) applying a potential difference of 4 V for a time of 5 - 60 s. On the Ni and Fe alloys, the electrolytic etching has been performed in a water solution of oxalic acid (10 vol.%) applying a potential difference of 6 V for a time of 5 - 60 s.

### 2.5.3 Image Analysis

The image analysis software ImageJ has been used to measure the main geometrical features of the clad-cross section as schematically represented by Figure 1.18 in Chapter 1.5.1. In case of the coatings with tungsten carbides, image analysis has been utilized to investigate dissolution (see Appendix 1).

## 2.5.4 Scanning Electron Microscopy (SEM) and Energy-Dispersive X-ray Spectroscopy (EDXS)

A Philips XL30 Scanning Electron Microscope (SEM), operating in high vacuum atmosphere, has been used for the observation of the solidification microstructures and microstructural details (e.g., carbides in WC + Co-based alloy coatings, oxidation scale in In625 coatings, and so on).
The scanning electron microscope was equipped with an Energy-Dispersive X-ray Spectroscopy (EDXS) device, which has been used for the microstructure and microstructural details investigation and for the study of dilution (see Appendix 2).

### 2.5.5 X-Ray Diffraction (XRD)

X-Ray Diffraction (XRD) analysis was done using a Cu-k α source ($\lambda = 1.5418$ Å), and an Image Plate (IP) over the 2θ-range from 30° to 120°, in reflection geometry. The experimental patterns were elaborated with the Rietveld method using the MAUD (Materials Analysis Using Diffraction) software.

### 2.5.6 Calorimetric experiment

The calorimetric tests have been performed in-situ during laser cladding experiments, by measuring the temperature of the sample during cooling (see Appendix 3). For the temperature measurement, two S-type thermocouples have been used. Thermocouples have been connected to an Intab AAC-2 data logger for the data acquisition. Data analysis has been realized by the LabVIEW 7.0 software.

### 2.5.7 Thermogravimetric Analysis (TGA)

Thermogravimetric Analysis (TGA) has been carried out in a Netzsch 409-PC apparatus. Alumina crucibles have been employed.

Thermogravimetric Analysis (TGA) has been performed to study the thermal oxidation behaviour of the In625 coatings. For this purpose, isothermal treatments for 3 hours at different temperatures (1100, 1150 and 1200°C) have been made and a constant air flux (100 ml/min) has been insufflated during the test. A heating rate of 40 °C/min and a cooling rate of 50 °C/min have been applied in order to reach the desired temperature and, subsequently, to cool down the sample. A subtraction curve has been acquired on the empty crucible for each measurement.

## 2.6 Powders characterization

### 2.6.1 Density

The density of the different powders used has been determined using an AccuPyc II 1340 Gas Pycnometer. The instrument has been installed and calibrated to measure density according to the ASTM B923-10 standard.

### 2.6.2 Normal spectral absorbance

Normal spectral absorbance has been measured with an Ocean Optics USB4000 optical spectrometer, which disperses and records the full reflected spectrum within an integration time of 10 second. Radiation has been created by a DH2000-S Deuterium Tungsten Halogen Light Sources. Three indentations have been executed for every tested powder (see Appendix 4).

### 2.6.3 Differential Scanning Calorimetry (DSC)

The Differential Scanning Calorimetry (DSC) have been carried out in a Netzsch 409-PC apparatus. Alumina crucibles have been employed.
The Differential Scanning Calorimetry (DSC) has been performed to characterize the thermal behaviour of the powders used up to the melting temperature. A heating rate of 20 °C/min and a cooling rate of 50 °C/min have been applied and a constant argon flux (100 ml/min) has been insufflated during the test in order to avoid oxidation.

# Chapter 3
# Results and discussion

As seen in Chapter 1.4, the three principal processing parameters in the laser cladding process are the laser power, the scan speed and the feeding rate. The reason is their large effect on the final characteristics of the coating such us geometry, dilution, microstructure, presence of defects, particles dissolution, process efficiency and so on. In the following chapters, the effects of the principal processing parameters on geometrical features, dilution, energetic and material efficiency are investigated for different cladding materials. In particular, physical/analytical models to estimate the final geometrical characteristics and to evaluate the optimal processing conditions are proposed. The possible influence of the substrate (chemical composition or preheating) on the validity of these models is investigated. Finally, the properties of the coatings produced in different processing conditions are analysed. The effect of important parameters such us dilution and, in the case of MMC, carbide dissolution is considered and discussed.

## 3.1 Geometry

The effect of a single process parameter on the main geometrical features of the clad (i.e. height $H$, width $W$ and in turn aspect ratio $W/H$ of the bead) can be seen in Figure 3.1, where different clads of In625 were deposited on a mild steel by varying one of the principal parameters and keeping constants the other two.

On increasing the feeding rate, height of the clad increases while width remains basically the same. As a consequence, aspect ratio of the bead increases. On the opposite, on increasing the scan speed both the height and the width of the clad decrease. Aspect ratio increases since the decrease in the clad height is more pronounced than the decrease in the clad width. Finally, on increasing the power of the laser, the width of the clad increases. Clad height slightly increases leading to a slight increase in the aspect ratio value.

Because of the complexity of the laser cladding process and the mutual interactions between processing parameters, combined parameters can give a better description of the correlations between parameters and final characteristics of the clads. To investigate the effect of combined parameters, clads with four different materials (NiBSi, 316L, In625 and Stellite1) have been produced on the same mild steel substrate in different processing conditions.
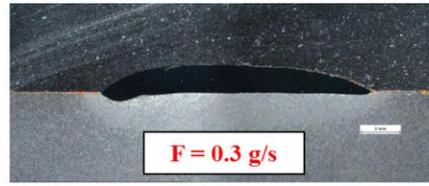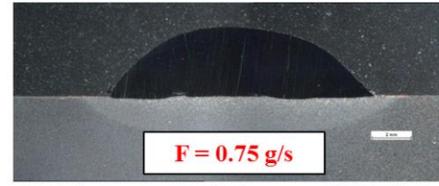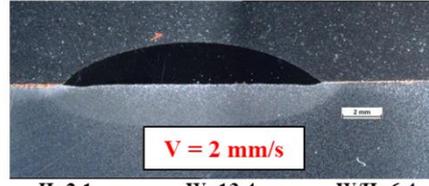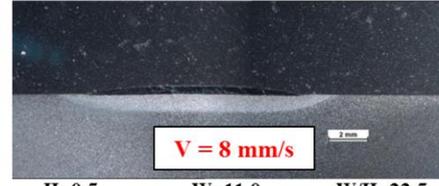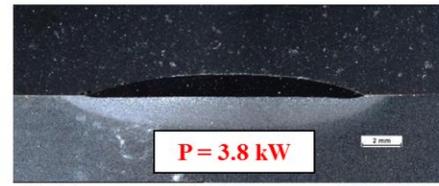
*Figure 3.1. Effect of a single process parameter on geometry of clads produced with In625.*

Clad height is linearly proportional to the powder density, defined as the ratio between the feed rate $F$ and the scan speed $V$ (Figure 3.2). Powder density represents the amount of material per mm length fed into the cladding system. Consequently, when no powder is injected into the system (i.e. $F/V = 0$), clad height is equal to 0. On increasing the material fed into the system, clad height increases linearly.
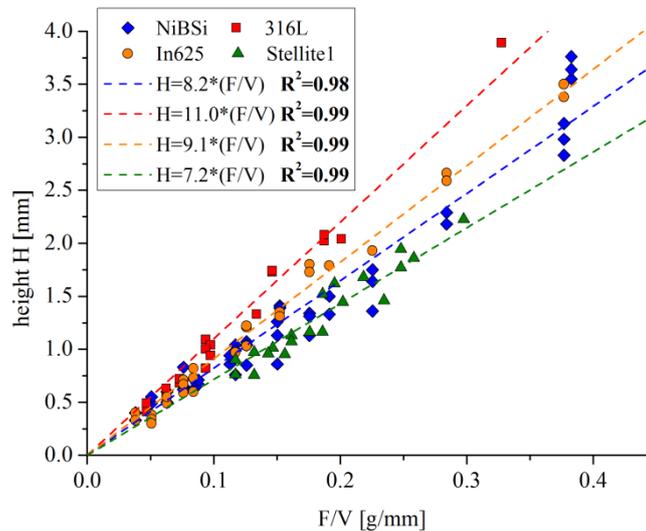


*Figure 3.2. Correlations between clad height and F/V for different powders.*

As shown in Figure 3.2, different correlations (different straight lines with different slopes) may be identified for the four cladding materials considered. In order to identify a univocal correlation between clad height and processing parameters, some considerations must be done.

The first consideration takes into account the powder loss during the process. As said before, $F/V$ represents the amount of material fed per mm length. Since not all the injected particles remain into the cladding system, the parameter "material efficiency" $\eta$ is introduced. Material efficiency

corresponds to the percentage of material that remains into the system with respect to the material injected and can be calculated by the following equation

$$\eta = 100 \cdot \frac{w_{s,a} - w_{s,b}}{w_i} \qquad (3.1)$$

where $w_{s,a}$ and $w_{s,b}$ are the weight of the sample after and before cladding respectively and $w_i$ is the weight of the powder injected, calculated as

$$w_i = \frac{F \cdot l}{V} \qquad (3.2)$$

where $l$ is the length of the clad bead.

Material efficiency depends on the processing parameters as well. The relationship between $\eta$ and the main process parameters has been estimated with the trial and error method (see Appendix 5), and the result of this calculation is reported in Figure 3.3.
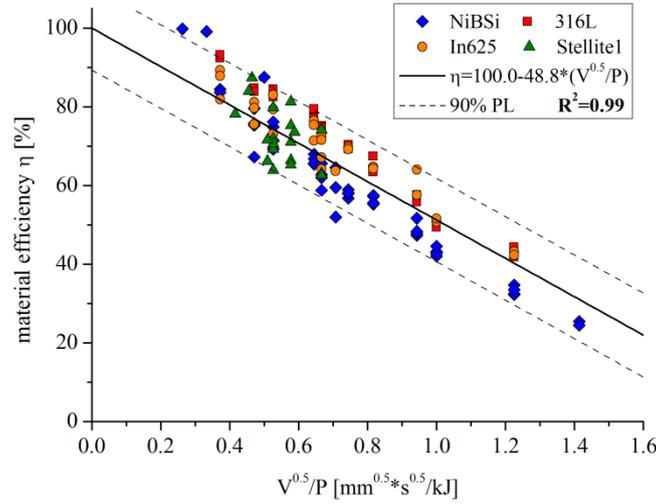


*Figure 3.3. Correlation between material efficiency and $V^{0.5}/P$.*

Independently from the cladding material, material efficiency depends on the scan speed and on the laser power, while it is not influenced by the feeding rate. In particular, material efficiency depends on the combined parameter $V^{0.5}/P$ through equation

$$\eta = 100 - 49 \cdot \frac{V^{0.5}}{P} \qquad (3.3)$$

A physical interpretation of this result will be given later (Chapter 3.4). However, material efficiency can be used to modify powder density: since $F/V$ represents the amount of material fed per mm length, the combined parameter $\eta F/V$ gives the effective powder mass remained into the system per mm length.

The second consideration takes into account the cladding material. As it can be seen in Figure 3.2, four different correlations between $H$ and $F/V$ can be identified according to the cladding material used. To consider the influence of the cladding material, the material density $\rho$ is introduced. Material density is a physical property of the material and it has been measured with a gas picnometer according to the

ASTM B923-10 standard. Measurements of the material density of the four different cladding materials are listed in Table 3.1.

*Table 3.1. Measured density of the four different cladding materials.*

| material | density [g/cm$^3$] |
|----------|--------------------|
| NiBSi | $8.27 \pm 0.01$ |
| 316L | $7.93 \pm 0.01$ |
| In625 | $8.45 \pm 0.01$ |
| Stellite1 | $8.57 \pm 0.01$ |

With the introduction of $\rho$, the combined parameters $\eta F/\rho V$ assumes a different meaning: expressed in mm$^3$/mm (or, for sake of simplicity, in mm$^2$), it becomes the effective powder volume remained into the system per mm length [99]. If no variation of the clad cross-section in the clad length is assumed, the parameter $\eta F/\rho V$ may identify the emerging part of the clad cross-sectional area $A_N$. This can be easily seen in Figure 3.4, where the measured values of $A_N$ are reported as a function of the parameter $\eta F/\rho V$. The distances of the data points from the bisector of the quadrant are qualitatively representative of the difference between the two measurements.
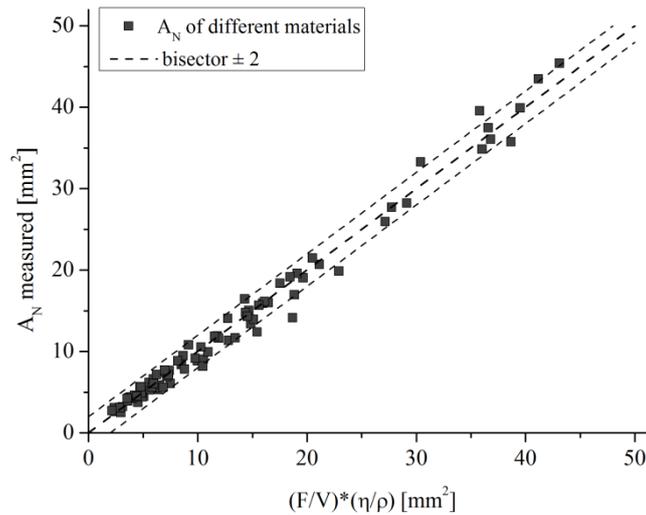


*Figure 3.4. Correlation between the measured clad cross-sectional area and the parameter $\eta F/\rho V$.*

The correlation between clad height and the combined parameter $\eta F/\rho V$ is shown in Figure 3.5. The height of the clad is proportional to the combined parameter $\eta F/\rho V$ or, alternatively, to the emerging clad cross-section $A_N$. This proportionality can be used to univocally estimate the height of the clad once the processing parameters and the cladding material are selected. The correlation between $H$ and $\eta F/\rho V$ is assumed to be linear and can be described by equation

$$H = k_0 \cdot \frac{F}{V} \cdot \frac{\eta}{\rho} \qquad (3.4)$$

where the constant of proportionality $k_0$, calculated with the optimization of the regression coefficient, results to be equal to 0.095.
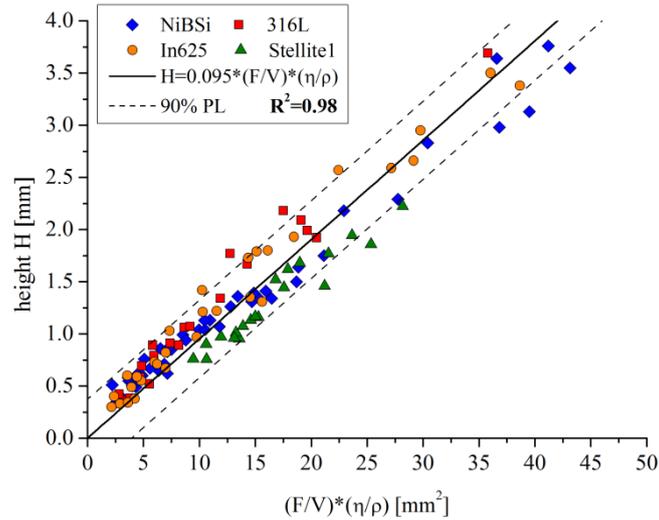
*Figure 3.5. Correlation between clad height and the parameter ηF/ρV.*

Clad height is correlated with the emerging cross-sectional area, and the emerging cross-sectional area is limited by height and width of the clad. For this reason it could be expected that also the clad width shows a correlation with the combined parameter *ηF/ρV*. When clad width is plotted as a function of *ηF/ρV*, no significant correlation can be revealed (Figure 3.6).
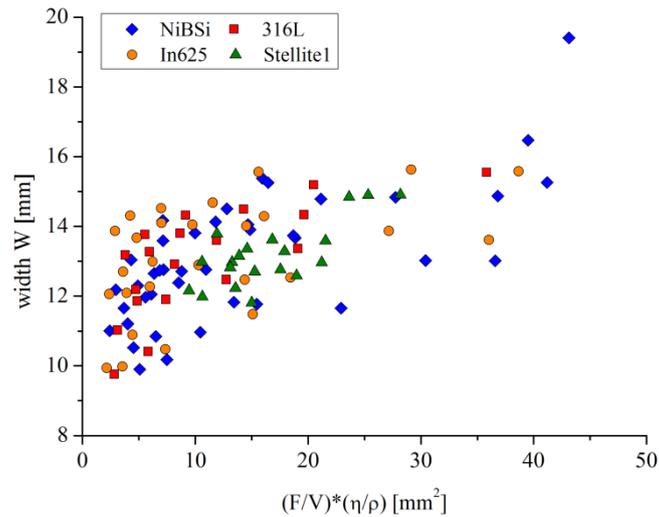


*Figure 3.6. Clad width as a function of the parameter ηF/ρV.*

The correlation between the width of the clad and the processing parameters is estimated again with the trial and error method (Figure 3.7) and represented by equation

$$W = 9.8 + 0.6 \cdot \frac{P^2}{V^{0.5}} \qquad (3.5)$$
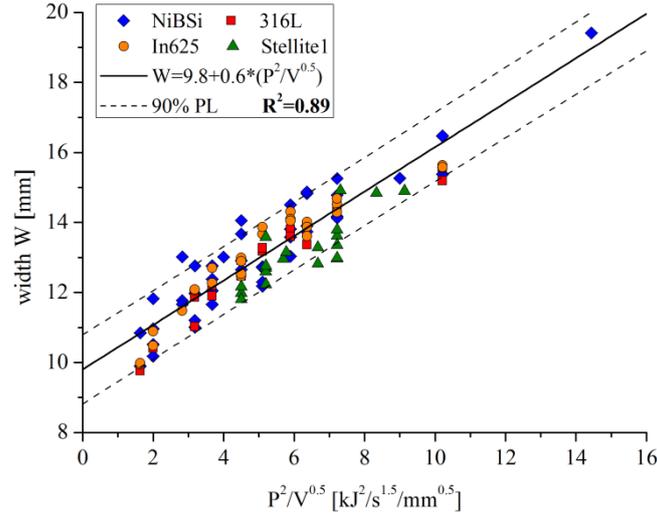
*Figure 3.7. Correlation between clad width and the parameter $P^2/V^{0.5}$.*

Clad width is not directly influenced by the powder density, but it is ruled by the combined parameter $P^2/V^{0.5}$. As well as for the material efficiency, this correlation is not influenced by the cladding material and by the feeding rate, but only by the laser power and the scan speed. The laser power, as it can be seen by the exponent of $P$ in equation (3.5), strongly affects clad width: on increasing the laser power, width of the clad gets larger. On the other hand, the faster is the scan speed, the lower is the clad width. The effect of the scan speed, with the exponent equal to 0.5, is lower.

It is interesting to notice that clad width values range approximatively between 10 and 19 mm. Even if the beam spot width is constant, processing parameters are able to modify the final width of the clad. Moreover, clad width can reach values higher than the width of the spot beam, which is equal to 12 mm.

Equations (3.4) and (3.5) to estimate clad width and height respectively allow the determination of the aspect ratio of the clad bead, defined as the ratio between the width and the height of the clad, through equation

$$\frac{W}{H} = \frac{9.8 + 0.6 \cdot \frac{P^2}{V^{0.5}}}{0.095 \cdot \frac{F}{V} \cdot \frac{\eta}{\rho}} \qquad (3.6)$$

Aspect ratio depends on the three processing parameters as well as the cladding material (through the material efficiency and its density). Due to the strong influence of the clad height on the aspect ratio, it can be said that *W/H* is mainly influenced by the powder density, which characterizes clad height. This is also visible when aspect ratio is plotted as a function of *F/V* (Figure 3.8).
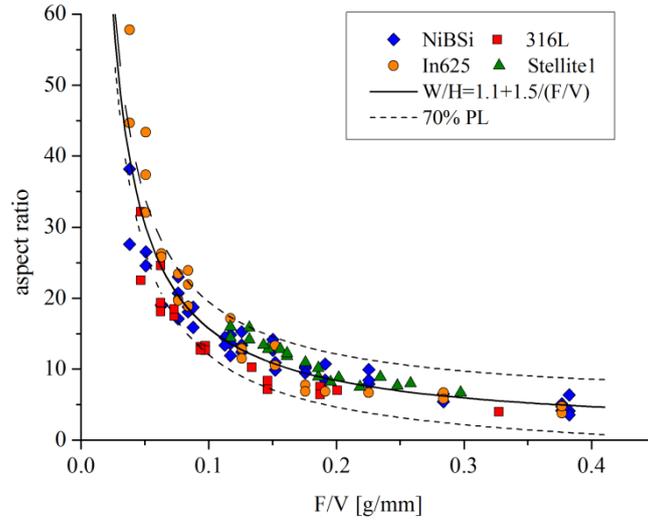
*Figure 3.8. Correlation between aspect ratio and the parameter F/V.*

However, a more complete correlation between processing conditions and aspect ratio, that takes into account also laser power and cladding material density, is described by equation (3.6). In Figure 3.9, the values of the aspect ratio estimated through equation (3.6) are reported as a function of the measured values.
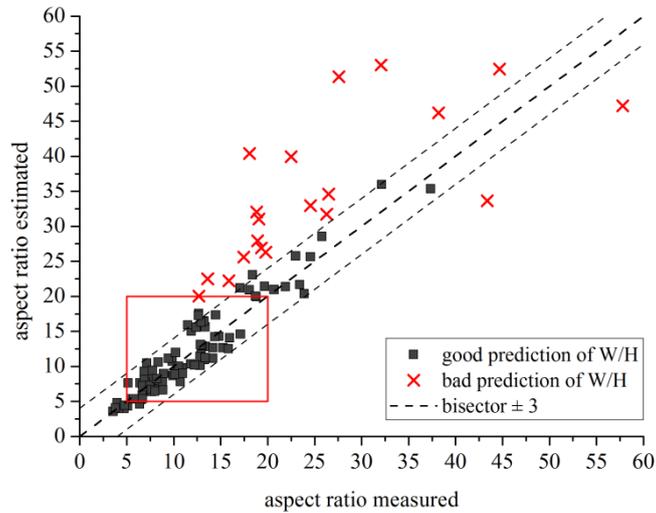


*Figure 3.9. Aspect ratio values estimated through equation (3.6) as a function of the measured values.*

According to Figure 3.9, aspect ratio can be well predicted up to the value of 20. Above this threshold value, prediction gets worse and data points start to fall away from the quadrant's bisector. The reason is mainly given by the small variations of clad height that cause large variations in clad aspect ratio, especially for high values of it.

Anyway, it has to be said that the typical values of the clad aspect ratio in laser cladding processes range between 5 and 20. When multiple-bead laser cladding is designed, aspect ratio must be higher than 5 to avoid inter-run porosity between adjacent beads. Moreover, aspect ratio value is generally kept lower than 20 to guarantee proper clad thickness and process productivity.

In this range, equation (3.6) can be used to evaluate the correlation between processing parameters and aspect ratio of the clad.

As said before, height and width of the clad can be estimated through equation (3.4) and (3.5) respectively. $H$ is proportional to the emerging cross section of the clad $A_N$, while no proportionality is found between $W$ and $A_N$. However, a complex correlation between both the width and the height of the clad and the emerging cross-sectional area exists. To describe the change in the emerging clad cross-sectional area with respect to $W$ and $H$, the Simpson's rule is used. In this approach, the emerging cross-section is considered as a portion of a circle where the secant line of the circle is defined by the original surface of the substrate and the chord of the circle, consequently, represents the width of the clad. Figure 3.10 shows a schematic of the emerging cross-sectional area of the clad ($A_N$) and the accompanying virtual circle created below the substrate $A_2$ [140].
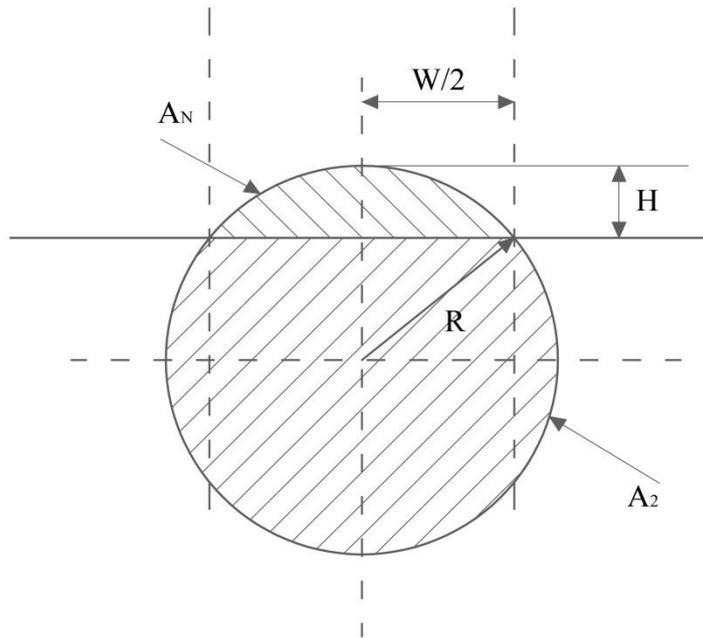


*Figure 3.10. Schematic of the emerging cross-sectional area of the clad ($A_N$) and the accompanying virtual circle created below the substrate $A_2$ [140].*

$A_N$ can be thus estimated through equation

$$A_N = \frac{H}{3} \cdot \left( \frac{W}{2} + 2 \cdot \sqrt{(W/2)^2 + H^2} \right) \qquad (3.7)$$

which is a well-known approximation for a definite integral proposed by Simpson. This assumption is valid only for values of $H$ smaller than $W/2$, condition which is amply satisfied in any case of this study [140].

Using the measured values of $H$ and $W$, $A_N$ has been calculated with equation (3.7) and then compared with the measured values of $A_N$ (Figure 3.11).
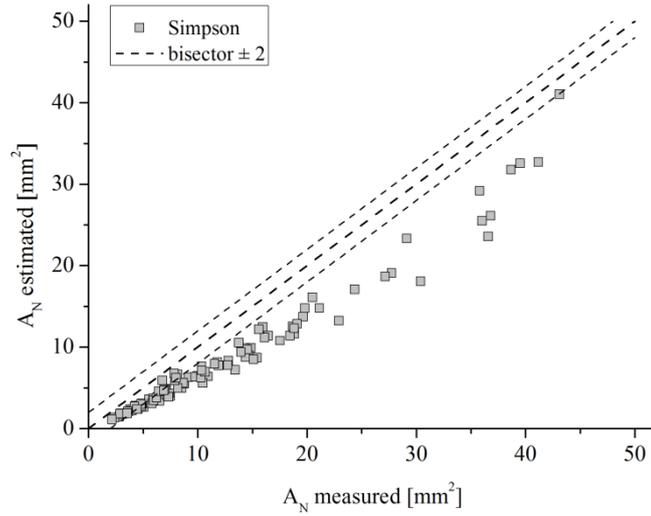
*Figure 3.11. Comparison between clad cross-sectional area estimated with Simpson's model and measured.*

There is a clear correlation between the values of $A_N$ estimated with Simpson's equation (3.7) and the measured ones, but data points deviate from the Simpson model (Figure 3.11). This is mainly due to the fact that clads are not portions of a circle, as stated with this approach. Equation (3.7) has been analytically modified using correction coefficients $k_1$ and $k_2$ in equation

$$A_N = k_1 \cdot \left[ \frac{H}{6} \cdot \left( \frac{W}{2} + 2 \cdot \sqrt{(W/2)^2 + H^2} \right) \right]^{k_2} \qquad (3.8)$$

Values of $k_1$ and $k_2$ have been obtained by residuals minimization ($k_1$=2.1 and $k_1$=0.85) and results of this modification are visible in Figure 3.12.
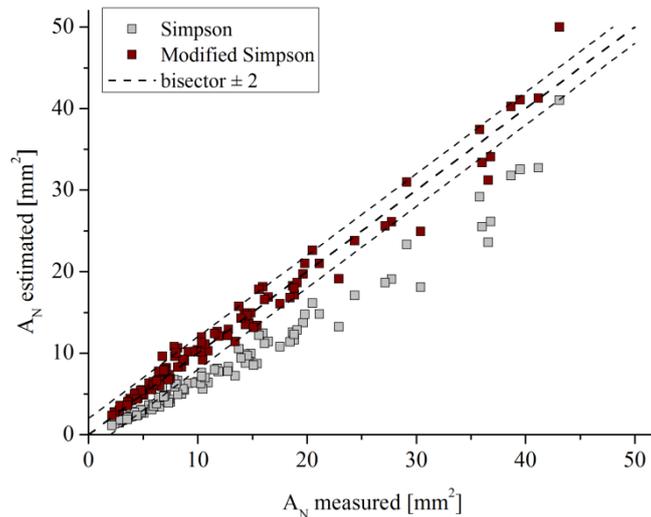


*Figure 3.12. Comparison between clad cross-sectional area estimated with Simpson's equation (3.7), modified Simpson's equation (3.8) and measured.*

Modified Simpson's equation (3.8) can be utilized to describe the change in the emerging clad cross-sectional area with respect to W and H. This allows to draw a helpful graph like the one shown in Figure 3.13, where the y-axis represents clad width and the x-axis represents clad height.
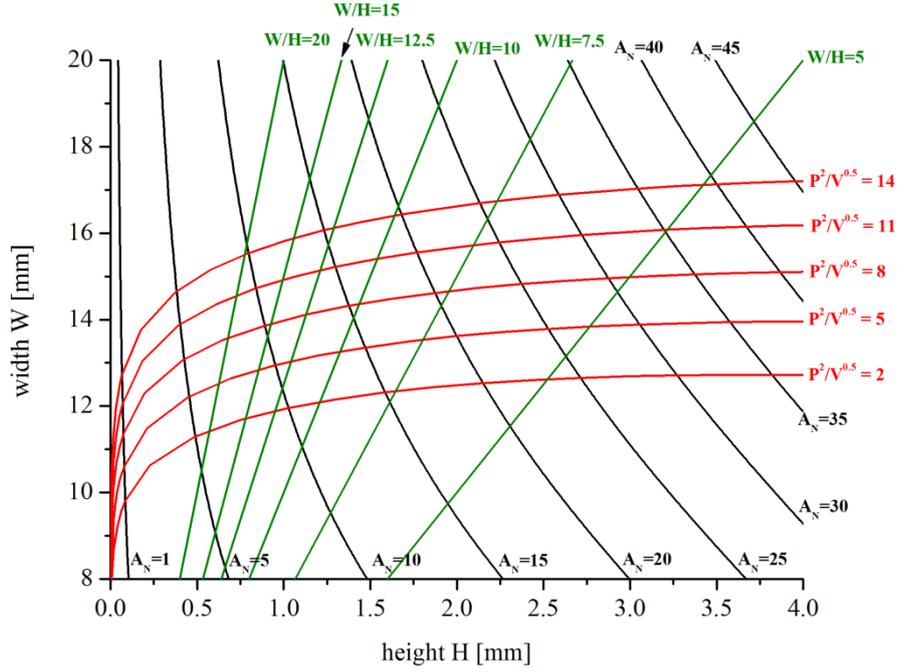
*Figure 3.13. Clad width vs. clad height where are reported: curves calculated with modified Simpson's equation (3.8) for different values of $A_N$ (black curves); curves calculated with aspect ratio equation (3.6) for different values of $P^2/V^{0.5}$ (red curves); lines for different values of aspect ratio (green lines).*

In this graph, modified Simpson's equations (3.8) calculated for different values of $A_N$ are represented by the black curves, while the red curves represent aspect ratio equations (3.6) calculated for different values of $P^2/V^{0.5}$.

For a defined value of $A_N$, which can be calculated once processing parameters, material efficiency and cladding material density are known, the corresponding black curve gives all the possible combinations of width and height that satisfy the modified Simpson's model. Among all the possible solutions, the identification of the ($H;W$) couple that describes the clad geometry can be done with the combined parameter $P^2/V^{0.5}$, and thus with the proper red curve. The intersection between the black curve and the red curve, both selected once cladding conditions are decided, gives the final height and width of the clad. Consequently, final clad aspect ratio can be identified (green straight lines).

## 3.2 Dilution

Definition of dilution has been reported and validated in Appendix 2. In this thesis work, dilution is defined as

$$D = \frac{A_D}{A_N + A_D} \cdot 100 \qquad (3.9)$$

where $A_D$ represents the diluted part of the cross-sectional area (i.e. the part submerged below the original surface of the substrate). In this case, dilution is expressed as a percentage value.

The correlation between processing parameters and dilution has been investigated with the trial and error method, firstly on the four materials considered separately, then on all the data together.

When the four materials are considered separately, the following equation can be used to estimate dilution as a function of the main processing parameters

$$D = m \cdot \frac{P^x \cdot V^y}{F^z} \qquad (3.10)$$

where the calculated values of $m$, $x$, $y$ and $z$ are reported in Table 3.2 for the different cladding materials. Graphical results of these analysis are reported in Figure 3.14.

*Table 3.2. Calculated values of m, x, y and z of equation (3.10) for different cladding materials.*

| material | m | x | y | z |
|----------|------|-----|-----|-----|
| NiBSi | 0.52 | 1 | 0.5 | 1.5 |
| 316L | 0.06 | 1.5 | 1 | 2 |
| In625 | 0.19 | 2 | 0.5 | 1.5 |
| Stellite1 | 0.004 | 3.5 | 0.5 | 4 |
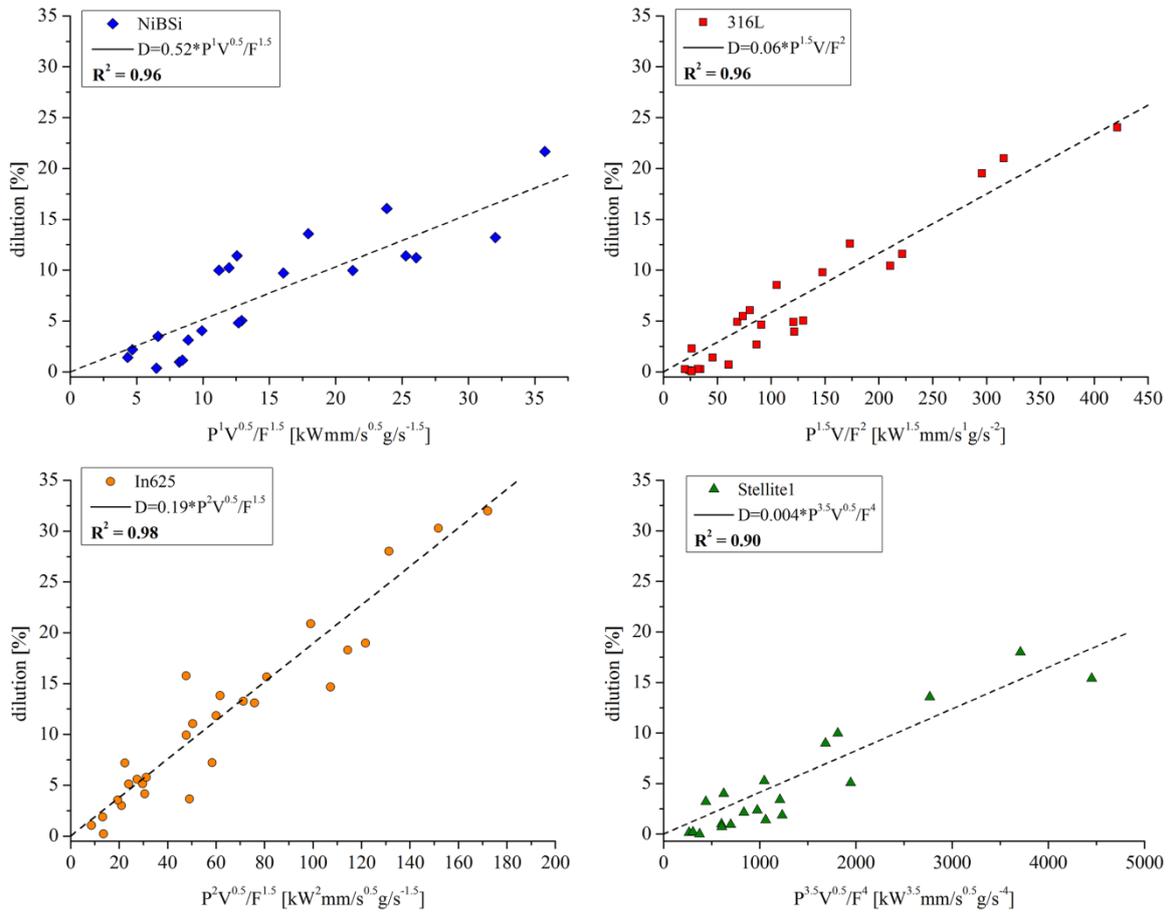


*Figure 3.14. Linear correlations between dilution D and the opportune combined parameter for the different materials.*

The values of the exponents $x$, $y$ and $z$, which maximize the regression coefficient of equation (3.10), differ from batch to batch according to the different cladding materials utilized. As a consequence,

angular coefficient *m* differs as well. Even if all these values are different, some considerations can still be done.

For all the four batches *P* and *V* are parts of the numerator while *F* is part of the denominator: an increase in the laser power and in the scan speed lead to an increase in dilution, while an increase in the feeding rate tends to decrease dilution. The main trends of these processing parameters on dilution have been confirmed by other works present in literature. For instance, Olivera et al. [91] found that the combined parameter to control dilution in coaxial cladding is $P^{0.5} \cdot V^{0.5}/F^{0.5}$, while for side cladding was found to be $P \cdot V/F$ by Felde et al. [101] and $ln(P \cdot V^{0.5}/F^{0.5})$ by Ocelik et al. [92].

From a physical point of view, these behaviours can be explained through energy transmission phenomena. Laser power tends to increase dilution since it increases the total energy in the system, and consequently the energy conducted through the substrate, which is responsible of dilution. With the increase in the feeding rate, on the other hand, the mass of material into the system increases and therefore the energy conducted through the substrate decreases, leading to a lower dilution. The effect of the scan speed is double: on increasing the scan speed, both the combined parameters *P/V* and *F/V* diminish, leading to a decrease in the J/mm and the g/mm available in the system: when a constant length is considered, a lower mass of material hinders transmission through the substrate but at the same time less energy is available. Since these effects are concurrent, a variation in the scan speed is less effective on dilution than a change in the laser power or in the feeding rate. This is confirmed by experimental values of the y exponents in equation (3.10), that are always lower than x and z as shown in Table 3.3. Moreover, since increasing scan speed results in an increasing clad dilution, it can be stated that the effect of the scan speed on *F/V* prevail on the effect on *P/V*.

When all the data are considered together (i.e. the effect of the cladding material on dilution is neglected), the coefficients *m*, *x*, *y* and *z* in equation (3.10) becomes as reported in Table 3.3.

*Table 3.3. Calculated values of m, x, y and z of equation (3.10) for the data considered together.*

| material | m | x | y | z |
|---|---|---|---|---|
| data together | 0.17 | 1.5 | 0.5 | 2 |

Graphical result is shown in Figure 3.15.
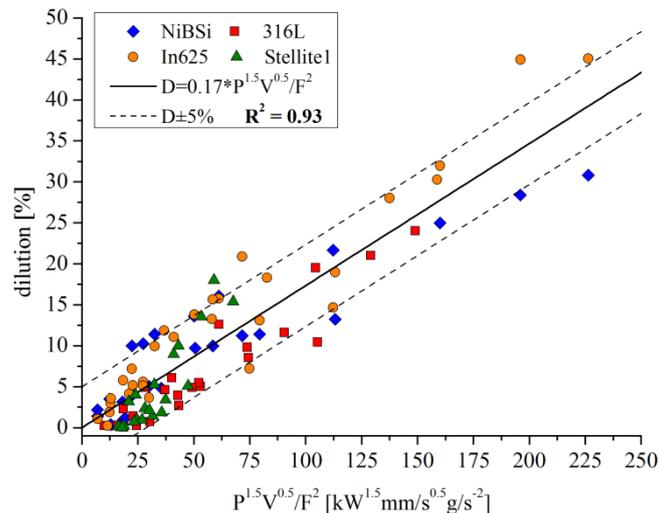


*Figure 3.15. Correlation between dilution D and the parameter $P^{1.5}V^{0.5}/F^2$.*

Regression coefficient is maximized ($R^2=0.93$) when *x = 1.5*, *y = 0.5* and *z = 2*. This confirms all the considerations that have been done on the four batches considered separately. Equation (3.10) may be used, within a certain approximation, to predict dilution independently from the cladding material as a function of the processing parameters.

## 3.3 Geometry and dilution: processing map

Clad aspect ratio and dilution are two of the most important features when designing the laser cladding process. As anticipated, the typical value of aspect ratio range lies between 5 and 20: aspect ratio must be higher than 5 to avoid inter-run porosity between adjacent beads, while 20 is usually taken as maximum value to guarantee proper clad thickness and process productivity. Dilution is generally kept between 2 and 5%: some dilution is necessary to have a good metallurgical bond between substrate and clad, but too much dilution can influence the properties of the cladding material negatively. However, a higher percentage of dilution can be allowed if the variation of the chemical composition of the cladding material does not affect the desired properties of the final coating.

Aspect ratio and dilution dependences on the processing parameters have been described with equation (3.6) and (3.10) respectively. Once the desired boundary conditions for both aspect ratio and dilution are selected, these equations can be plotted together on a 3D-graph like the one shown in Figure 3.16, where the three axis represent the laser power, the scan speed and the feeding rate.
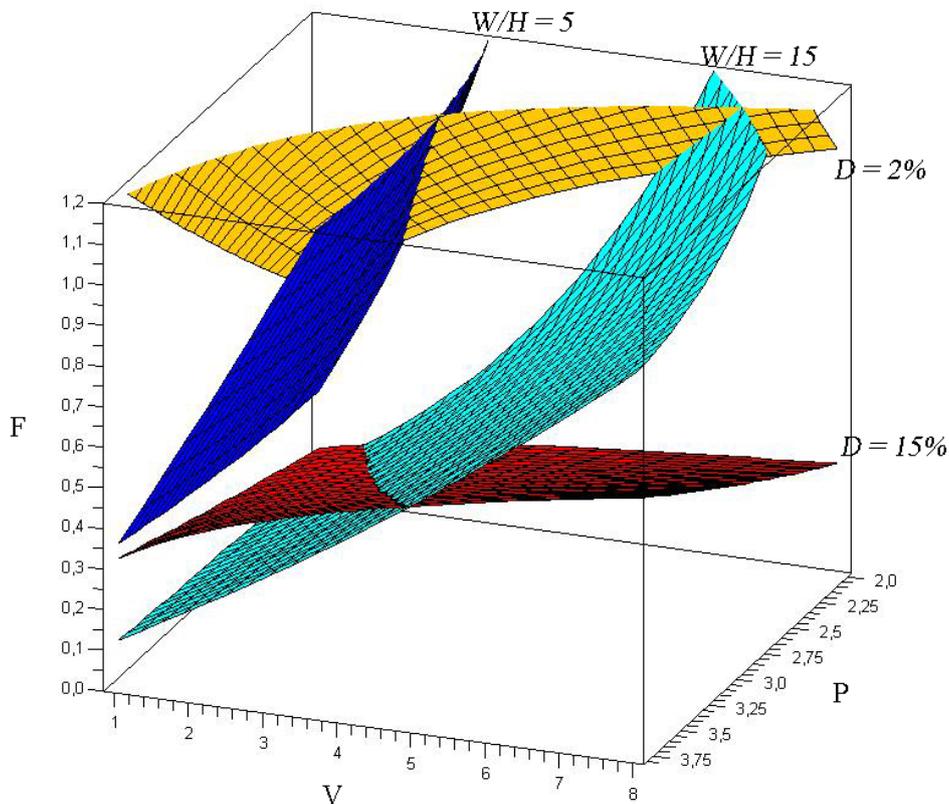


*Figure 3.16. Laser power, scan speed and feeding rate 3D-graph with iso-dilution and iso-aspect ratio surfaces: (D=2%, yellow; D=15%, red; W/H=5, blue, W/H=15, cyan).*

The surfaces represented in Figure 3.16 are the so called iso-dilution and iso-aspect ratio surfaces, i.e. the set of all the possible combination of $P$, $V$ and $F$ that allow the production of a clad with the desired value of dilution or aspect ratio respectively. For instance, in Figure 3.16 are reported the equations for values of dilution set to 2% and 15% and the equations for values of aspect ratio set to 5 and 15 for the coatings produced with the NiBSi alloy. Intersections between surfaces, moreover, give the values of laser power, scan speed and feeding rate to obtain a clad with both a defined aspect ratio and amount of dilution. A tool like this is be very useful to define the possible processing window according to the desired final properties of the coatings.

## 3.4  Material efficiency

Material efficiency is the coefficient that defines how much of the injected powder remains into the melt pool to form the clad. Its value ranges between 0, when all the powder injected is lost, and 1, when all the powder particles are captured into the melt pool.

As described in Chapter 1.3.2, the condition that determines whether the delivered powder sticks to the cladding zone to form the clad or not is defined by the type of impact: the powder particles that strike on a solid surface ricochet and are lost, while the particles impinging on the liquid surface of the melt pool are captured and participate in the formation of the clad. For this reason, material efficiency can be simply defined geometrically with equation

$$\eta = \frac{A_{mp}}{A_{pj}} \qquad (3.11)$$

where $A_{mp}$ is the melt pool area and $A_{pj}$ is the section of the powder jet when it reaches the melt pool [99]. When the area of the melt pool is smaller than the section of the powder jet, some powder particles are not injected into the melt pool but on the solid surface of the substrate, they thus ricochet and are lost: material efficiency, as a consequence, is lower than 1. When the area of the melt pool is higher than the one of the powder jet, all the powder particles are directed into the melt pool and material efficiency is maximized ($\eta = 1$).

The measured values of material efficiency and melt pool area have been compared in Figure 3.17.

As supposed, an increase in the melt pool area leads to an increase in material efficiency since these two quantities are proportional. However, the correlation between $\eta$ and $A_{mp}$ is not linear: the area of the powder jet $A_{pj}$ is not a constant in this process, and must be influenced by the processing parameters.

Due to the complex geometry of the feeding system used, no direct information on $A_{pj}$ are available. However, the correlations between melt pool dimensions and melt pool area together with the effect of processing parameters on these quantities have been investigated in order to clarify equation (3.11).
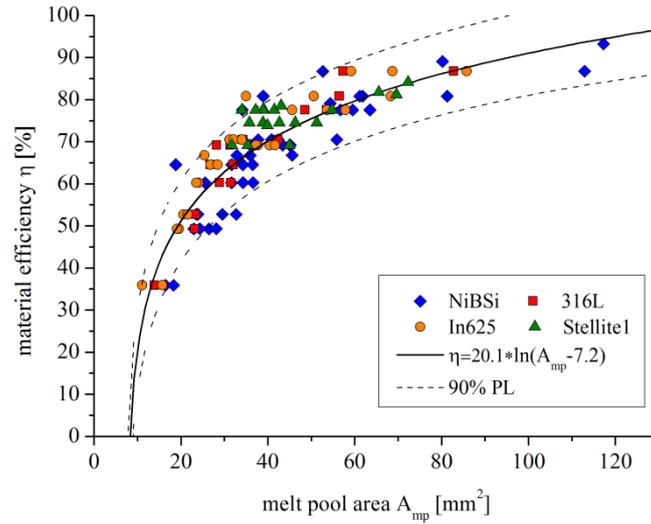
*Figure 3.17. Correlation between material efficiency and melt pool area.*

The area of the melt pool is schematically illustrated by Figure 3.18, where the top-view and the side-view of the last part of a single bead clad are reported. The last part of the produced clads is in fact representative of the melt pool size, shape and orientation during the deposition of the clad, since at this very moment the laser and the powder jet have been simultaneously switched off.
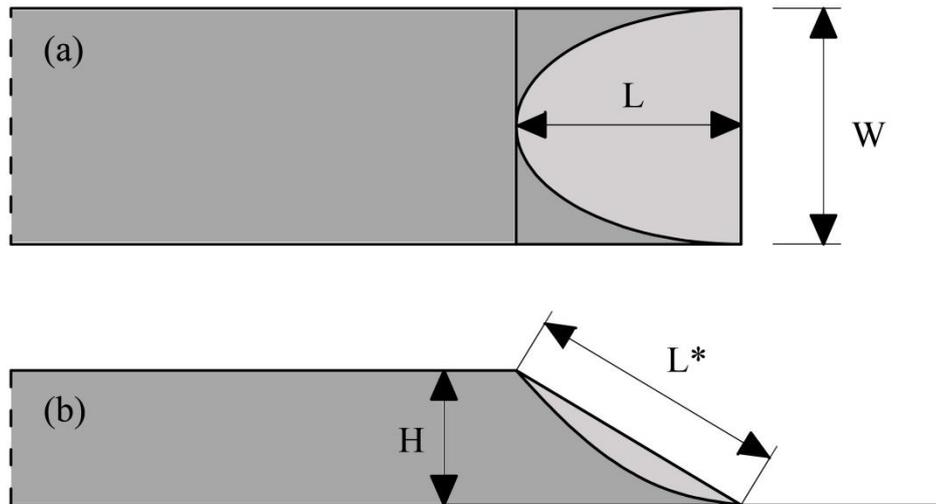


*Figure 3.18. Schematic of melt pool area: (a) top-view and (b) side-view of the last part of a single bead clad.*

According to the Figure 3.18, the area of the melt pool is assumed to be identified with the area of a semi-ellipse having the semi-major axis equal to the semi-width of the clad (*W/2*) and the semi-minor axis equal to $L^*$, defined as the real length of the molten pool. The measure of $L^*$ can be obtained through equation

$$L^* = \sqrt{L^2 + H^2} \qquad (3.12)$$

where *H* is clad height and *L* is the length of the melt pool in the longitudinal direction (i.e. parallel to the scanning direction). Under this assumption, the equation to estimate the area of the melt pool using its dimensions is

49

$$A_{mp} = \frac{\pi}{4} \cdot W \cdot L^*  \qquad (3.13)$$

The correspondence between the values of the melt pool area measured with image analysis and those estimated with equation (3.13) is satisfactory, as it can be seen in Figure 3.19.
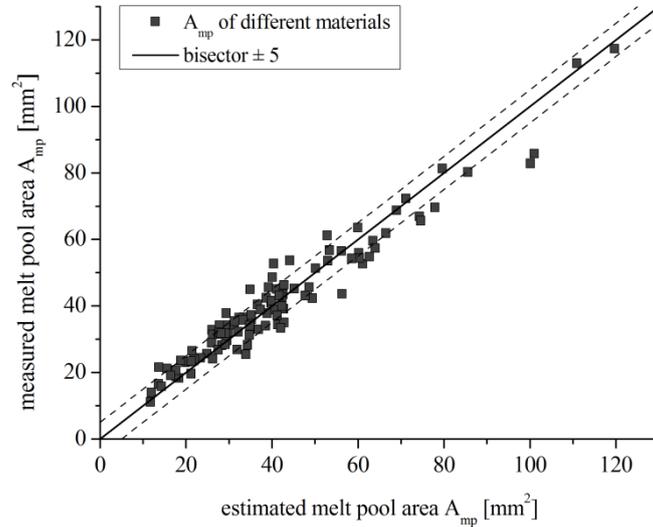


*Figure 3.19. Comparison between measured melt pool area and melt pool area estimated with equation (3.13).*

As expected, the area of the melt pool is directly proportional to the length of the melt pool and to the width of the clad, which corresponds to the width of the melt pool.

Through equation (3.13), correlation between processing parameters and the area of the melt pool can be easily explained. As seen in the previous paragraphs, width of the clad has been calculated with the trial and error method as proportional to the combined parameter $P^2/V^{0.5}$. With the same method, influence of processing parameters on the length of the melt pool ($L^*$) is obtained (Figure 3.20).
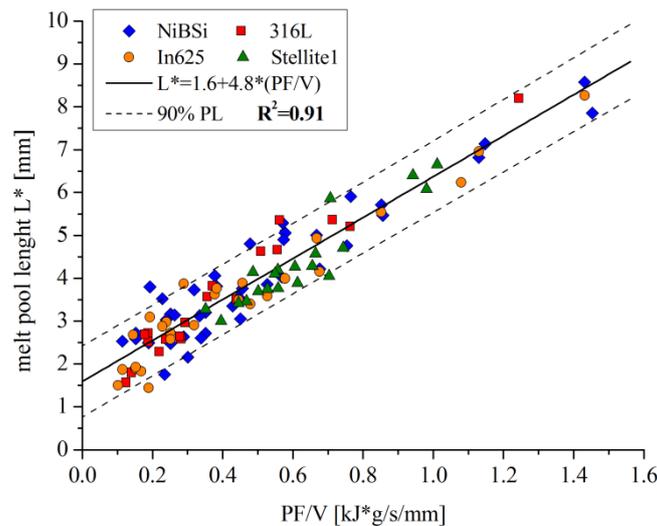


*Figure 3.20. Correlation between melt pool length L\* and the parameter PF/V.*

Independently from the cladding material, the length of the melt pool depends on the combined parameter *PF/V* through equation

$$L^* = 1.6 + 4.8 \cdot \frac{P \cdot F}{V} \qquad (3.14)$$

Both melt pool width and length increase on increasing the laser power and on decreasing the scan speed. Moreover, an increase in the feeding rate leads to an increase in the length of the melt pool. When trial and error method is applied on the measured values of $A_{mp}$, these correlations are confirmed: melt pool area is linearly proportional to the combined parameter $P^2F/V$ (Figure 3.21).
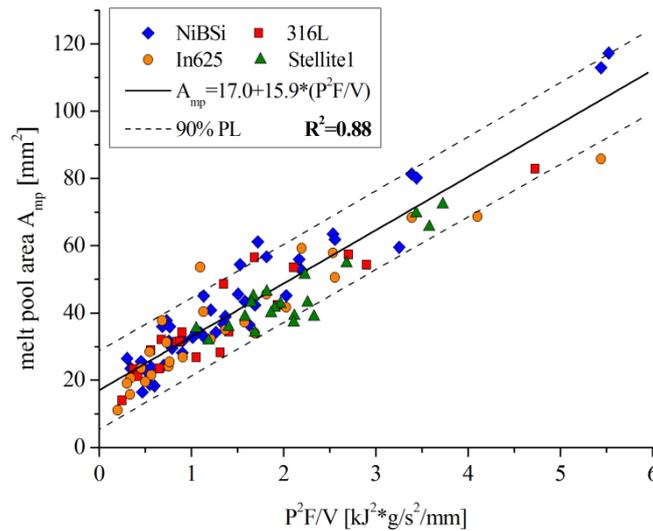


*Figure 3.21. Correlation between melt pool area and the parameter $P^2F/V$.*

The following equation

$$A_{mp} = 17.0 + 15.9 \cdot \frac{P^2 \cdot F}{V} \qquad (3.15)$$

can be used, independently from the cladding material, to correlate the molten pool area with the processing parameters.

Since both the melt pool area and the material efficiency have been measured, values of $A_{pj}$ have been calculated through equation (3.11), and the possible effect of the processing parameters has been investigated. Assuming that the only main processing parameters that can modify the powder jet are the feeding rate and the scan speed, the laser power has been rejected as a possible influencing parameter.

With a certain limitation on the calculated regression coefficient ($R^2 = 0.57$), the combined parameter which maximizes $R^2$ is the powder density (*F/V*) (Figure 3.22).
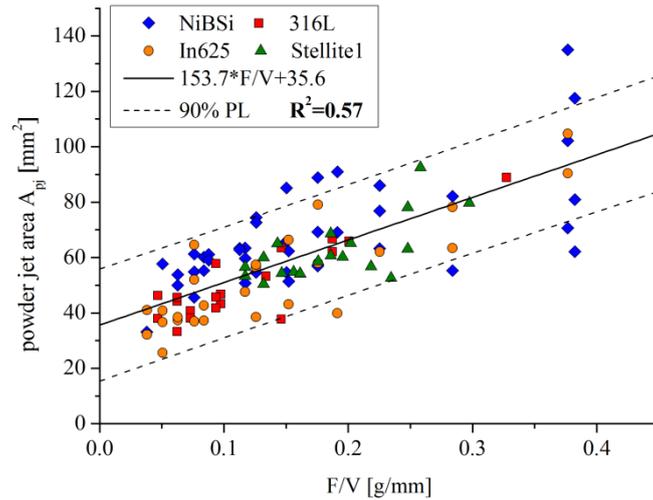
*Figure 3.22. Correlation between the projected area of the powder clad $A_{pj}$ and the parameter F/V.*

If the correlation between $A_{pj}$ and the parameter *F/V* is assumed to be valid, when the grams per millimetre of injected material are increased, a generally larger area can be covered by the powder particles.

Even if the feeding rate *F* affects both the powder jet and the melt pool dimensions, the effect of this processing parameter does not seem to be reflected on the material efficiency. Indeed, when the trial and error method has been applied on the measured values of material efficiency, no influence of the feeding rate is highlighted: the effect of the feeding rate on increasing the powder jet dimension in balanced by its tendency to increase the area of the melt pool. As stated in equation (3.3), material efficiency is only influenced by the combined parameter $V^{0.5}/P$.

## 3.5 Effect of substrate and preheating treatment on geometry and dilution models

In the previous chapters, models to estimate clad geometry and dilution as a function of the processing parameters for different cladding materials have been defined. The possible influence of substrate material or condition has not been taken in consideration, since the same mild steel substrate at room temperature have been utilized. In this chapter, the effect of substrate preheating and different chemical composition of the substrate are investigated. Two batches have been produced cladding the NiBSi alloy onto the mild steel substrate preheated at 400°C and onto the grey cast iron substrate preheated at 400°C. Results of these batches have been compared with those obtained from cladding the NiBSi alloy onto the mild steel substrate.

In Figure 3.23 the measured values of height, width, material efficiency and dilution of the clads produced on the preheated mild steel are reported together with the previously obtained equations (3.4), (3.5), (3.10) and (3.3), which give the correlation between the cited properties and the processing parameters when substrate is not preheated.
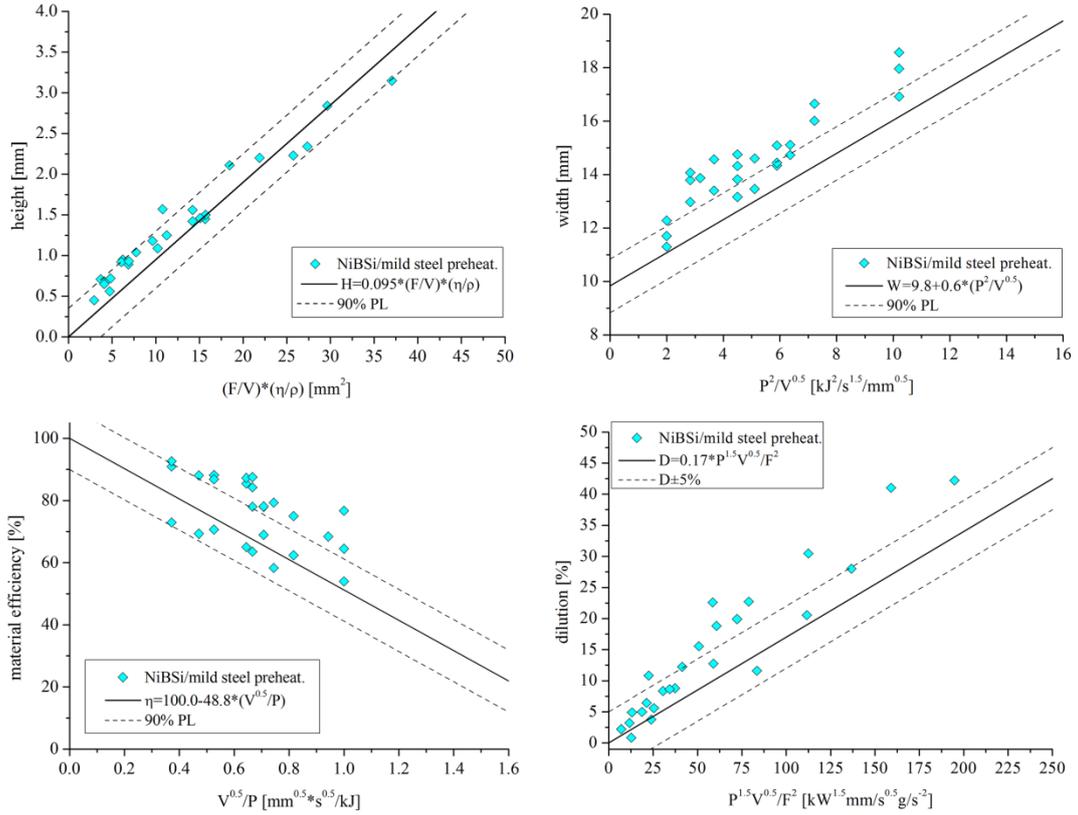
*Figure 3.23. Height, width, material efficiency and dilution of the clads produced on the preheated mild steel reported together with the previously obtained correlations.*

Clad height prediction does not seem to be influenced by substrate preheating. Data points falls close to the straight line representing equation (3.4), or at least in the acceptable region. On the other hand, predictions of clad width, dilution and material efficiency are slightly affected by the preheating of the substrate. Most of the data points, in fact, lies above the three straight lines used to represent equations (3.5), (3.10) and (3.3): when two clads are produced with the same laser power and the same scan speed, clads produced on a preheated substrate tend to be wider than those produced on a not preheated substrate, and material efficiency in the case of preheated substrate results to be higher. In addition, when the three main processing parameters are the same, preheating the substrate leads to an increase in dilution percentage.

From a physical point of view, substrate preheating can be seen like a surplus of energy given to the cladding system: a higher amount of energy available leads to higher energy transferred to the substrate (which means higher dilution), larger melt pool area (which means higher material efficiency) and higher temperature reached by the melt pool (which generates higher wettability and wider clads). Since the usable energy in the laser cladding process is mostly determined by the laser power, a simple approach is proposed: the effective laser power available by the cladding system when the substrate is preheated ($P_{eff}$) is equal to

$$P_{eff} = P + P_{pr} \qquad (3.16)$$

where $P$ is the input power and $P_{pr}$ is the extra amount of power available by the system due to substrate preheating.

This consideration is further confirmed by the dependencies of the clad properties on the processing parameters, and in particular on the laser power. Material efficiency, dilution and clad width, which

are influenced by the laser power, are sensitive to substrate preheating. In specific, an increase in the available laser power generates higher values of $\eta$, $D$ and $W$, as revealed by experimental results. Clad height, which is only partially influenced by the power of the laser through the material efficiency, remains basically the same whether the substrate is preheated or not.

Under this assumption, the equations that correlate the processing parameters with the clad properties considered have to be opportunely modified using equation (3.16). In case of substrate preheating, the following equations can be used to estimate material efficiency, clad height, clad width and clad dilution respectively

$$\eta_{pr} = 100 - 49 \cdot \frac{V^{0.5}}{P_{eff}} \qquad (3.17)$$

$$H_{pr} = k_0 \cdot \frac{F}{V} \cdot \frac{\eta_{pr}}{\rho} \qquad (3.18)$$

$$W_{pr} = 9.8 + 0.6 \cdot \frac{P_{eff}^2}{V^{0.5}} \qquad (3.19)$$

$$D_{pr} = m \cdot \frac{P_{eff}^{x} \cdot V^y}{F^z} \qquad (3.20)$$

The unknown value of $P_{pr}$ has been calculated as equal to 0.67 kW. This result has been obtained using the experimental data through the optimization of the four linear regression coefficients of the previously cited equations. For the proposed models to estimate clad geometry and dilution, substrate preheating of 400°C results to be equivalent to an increase in the laser power of 0.67 kW (Figure 3.24). For future works, an investigation to study and confirm the correlation between $P_{pr}$ and the preheating temperature is suggested.

The same approach has been applied on clads produced on the different substrate (grey cast iron) preheated as well as before at 400°C. In Figure 3.25 the measured values of height, width, material efficiency and dilution of these clads are reported together with equations (3.4), (3.5), (3.3) and (3.10) respectively, which give the correlation between the cited properties and the processing parameters when substrate is a mild steel and it is not preheated.

As before, no visible difference between the measured values and clad height prediction can be seen, while the measured values of material efficiency and clad width are underestimated by equation (3.3) and (3.5) respectively. Since the effect of substrate preheating has been previously evaluated, the same assumption is used. Equations (3.17), (3.18) and (3.19) are used to estimate material efficiency, clad height and clad width respectively, and $P_{eff}$ is calculated using equation (3.16). The extra amount of power available by the system due to substrate preheating ($P_{pr}$), which is included in equation (3.16), is again obtained through optimization of the linear regression coefficients. This value results to be equal to 0.67 kW, thus confirming the previous result: the effect of substrate preheating of 400°C on the proposed models to estimate clad geometry is the same for the clads realized on a different substrate, and it can be represented by an increase in the laser power of 0.67 kW (Figure 3.26). Moreover, the different material used for the substrate does not have any significant effect on equations to predict clad geometry and material efficiency.
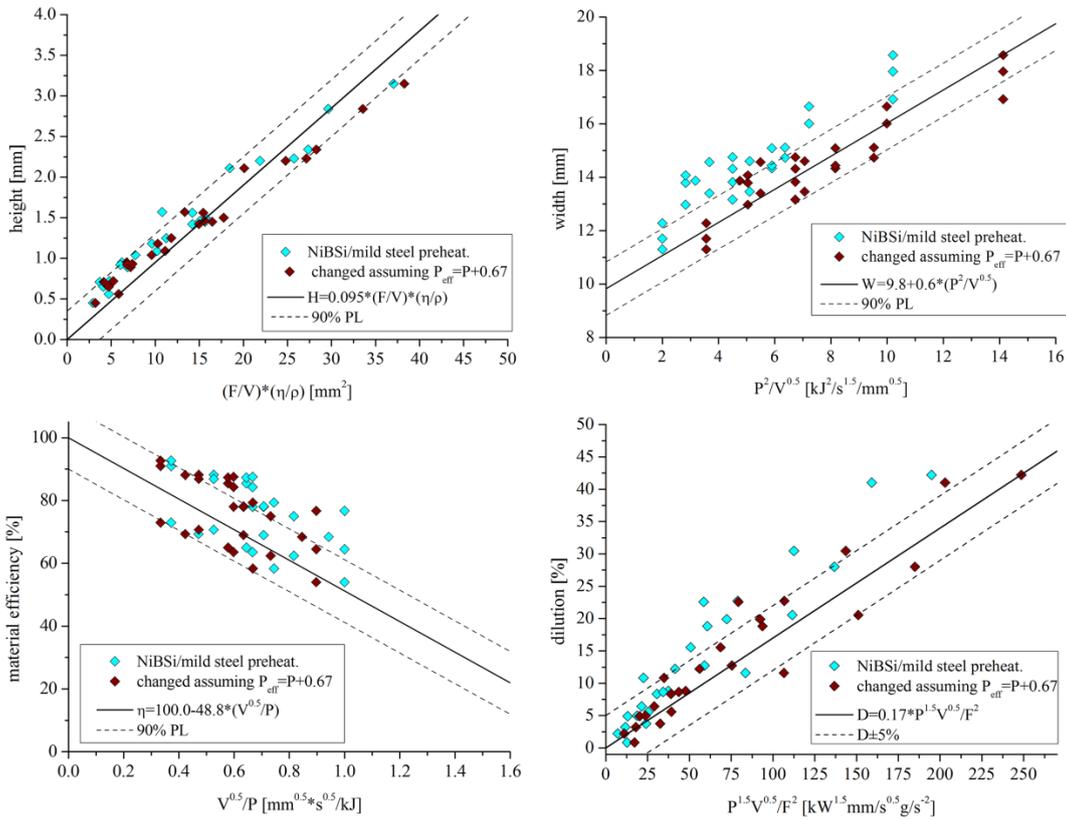
*Figure 3.24. Height, width, material efficiency and dilution of the clads produced on the preheated mild steel plotted as a function of the opportune parameter, using the real laser power P (cyan) and the modified laser power $P_{eff}$ (brown). Data points reported together with the previously obtained correlations.*
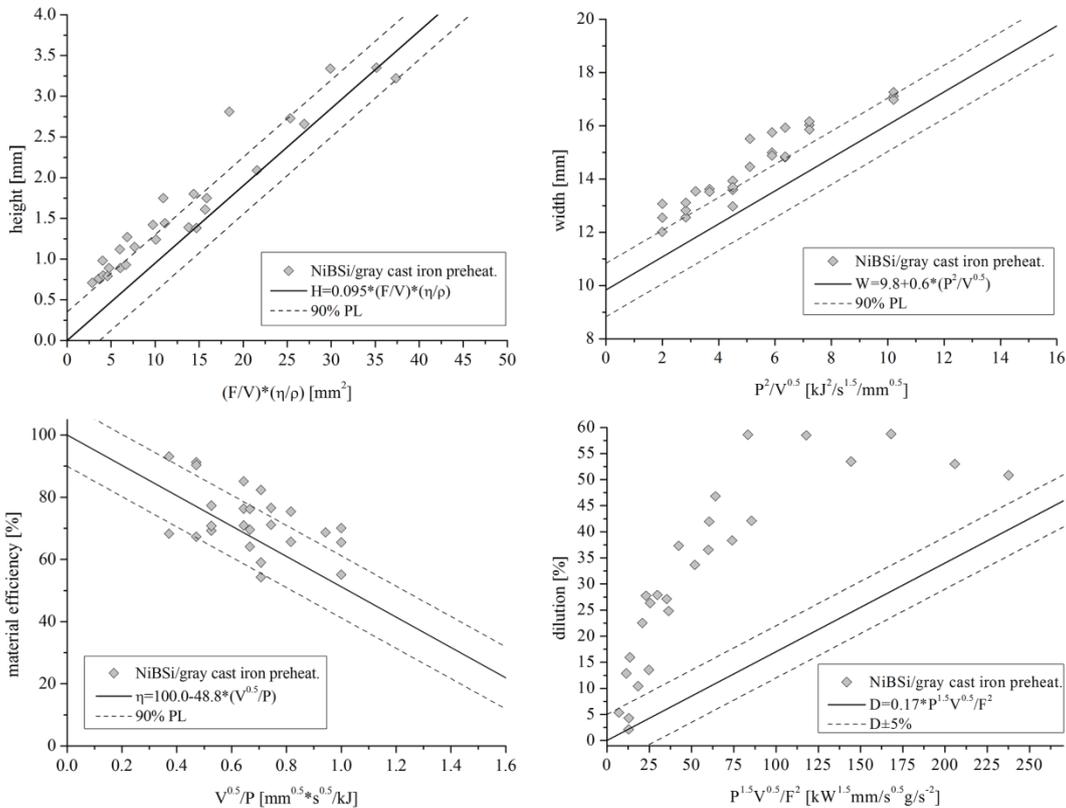


*Figure 3.25. Height, width, material efficiency and dilution of the clads produced on the preheated grey cast iron reported together with the previously obtained correlations.*
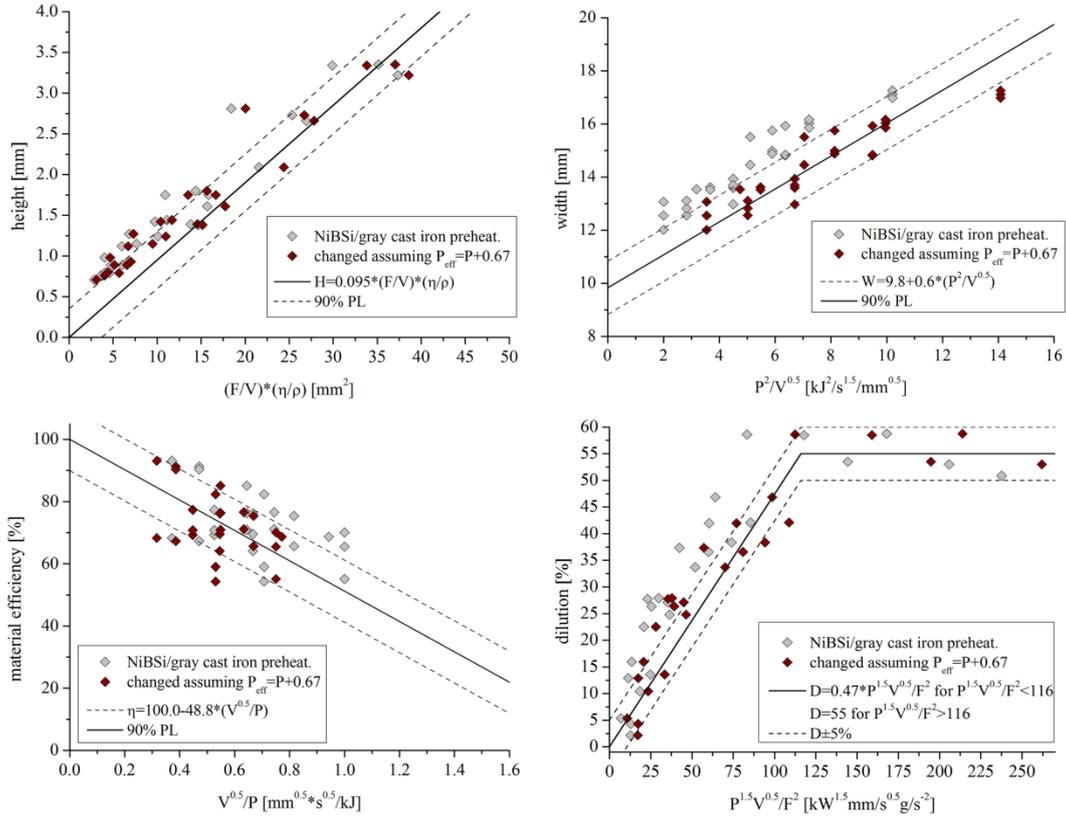
*Figure 3.26. Height, width, material efficiency and dilution of the clads produced on the preheated grey cast iron plotted as a function of the opportune parameter, using the real laser power P (light grey) and the modified laser power $P_{eff}$ (brown). Data points reported together with the previously obtained correlations.*

Dilution have been excluded from the calculation of $P_{pr}$. In fact, as it can be seen in Figure 3.26, even if substrate preheating is taken into account and the corrected equation (3.20) is used to estimate dilution, its prediction it is still not satisfactory. The measured values of dilution are always higher than the predicted ones, and they cannot be represented with a straight line. When compared to the combined parameter $P_{eff}^{1.5}V^{0.5}F^2$, dilution tends to increase linearly until the value of $D = 55\%$, where a threshold value for dilution is reached: a further increase in the parameter $P_{eff}^{1.5}V^{0.5}F^2$ does not affect dilution anymore.

The reason of the underestimation of dilution lies in the different material used as a substrate: grey cast iron, indeed, has a lower melting temperature than the mild steel; the lower melting temperature of the substrate promotes dilution since, if the same quantity of energy is given as a input and same mass and type of material is fed into the system, an higher amount of substrate is allowed to melt and dilute into the melt pool.

In order to predict dilution when a different substrate material is used, equation (3.20) has to be opportunely modified. In the first region of the graph, where dilution is linearly proportional to $P_{eff}^{1.5}V^{0.5}F^2$, a different constant of proportionality has been calculated through the optimization of the regression coefficient. This calculation has been done neglecting the measurements of the second region of the graph, where dilution has been considered as constant ($D = 55\%$). As a consequence, the equation to predict dilution in clads produced with the grey cast iron can be represented as follow

$$D_{pr} = \begin{cases} m_s \cdot \dfrac{P_{eff}^{1.5} \cdot V^{0.5}}{F^2} \ [\%], & \dfrac{P_{eff}^{1.5} \cdot V^{0.5}}{F^2} < 116 \\[2ex] 55 \ [\%], & \dfrac{P_{eff}^{1.5} \cdot V^{0.5}}{F^2} \geq 116 \end{cases} \qquad (3.21)$$

where $m_s$ is the new constant of proportionality and results to be equal to 0.47.

Graphical representation of equation (3.21) is given in Figure 3.27 together with experimental data.
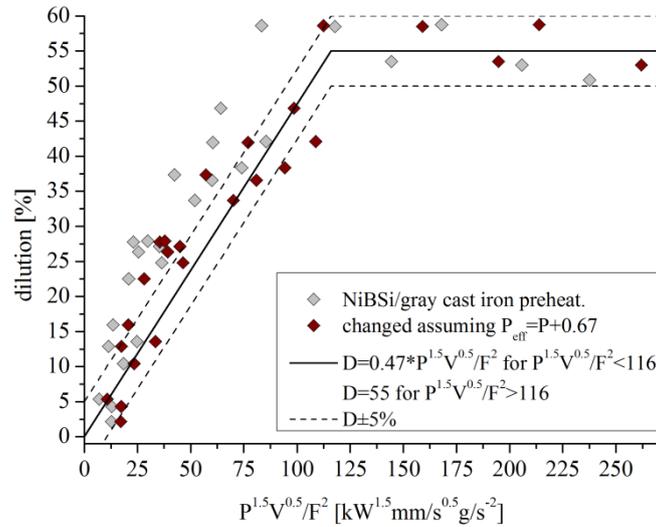


*Figure 3.27. Dilution of the clads produced on the preheated grey cast iron as a function of the parameter $P_{eff}^{1.5}V^{0.5}F^2$, plotted using the real laser power P (light grey) and the modified laser power $P_{eff}$ (brown). Data points reported together with equation (3.21).*

For clads produced with the same main processing parameters, the higher value of $m_s$ with respect to $m$ justifies the higher dilution revealed in samples produced on grey cast iron substrate.

For the particular cladding material investigated and the processing window utilized, dilution at 55% was found to be the maximum amount of dilution allowed by the process.

## 3.6 Energetic model

Laser cladding is well-known for the low energetic efficiency since a large part of the incoming laser radiation is reflected or reradiated from the cladding zone. Together with this, there are other energy losses which are more or less unavoidable or necessary to the cladding process. In Chapter 1.6 a schematic representation of the energy redistribution during laser cladding process is reported and explained. In this section, energetic balance is proposed in terms of power balance for the coatings produced with In625, 316L, Stellite1 and NiBSi. The different terms of the power balance are investigated and discussed using equations found in literature and, if necessary, modified by the author. Final considerations regarding the process efficiency and how it can be correlated to the processing conditions and the final characteristics of the clad are discussed.

### 3.6.1 Definition of the power partitioning

A brief description of the power redistribution in laser cladding process during its steady-state is given in the following lines, while a schematic representation in reported in Figure 3.28.
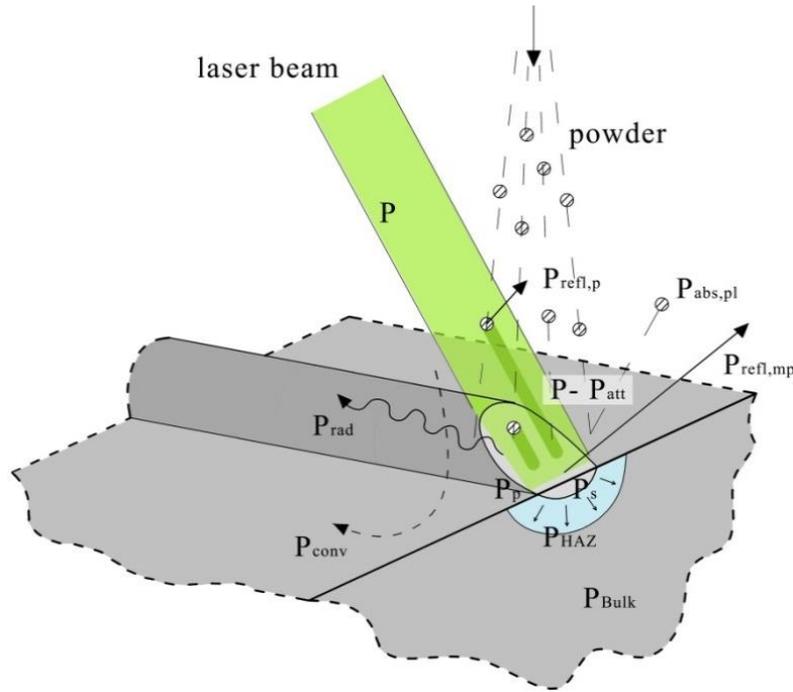
*Figure 3.28. Schematic illustration of the power redistribution for the laser cladding process during its steady-state.*

Before reaching the workpiece, the laser beam interacts with the powder particles stream: part of the radiation that hits the powder is reflected off the particles surface ($P_{refl,p}$) and part is absorbed by them ($P_{abs,p}$). Since not all the powder particles injected remain into the system, a portion of this power will contribute to the clad formation (the one related to the powder particles that remain into the melt pool, ($P_{abs,prl}$) while the other will be lost (the one related to the powder particles lost, $P_{abs,pl}$).

Consequently to this interaction, the laser beam results to be attenuated ($P_{att}$) by the powder jet, and the effective laser power available at the melt pool surface is lower ($P-P_{att}$). When the "attenuated" laser light hits the melt pool, a fraction is reflected off the melt pool surface ($P_{refl,mp}$) while the remaining part is absorbed by the cladding system ($P_{abs,mp}$) according to the absorption coefficient of the melt pool material. The laser radiation reflected off the melt pool surface is reradiated towards the powder cloud: for this reason, part of it is absorbed by the powder particles that remain into the melt pool with the same mechanism as before ($P_{abs,prl}$), and thus it is not lost [62,68,99,124,130].

However, not all the power absorbed by the workpiece can be considered as the power necessary to the clad formation ($P_C$) due to other energetic losses phenomena: part of this power is lost by conduction from the melt pool into the substrate (i.e. power to form the heat affected zone $P_{HAZ}$ and to heat up the base material $P_{bulk}$) and the remaining small part is lost by radiation and convection from the melt pool to the surroundings ($P_{rad}$ and $P_{conv}$).

Reflection and absorption phenomena of laser irradiation by the cladding system play a fundamental role in the energy balance. For this reason, the input power of the laser ($P$) can be distinguished in $P_A$ and $P_{NA}$: $P_A$ represents the part of the laser power that, at the end of the cladding process, is absorbed by the cladding system; $P_{NA}$ consequently represents the part of the power which is not absorbed and thus lost by the cladding system when the process is over

$$P = P_A + P_{NA} \qquad (3.22)$$

The part of the power which is not absorbed and thus lost by the cladding system when the process is over ($P_{NA}$) includes five quantities: the power reflected by the melt pool ($P_{refl,mp}$), the power reflected by the powder particles during injection ($P_{refl,p}$), the power absorbed by the powder particles lost in the process ($P_{abs,pl}$), the power radiated by the melt pool ($P_{rad}$) and the power lost by convection from the melt pool ($P_{conv}$) [62,99,124]

$$P_{NA} = P_{refl,mp} + P_{refl,p} + P_{abs,pl} + P_{rad} + P_{conv} \qquad (3.23)$$

On the other hand, the part of the absorbed power $P_A$ includes three quantities: the power directly absorbed by the melt pool ($P_{abs,mp}$), the power absorbed by the powder particles that remain into the melt pool ($P_{abs,prI}$) and power reflected by melt pool and subsequently absorbed by powder particles that remain into the melt pool ($P_{abs,prII}$) [99,124]

$$P_A = P_{abs,mp} + P_{abs,prI} + P_{abs,prII} \qquad (3.24)$$

The power absorbed by the cladding system is in turn redistributed between powder and substrate. In fact, $P_A$ can be seen as

$$P_A = P_p + P_s + P_{HAZ} + P_{bulk} \qquad (3.25)$$

where $P_p$ and $P_s$ are the part of the laser power used to heat up, melt and superheat the powder and the substrate respectively, $P_{HAZ}$ is the power used to form the Heat Affected Zone and $P_{bulk}$ is the power dissipated by conduction through the substrate. Since the only part of laser power which is effectively used to form the clad is given by $P_p$ and $P_s$, these two quantities together can be considered as the part of the laser power used to form the clad $P_C$.

Quantification of all these terms is now discussed.

### power attenuated ($P_{att}$)

To evaluate the amount of power attenuated, Mie's theory for the scattering of the light is used. If a powder particle cloud containing $N$ particles per unit volume is hit by a laser beam, and the powder particles are assumed to be identical to sphere in vacuum, the intensity of the proceeding beam decreases in a distance $z$ by the fraction $exp(-\gamma z)$, where $\gamma$ is the extinction coefficient [141]. Independently from the state of polarization of the incident light, the extinction coefficient is given by

$$\gamma = N \cdot \pi \cdot r^2 \cdot Q_{ext} \qquad (3.26)$$

where $r$ is the particle radius and $Q_{ext}$ is the efficiency factor of extinction.

Because of this, the ratio between the attenuated power and the incident power is described by equation

$$\frac{P_{att}}{P} = 1 - exp(N \cdot \pi \cdot r^2 \cdot Q_{ext} \cdot z) \qquad (3.27)$$

Evaluation of the terms $N$ and $z$ in equation (3.27) is quite complex due to the setup of the feeding system used. $N$ is estimated with the following equation

$$N = \frac{3 \cdot F}{\pi^2 \cdot r^3 \cdot D_{pj}{}^2 \cdot \rho \cdot V_p} \qquad (3.28)$$

where $F$ is the feeding rate, $\rho$ is the density of the cladding material and $V_p$ is the particle velocity. This equation, reported by many papers in literature [99,124,130], is simply determined geometrically assuming the laser beam and the powder stream as two intersecting cylinders.

The term $z$, through simple trigonometry, is assumed to be

$$z \cong \frac{D_{pj}}{\sin \alpha_L} \qquad (3.29)$$

Assuming that particles have constant velocity ($V_p = 2.5$ m/s) and assuming the particle radius r constant and equal to the arithmetical mean between the maximum and the minimum particle radius ($r = 50.8$ μm), equation to evaluate the attenuated power can be rewritten as

$$P_{att} = P \cdot \left[ 1 - exp \left( \frac{3 \cdot Q_{ext} \cdot F}{\pi \cdot r \cdot D_{pj} \cdot \rho \cdot V_p \cdot \sin \alpha_L} \right) \right] \qquad (3.30)$$

The efficiency factor of extinction $Q_{ext}$ is function of $n_m$-$x$ domain, where $n_m$ is the refractive index mismatch (i.e. the ratio between the refractive index of the particle and the refractive index of the medium) and $x$ is the size parameter (i.e. $x = 2\pi r/\lambda$), and might be estimated through the Tables of Mie functions [141].

However, in the present experiment the target (i.e., the liquid melt pool) is close to the powder jet with dimensions comparable to the laser beam radius. Moreover, for large particles, most of the light is diffused within a narrow cone in the forward direction. It is thus possible to assume that only the light absorbed by, or reflected onto, the particle is removed from the incident beam. In such a case, the extinction cross section should be close to the actual geometrical cross section, that is, $Q_{ext} = 1$ [99].

*power reflected by the powder particles during injection ($P_{refl,p}$)*

The power reflected by the powder particles is calculated with the following equation

$$P_{refl,p} = P_{att} \cdot \left( 1 - \beta_p \right) \qquad (3.31)$$

where $\beta_p$ is the absorbance of the powder material at the laser wavelength (808 nm) [99,124]. The use of the power attenuated in equation (3.31) is justified by the fact that $P_{att}$ is the portion of the incoming power that interacts with the powder particles. Since $\beta_p$ represents the absorbance of the powder material, $1-\beta_p$ express its reflectance. The measurement of the coefficient $\beta_p$ for the different powders is reported in Appendix 4.

*power absorbed by the powder particles lost in the process ($P_{abs,pl}$)*

The power absorbed by the powder particles lost can be quantified with equation

$$P_{abs,pl} = P_{att} \cdot \beta_p \cdot (1 - \eta) \qquad (3.32)$$

where $\eta$ is the material efficiency, expressed as a coefficient that ranges between 0 and 1 [99,124]. The term $P_{att} \cdot \beta_p$ represents the power absorbed by all the powder particles, while with the term $1 - \eta$ limits the calculation only to the powder lost in the process.

### *power radiated by the melt pool ($P_{rad}$)*

The power radiated from the melt pool can be estimated using the temperature of the melt pool, its surface area and its emissivity. Assuming the emissivity of the liquid metal as equal to 1 for simplicity, the maximum possible radiation can be calculated with the formula

$$P_{rad} = \sigma_{SB} \cdot T_{mp}^{\;4} \cdot A_{mp} \qquad (3.33)$$

where $\sigma_{SB}$ is the Stefan-Boltzmann constant ($5.7 \cdot 10^{-8}$ W/m$^2$K$^4$), $T_{mp}$ is the average temperature reached by the melt pool and $A_{mp}$ is the area of the melt pool [62]. The temperature of the melt pool, which is the only parameter unknown, has been estimated is Appendix 6.

### *power lost by convection from the melt pool ($P_{conv}$)*

Convection occurs because the hot melt pool is exposed to the cold streams of the carrier and the shielding gas. The rate of convective cooling of a hot body exposed to a cooler gas is given by equation

$$Q_{conv} = h \cdot S \cdot \left(T_{mp} - T_{cg}\right) \qquad (3.34)$$

where $h$ is the heat transfer coefficient, $S$ is the surface area of the hot body and $T_{cg}$ is the temperature of the cooling gas [62]. Since evaluation of the heat transfer coefficient from a standard text (100 W/m$^2$K) [142] leads to a limited rate of convective cooling and consequently to a very low value of powder lost by convection from the melt pool ($P_{conv} < 0.01P$), the convection phenomena can be neglected from the power balance.

### *power reflected by the melt pool ($P_{refl,mp}$)*

The power lost by melt pool reflection is estimated with equation

$$P_{refl,mp} = (P - P_{att} - P_{rad} - P_{conv}) \cdot (1 - \beta_S) - P_{abs,prII} \qquad (3.35)$$

where $\beta_s$ is the absorptivity, or absorption coefficient, of the liquid metal material when irradiated by a laser light and $P_{abs,prII}$ is the fraction of power reradiated from the melt pool and subsequently absorbed by the powder particles that remain into the melt pool [99]. This value has to be subtracted in the calculation of $P_{refl,mp}$ because, even if initially reflected by the melt pool, this radiation is absorbed by the system and thus not lost. The equation to calculate $P_{abs,prII}$ is presented in the next point. The term $1 - \beta_s$ in equation (3.35) represents the reflectivity of the metal melt pool. The calculation of the coefficients $\beta_s$ for the cladding materials treated is reported in Appendix 3.

***power absorbed by the powder particles that remain into the melt pool ($P_{abs,prI}$ and $P_{abs,prII}$)***

The power absorbed by the powder particles that remain into the melt pool can be distinguished in two components: the part which is absorbed directly from the input laser radiation ($P_{abs,prI}$) and the part which is absorbed from the radiation reradiated from the melt pool, as explained before ($P_{abs,prII}$). These two components can be estimated [99] through the following equations

$$P_{abs,prI} = P_{att} \cdot \eta \cdot \beta_P \qquad (3.36)$$

$$P_{abs,prII} = (P - P_{att} - P_{rad} - P_{conv}) \cdot \eta \cdot \beta_P \cdot \frac{P_{att}}{P} \cdot (1 - \beta_S) \qquad (3.37)$$

***power absorbed by the melt pool ($P_{abs,mp}$)***

As shown for the calculation of $P_{refl,mp}$, the power absorbed by the melt pool can be calculated [62,99,124] through the absorption coefficient $\beta_s$ using equation

$$P_{abs,mp} = (P - P_{att} - P_{rad} - P_{conv}) \cdot \beta_S \qquad (3.38)$$

Using equation (3.38) the global power absorbed by the cladding system ($P_A$) can be calculated. This power is redistributed as explained in equation (3.25). The terms of this equation can be estimated as follows.

***power used to heat up, melt and superheat the powders ($P_p$)***

With the assumptions of constant cross-sectional area in the clad length and negligible influence of the solid-state phase transformations in the material of the clad during laser irradiation, the power used to heat up, melt and superheat the powders is calculated with equation

$$P_p = A_N \cdot V \cdot \rho_p \cdot \left[ c_{p,p}(T) \cdot \left( T_{mp} - T_r \right) + \Delta H_{m,p} \right] \qquad (3.39)$$

where $A_N$ is the emerging cross section of the clad, $V$ is the scan speed, $\rho_p$ is the density of the cladding material, $c_{p,p}$ is the heat capacity of the clad material, which is function of the temperature, $T_{mp}$ is the average temperature reached by the melt pool, $T_r$ is the room temperature and $\Delta H_{m,p}$ is the enthalpy of melting of the cladding material [62]. The heat capacity of the different materials has been obtained as reported in Appendix 7, while the temperature of the melt pool has been estimated as shown in Appendix 6. For the enthalpy of melting of the different materials, values found in literature have been used [143-146]. These values are reported in Table 3.4.

*Table 3.4. Enthalpy of melting of the four powder materials and the substrate material.*

|  | $\Delta H_m$ [J/g] |
| --- | --- |
| NiBSi | 300 |
| 316L | 280 |
| In625 | 275 |
| Stellite1 | 310 |
| mild steel | 272 |

***power used to heat up, melt and superheat the substrate ($P_s$)***

The power used to heat up, melt and superheat the substrate is defined in a similar way. With the same assumption as before (constant cross-sectional area and negligible influence of the solid-state phase transformations in the material of the substrate), $P_s$ is estimated with equation

$$P_S = A_D \cdot V \cdot \rho_s \cdot \left[ c_{p,s}(T) \cdot \left( T_{mp} - T_r \right) + \Delta H_{m,s} \right] \qquad (3.40)$$

where $A_D$ is the submerged cross-sectional area of the clad, $\rho_s$ is the density of the substrate material, $c_{p,s}$ is the heat capacity of the substrate material, which is function of the temperature and $\Delta H_{m,s}$ is the enthalpy of melting of the substrate material, which has been found in literature (272 J/g). The heat capacity of the substrate material has been estimate in Appendix 7.

***power used to for the Heat Affected Zone ($P_{HAZ}$)***

The power utilized for the formation of the Heat Affected Zone is quantified with equation

$$P_{HAZ} = A_{HAZ} \cdot V \cdot \rho_s \cdot c_{p,s}(T) \cdot (T_{HAZ} - T_r) \qquad (3.41)$$

where $A_{HAZ}$ is the cross-sectional area of the Heat Affected Zone, measured with Image Analysis and $T_{HAZ}$ is temperature reached by the Heat Affected Zone. Again, the contribution of the alpha-to-gamma transformation to the value of $P_{HAZ}$ is neglected, and the cross-sectional area of the Heat Affected Zone is considered constant in the clad length. The Heat Affected Zone is assumed to reach, independently from the processing conditions, an average temperature between A$_3$ ($T_{A3,s} = 871°C$) [146] and the melting temperature ($T_{m,s} = 1515°C$) [146] of the mild steel used

$$T_{HAZ} = \frac{T_{A3,s} + T_{m,s}}{2} \qquad (3.42)$$

***power dissipated by conduction through the substrate ($P_{bulk}$)***

The remaining portion of power is dissipated by conduction through the substrate, and its only contribution is to heat up the substrate. This term can be calculated once all the other contributions are determined with the formula

$$P_{bulk} = P_A - P_p - P_S - P_{HAZ} \qquad (3.43)$$

## 3.6.2 Calculations of the power partitioning

*Effect of the cladding material*

The estimation of the energetic redistribution during the laser cladding process is reported in Figure 3.29 in terms of approximate percentages, calculated by averaging the results obtained in different processing conditions and with different cladding materials.
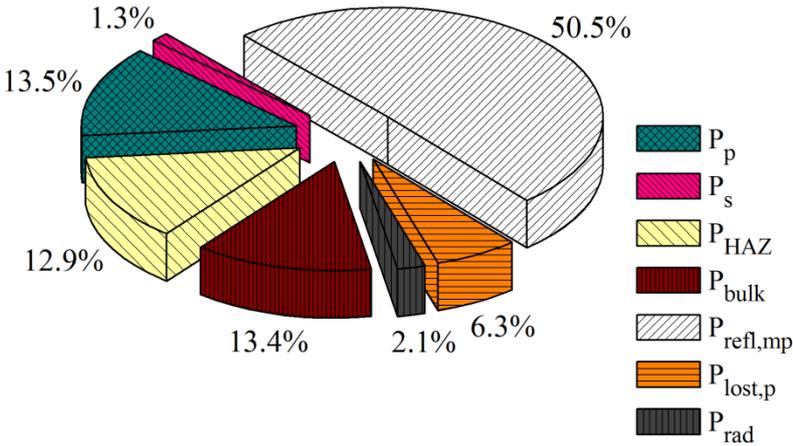


*Figure 3.29. Average energetic redistribution during the laser cladding process.*

The same calculation for the four distinguished cladding materials is represented in Figure 3.30.
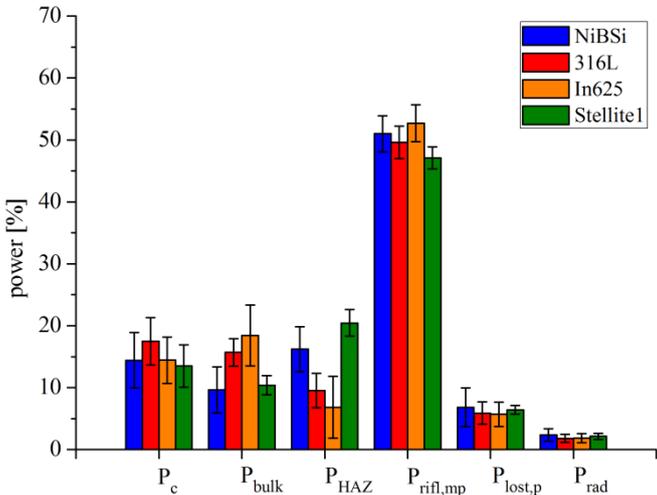


*Figure 3.30. Average energetic redistribution during the laser cladding process for the different materials.*

The major mechanism of energy loss is the reflection of the laser light from the molten pool surface. Irrespective of the cladding material, almost the half of the input energy ($50 \pm 3\%$) is lost due to this phenomenon. The reflectivity of the liquid metal, which is however limited by the low wavelength of the high power diode laser, is principally influenced by the melt pool surface condition, and in particular by surface oxidation during cladding: since the melt is produced in a protective atmosphere

guaranteed by argon injection, surface oxidation is prevented and interaction occurs directly between the laser light and the liquid metal, that is highly reflective.

The power lost due to the powder particles injection ($P_{lost,p}$), that includes both the part reflected off the powders surface and the part absorbed by the powders lost, corresponds to the $6 \pm 2\%$ of the input power. In these phenomena, the effect of the cladding material is mainly determined by the powder particle absorption coefficient $\beta_p$ and by the powder particles size. Since powder size is the same and no big differences are found between the estimated values of $\beta_p$, as reported in Appendix 4, no significant variations of this quantity is highlighted for the four different cladding materials (Figure 3.30).

The power losses due to radiation and convection from the melt pool are low: the first one corresponds to the $2 \pm 1\%$ of the input power, while the second one has been neglected since it is lower than 1% of the laser power $P$.

Even if results of the various batches are obviously influenced by the ranges of the processing parameters, by their combination and by the number of experiments performed, some considerations about the effect of the cladding material on the various quantities can still be done.

Of the power absorbed by the cladding system ($P_c + P_{HAZ} + P_{bulk} = 41\%$) more than half ($\approx 66\%$) is wasted to heat up the substrate and to form the Heat Affected Zone, while only $15 \pm 4\%$ of the input power is used for the clad formation. This average percentage is almost the same for all the cladding materials investigated; however, a slightly higher value is observed in the batch produced with the 316L stainless steel. This small difference is principally caused by the higher temperature reached by the melt pool during cladding, which requires a higher amount of energy and consequently to a higher average value of $P_c$.

The average value of the percentage of input power utilized to form the Heat Affected Zone is equal to the $13 \pm 5\%$. Also in this case, the effect of the molten pool temperature is visible when the various batches produced with different cladding materials are considered separately: even if the value of $P_{HAZ}$ is influenced by dilution and so by the processing parameters, the lowest average value of $P_{HAZ}/P$ is found for the clads produced with the NiBSi alloy, where the average melt pool temperature is the lowest. On the other hand, the average value of $P_{HAZ}/P$ is the highest for the clads produced with the 316L stainless steel, where the average melt pool temperature is the highest. The melt pool temperature affects the amount of energy conducted to the substrate and, as a consequence, the volume of the Heat Affected Zone.

Since the values of $P_{bulk}$ is obtained once all the other quantities of the power balance are known, any possible effect of the cladding material on $P_{bulk}$ is not considered or discussed. However, it is interesting to notice that the power lost to heat up the rest of the bulk is the $13 \pm 6\%$ of the input power, corresponding to about the 32% of the laser power absorbed by the cladding system. Due to the waste of high quality laser energy, not only the energetic efficiency but also the economic efficiency of the process result decreased. As suggested by [62], a possible solution to improve the economic efficiency of the cladding process is the substrate preheating treatment involving a cheaper energy source, such as flame, furnace, plasma or induction techniques.

*Effect of the processing parameters and angle of incidence*

In Figure 3.31, the percentage of the laser power that is absorbed by the cladding system ($P_A$) with respect to the input power is plotted as a function of the angle of incidence.
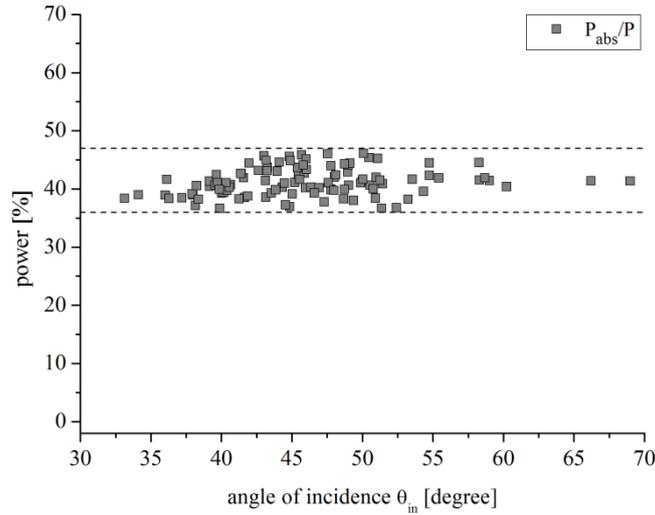
*Figure 3.31. $P_{abs}/P$ percentage as a function of the angle of incidence.*

As said before, the average value of the percentage of power absorbed by the cladding system is equal to 41%. As it can be seen in Figure 3.31, no significative variations of this value are highlighted: irrespective of the angle of incidence (i.e. on the processing parameters), the percentage of power (or energy) available by the cladding system remains the same. This condition is principally due to the polarization state of the laser source and to the similar values of $n$ and $k$ (refraction index and extinction coefficient respectively) of the cladding materials utilized, as extensively explained in Appendix 3.

In Figure 3.32, the percentage of the laser power used to heat up, melt and superheat the powder ($P_p$) with respect to the input power is plotted as a function of the angle of incidence.
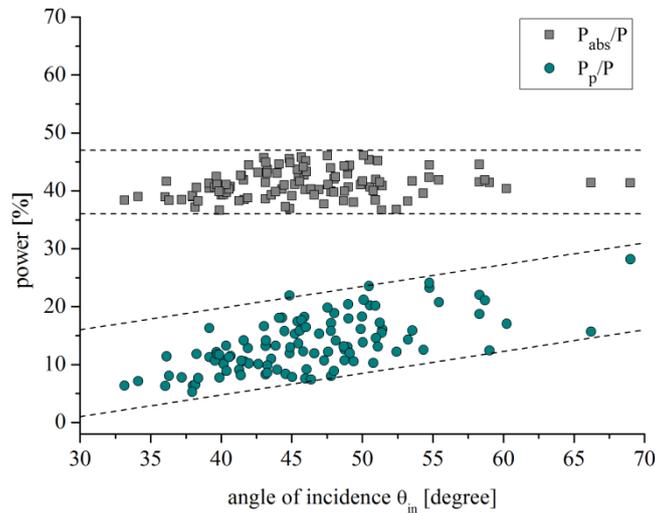


*Figure 3.32. $P_p/P$ and $P_{abs}/P$ percentages as a function of the angle of incidence.*

On increasing the angle of incidence, the percent of energy used for the powder particles increases since a higher amount of material is involved into the process. In fact, the angle of incidence is proportional to the clad height according to equation (A.11). As a consequence, the percentage of energy required by the cladding system results to be higher. This is also visible in Figure 3.33, where the correlation between the values of $P_p/P$ [%] and the feeding rate is reported.
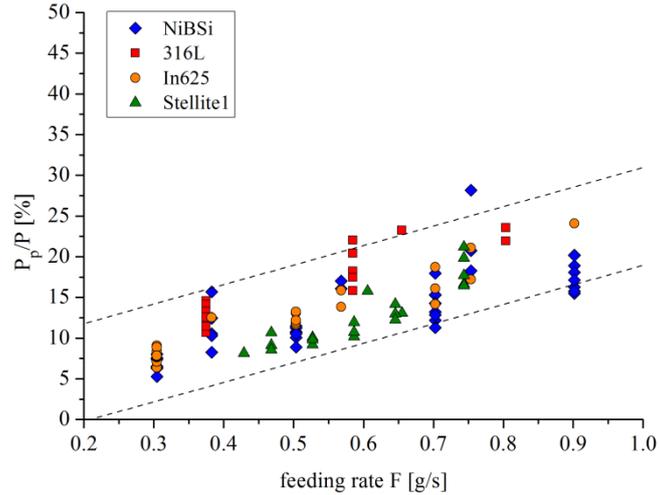
*Figure 3.33. $P_p/P$ percentage as a function of the feeding rate.*

In Figure 3.34, the percentage of the laser power used to heat up, melt and superheat the substrate ($P_s$) with respect to the input power is plotted as a function of the angle of incidence.
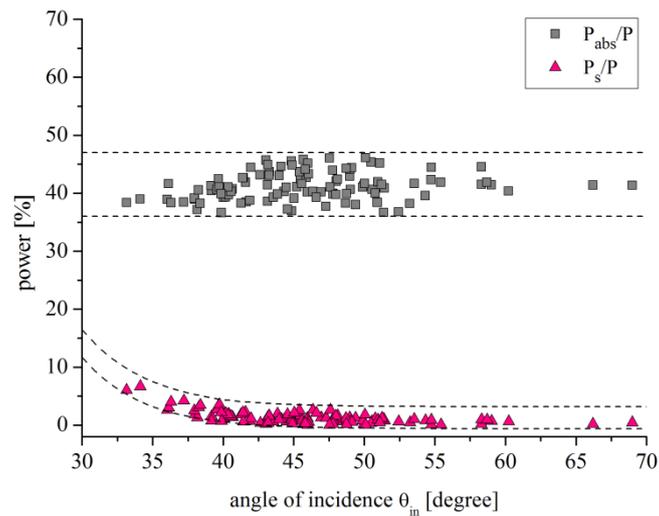


*Figure 3.34. $P_s/P$ and $P_{abs}/P$ percentages as a function of the angle of incidence.*

On increasing the angle of incidence, the percent of energy used for the substrate decreases. $P_s$, which is calculated with equation (3.40), is proportional to the submerged part of the cross-sectional area $A_D$, and represents the percent of energy utilized to dilute the substrate. Together with $P_p$, which is proportional to $A_N$, $P_s$ can be used to describe dilution.

Dilution $D$ has been defined as the ratio between the submerged part of the cross-sectional area $A_D$ and the total cross-sectional area ($A$), that is equal to $A_D+A_N$. Since the value of $A_D$ is much lower than $A_N$, dilution can be approximated as shown in equation

$$D = \frac{A_D}{A_D + A_N} \approx \frac{A_D}{A_N} \qquad (3.44)$$

If the differences in the specific heat and material density between substrate and powder are neglected, equation (3.44) becomes

$$D = \frac{A_D}{A_D + A_N} \approx \frac{A_D}{A_N} \approx \frac{P_s}{P_p} \qquad (3.45)$$

Clad dilution is correlated to the ratio between the power used to heat up, melt and superheat the substrate and the powder (Figure 3.35).
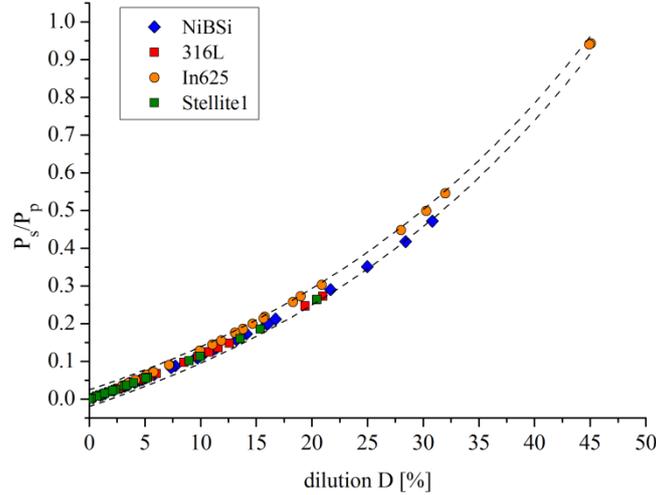


*Figure 3.35. Correlation between the $P_s/P_p$ ratio and the dilution D of the clad.*

Due to the evident correlation between the values of $P_p$ and $P_s$ and the angle of incidence (Figure 3.32 and Figure 3.34), the ratio $P_s/P_p$ and dilution have been plotted as a function of the angle of incidence in Figure 3.36.
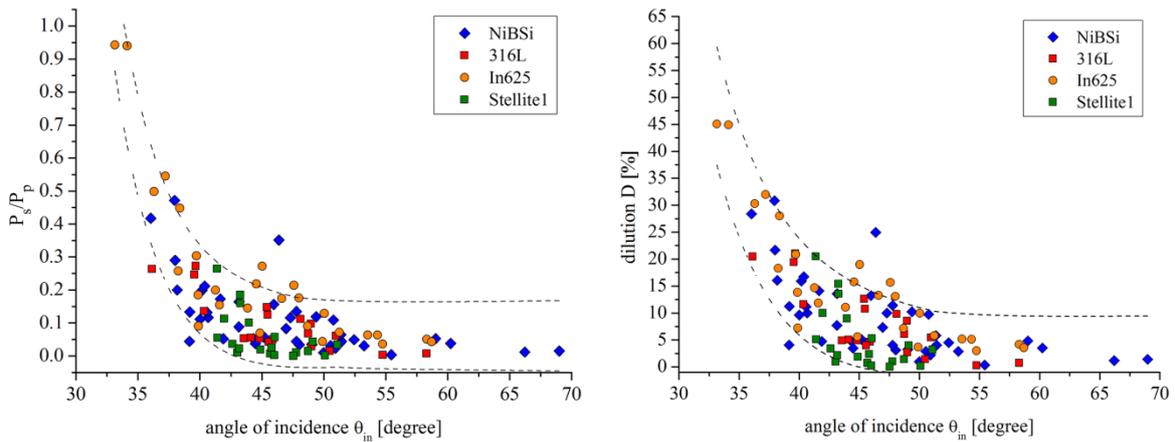


*Figure 3.36. Correlations between the $P_s/P_p$ ratio and angle of incidence (left) and between dilution and angle of incidence (right).*

For high values of the angle of incidence, clad dilution is limited and the ratio $P_s/P_p$ tends to be low. On decreasing the angle of incidence down to the minimum value accepted ($\theta_{in} = \alpha_L = 28°$), the ratio $P_s/P_p$ and dilution increase with the typical behaviour shown in Figure 3.36.

As the value of $P_s$ is much lower than the value of $P_p$, the total power used to form the clad ($P_c = P_p + P_p$) is basically dictated by $P_p$: on increasing the angle of incidence, the percentage of power used to form the clad with respect to the input power increases (Figure 3.37).
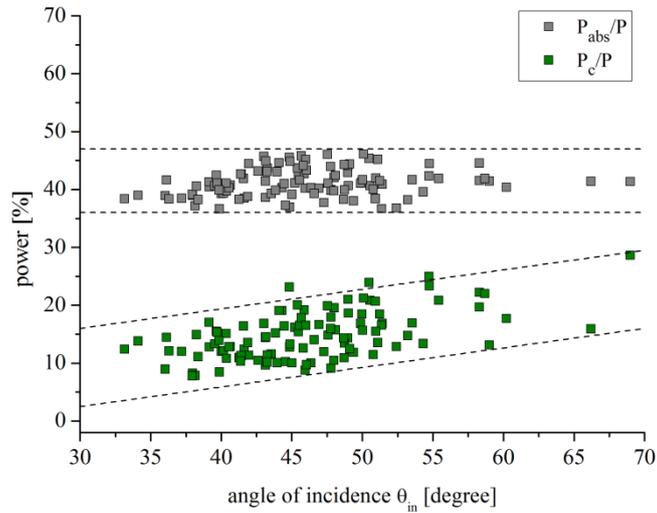


*Figure 3.37. $P_c/P$ and $P_{abs}/P$ percentages as a function of the angle of incidence.*

The angle of incidence is a useful parameter to describe the energy partitioning of the laser cladding process. By varying the angle of incidence, the energy absorbed by the cladding system does not change. However, the energetic balance of the process is drastically altered: for low $\theta_{in}$, thinner clads with an extremely high amount of dilution are generated, and most of the absorbed energy is lost by conduction through the substrate. This is further confirmed by the correlation between the value of $P_{HAZ}/P$ [%] and $\theta_{in}$: for low values of the incidence's angle, the percent of power utilized to form the HAZ with respect to the input power is high, and decreases on increasing $\theta_{in}$ (Figure 3.38).
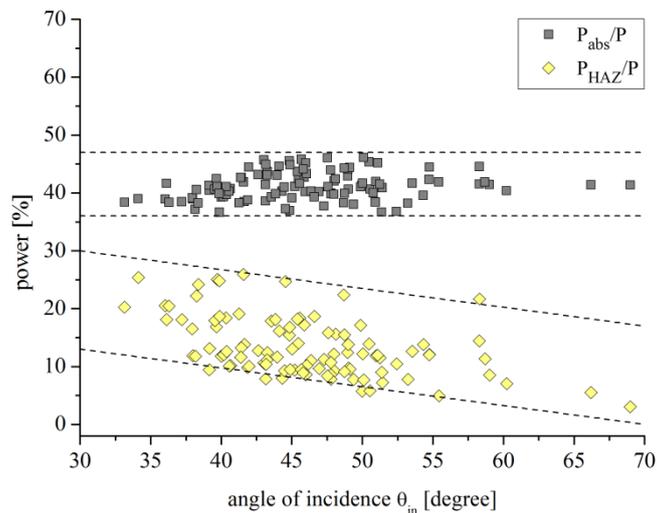


*Figure 3.38. $P_{HAZ}/P$ and $P_{abs}/P$ percentages as a function of the angle of incidence.*

On increasing $\theta_{in}$, thicker clads are produced. Since in thicker clads the amount of material to protect the substrate is higher, dilution increases. Furthermore, on increasing $\theta_{in}$ the energetic efficiency of the process increases due to the increment of $P_c/P$ and the decrement of $P_{HAZ}/P$.

Regarding the energy used to heat up the rest of the bulk, it can be said that no clear correlations are found between the values of $P_{bulk}/P$ [%] and the angle of incidence: the energy conducted to the substrate seems to be dissipated through the substrate unconditionally from the incidence angle (Figure 3.39).
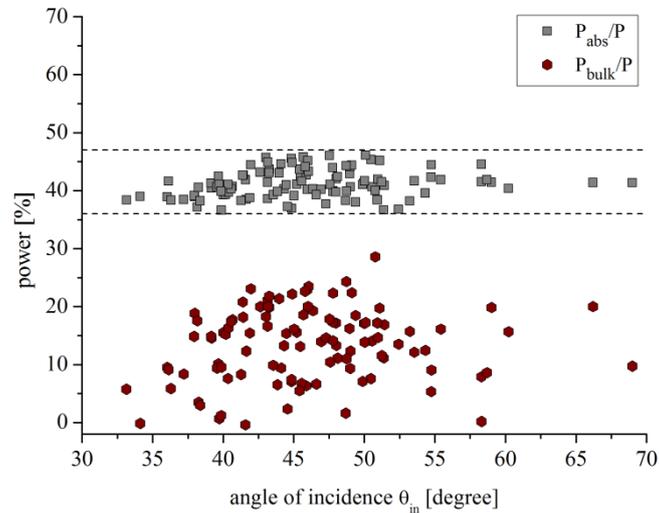


*Figure 3.39. $P_{bulk}/P$ and $P_{abs}/P$ percentages as a function of the angle of incidence.*

It has to be said, however, that the value of $P_{bulk}$ is calculated in reverse once all the other quantities are known, and for this reason it includes all the approximations made in the energetic balance. For a more precise evaluation of this quantity, substrate temperature measurements during laser cladding must be performed.

## 3.7   Coatings characterization

In this section the final characteristics of the coatings have been focused. In particular, the effect on clad properties of important parameters such us substrate dilution and, in the case of MMC, carbide dissolution, is considered and discussed.

As said before, in laser cladding process a minimum level of dilution is necessary to ensure a good bonding with the substrate, but an excessive contamination of the clad by the substrate material may influence the properties of the coating negatively. Dilution is generally kept between 2 and 5%, but a real upper limit can be fixed only when the influence of dilution on the coating properties is known. For this reason, a study of the effect of dilution on some selected properties of clads produced with Stellite1, In625 and NiBSi alloy is proposed in the following three chapters.

Together with dilution, when hard reinforcement particles are added to the cladding material to produce MMC coatings, also dissolution of these particles is something that may influence, not necessarily in a detrimental way, coating properties. In the last chapter the influence of different processing condition on the dissolution of tungsten carbides in two Co-based alloy, and its effect on final properties of the clad is presented.

### 3.7.1 Stellite1

Stellite1 powder has been cladded onto a mild steel substrate in different processing condition to obtain different values of dilution.

In Figure 3.40 three micrographs representative of the microstructure of samples with low (*Fe < 5%*), intermediate (*5% < Fe < 15%*) and high dilution (*Fe > 15%*) are reported. Since the initial iron content of the Stellite1 is low (0.93%), the value of *Fe* does not differ so much from the value of *D*.
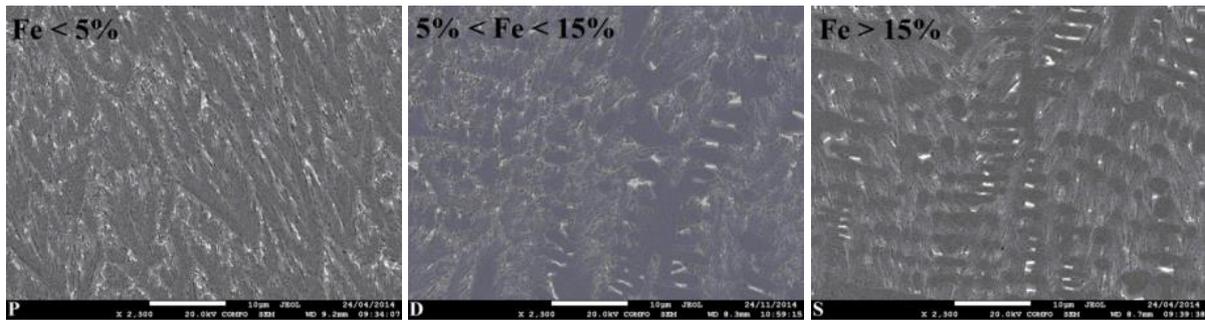


*Figure 3.40. Micrographs of samples with dilution lower than 5% (left), between 5% and 15% (center), and higher than 15% (right).*

Dilution influences clad microstructure. Solidification structure of the sample with low dilution (*Fe < 5%*) presents a pro-eutectic constituent having cellular features with small eutectic cells. In the highly diluted sample (*Fe > 15%*) the pro-eutectic constituent has a dendritic structure with the eutectic constituent segregated in the interdendritic spacing. In samples where dilution is between 5% and 15%, an intermediate solidification structure is present showing both the cellular and the dendritic features.

Solidification structures also differ in the total amount of eutectic constituent, which is higher in the clads with low dilution. This eutectic constituent was analysed by EDXS (Table 3.5) and SEM (Figure 3.41); it is made of the Co solid solution matrix and two different types of carbide: the white one (Figure 3.41,a) and the grey one (Figure 3.41,b). Considering the tungsten content and the W/C ratio, even if from semi-quantitative data it may be concluded that the white carbides are $M_6C$ and the grey carbides are $M_{23}C_6$.

*Table 3.5. EDXS analysis of the white (a) and the grey (b) carbides of samples with dilution lower than 5% and higher than 15% respectively.*

| sample | carbide type | C [%] | Cr [%] | Fe [%] | Co [%] | W [%] |
|--------|--------------|-------|--------|--------|--------|-------|
| Fe < 5% | white (a) | 4.7 | 22.9 | 0.6 | 33.8 | 38.0 |
|  | grey (b) | 1.7 | 24.5 | 1.0 | 60.6 | 12.2 |
| Fe < 15% | white (a) | 3.9 | 18.4 | 10.6 | 30.2 | 36.9 |
|  | grey (b) | 2.3 | 18.6 | 16.6 | 47.6 | 14.9 |
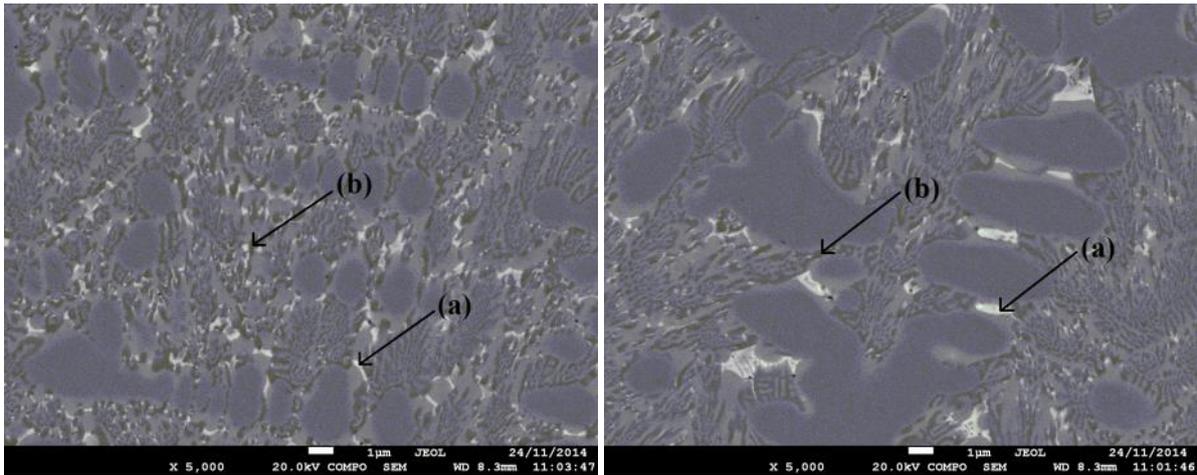
*Figure 3.41. Stellite microstructures showing the white (a) and the grey (b) carbides.*

Hardness of the clads is reported in Figure 3.42 as a function of their average iron content.
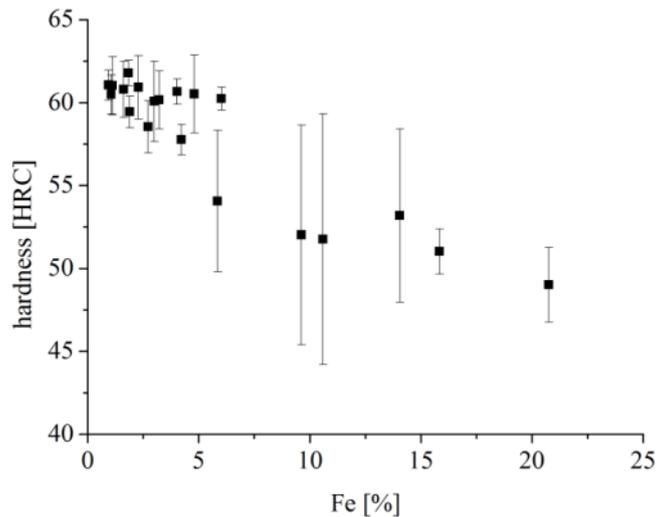


*Figure 3.42. Rockell-C hardness as a function of dilution.*

Hardness decreases with the increase in dilution: when dilution is low, it is about $61 \pm 1$ HRC, which corresponds to the expected hardness of a Stellite1 alloy coating produced with laser. When the average iron content of the coating is almost 20%, hardness drops down to $49 \pm 2$ HRC. Hardness is also highly scattered in the samples where dilution is in the range between 5% and 15%. To better understand this behaviour, microhardness measurements have been carried out. Results are reported in Figure 3.43.

Microhardness is strongly dependent on the clad microstructure: it is the higher in the less diluted samples, which show the cellular solidification structure (for instance $824 \pm 24$ $HV_{0.1}$ where *Fe = 0.9%*), and the lower in the most diluted specimen having the almost fully dendritic microstructure (for instance $675 \pm 3$ $HV_{0.1}$ where *Fe = 20.8%*). In samples where dilution is between 5% and 15%, which show both the cellular and the dendritic solidification structures, microhardness is different: in the cellular regions microhardness is higher ($795 \pm 22$ $HV_{0.1}$ where *Fe = 10.6%*) than in the dendritic ones ($698 \pm 40$ $HV_{0.1}$). This explains the broad scattering bands of the hardness values for the samples in this dilution range.

72
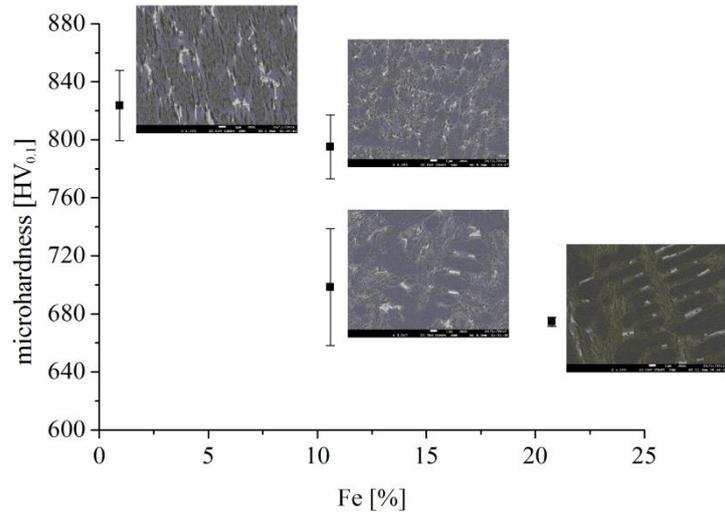
*Figure 3.43. Vickers 0.1 microhardness as a function of dilution with respective microstructure.*

Dilution finally influence phase distribution of the solid solution matrix. As it can be seen in Figure 3.44, on increasing dilution, the α-fcc phase of the coating tends to increase at the expense of the ε-hcp phase. This may be attributed to the alpha stabilizing effect of both carbon and iron in cobalt alloys [147].
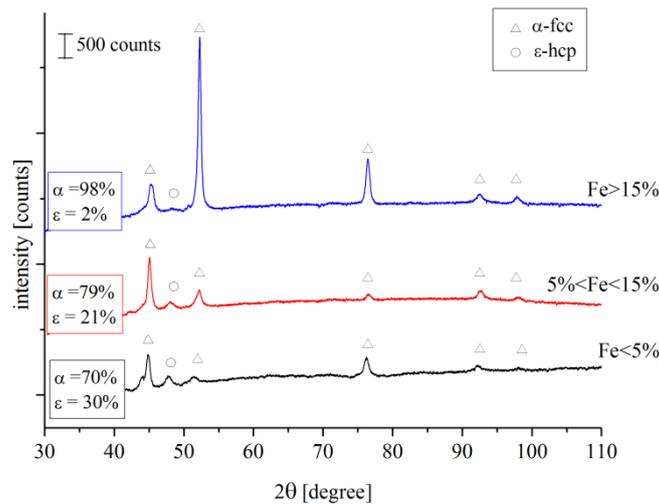


*Figure 3.44. Distribution of α-fcc and ε-hcp phases for samples with dilution lower than 5% (black), between 5% and 15% (red), and higher than 15% (blue) respectively.*

Dilution influences the solidification structure and hardness of the clad significantly. It's well known that solidification structure evolves from cellular to dendritic on decreasing the *G/R* ratio, where *G* and *R* are the temperature gradient perpendicular to the solid/liquid interface and the cooling rate, respectively. Huang et al. [148] propose a correlation between *G/R* and the laser scan speed (*V*) and power (*P*)

$$\frac{G}{R} = \frac{2 \cdot \pi \cdot K \cdot (T - T_0)^2}{\beta_G \cdot P \cdot V \cdot \cos\theta} \qquad (3.46)$$

where $T$ is the temperature of the alloy melt pool, $T_0$ is the preheated temperature of the substrate, $\beta_G$ is the laser absorption coefficient and $K$ is the thermal conductivity of the material and $\theta$ is the angle between the scan speed vector and the normal to the solid-liquid interface.

Dilution, as stated in Chapter 3.2, is promoted by higher laser power and higher scan speed. For this reason, dilution is representative of the variation of these two parameters: an increased clad dilution is generated with higher laser power and higher scan speed, which are also the cause of a lower $G/R$ ratio. As a consequence, evolution from cellular to dendritic solidification structure is favoured.

On increasing dilution, moreover, the iron content of liquid stellite increases and the carbon content decreases; consequently the chemical composition moves away from the eutectic composition, thus resulting in an increased extension of the solidification range. As well known, on increasing such a solidification range, solidification structure tends to evolve from cellular to dendritic.

Due to the modification of the chemical composition of the liquid stellite, a lower amount of eutectic constituent is formed during solidification of the more diluted clads. Consequently, being carbides localized in the eutectic constituent, microhardness and hardness decrease.

Figure 3.40 clearly shows that carbides are larger and more spaced in the most diluted clad, thus further contributing to the reduced hardness. Size and distribution of carbides depend mostly on cooling rate. Cooling rate is mostly determined by the product of $G$ and $R$ [149], and is thus governed by the ratio between $P$ and $V$ through equation

$$\frac{dT}{dt} = \frac{2 \cdot \pi \cdot K \cdot V \cdot \cos\theta \cdot (T - T_0)^2}{\beta_G \cdot P} \qquad (3.47)$$

In the present work, the larger and more spaced carbides are observed in the most diluted clads, that are produced with the highest power, the lowest powder feed and, even if with a lower influence, the highest scan speed. Again, it seems that the solidification microstructure is not linked to the thermal field assisting solidification. Any correlation between carbide size and the size of the proeutectic constituent cannot be made, due to the difficulty of comparing the size of cellular and dendritic structures.


## 3.7.2   Inconel 625

Inconel 625 powder has been cladded onto a the mild steel substrate in different processing condition to obtain different values of dilution, and a preliminary study of the effect of dilution on material properties (microstructure and microhardness) and on the thermal oxidation behaviour of these clads has been conducted.

The microstructures of the clads exhibiting 3.9 and 45.0% of dilution respectively are reported in Figure 3.45. In order to investigate the only effect of dilution on microstructure, these clads has been produced using the same laser power and scan speed and varying the feeding rate.

The effect of dilution on the microstructure of the clad is evident: the microstructure of the clad with low dilution (Figure 3.45,a) is characterized by a columnar dendritic microstructure resulting from the typical rapid solidification of the laser cladding technique, with an interdendritic region occupied by a fine distribution of blocky-shaped precipitates.
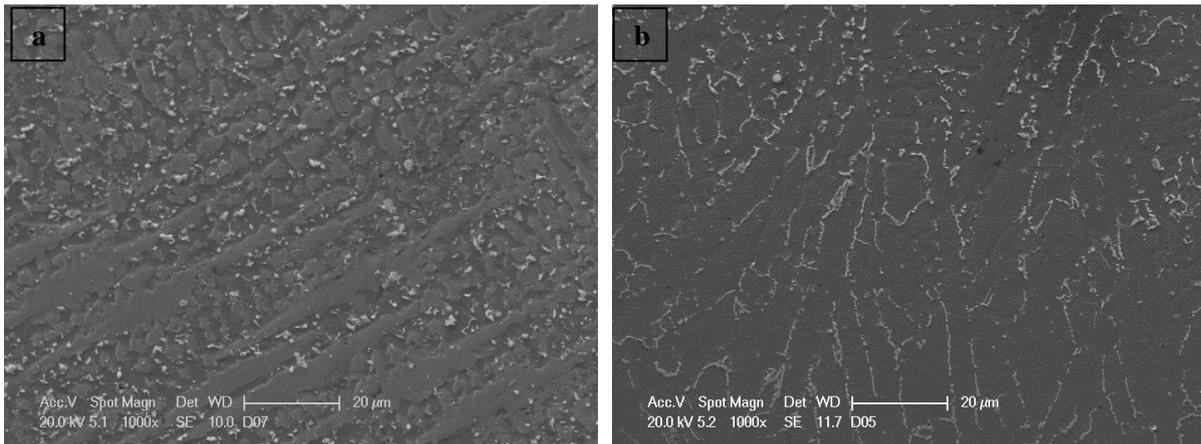
*Figure 3.45. Microstructures of the clads with different dilution: a) 3.9% and b) 45.0%.*

On the other hand, the microstructure of the clad with high dilution (Figure 3.45,b) presents the same columnar dendritic microstructure but shows an evolution in the interdendritic region, where precipitates are less well-distributed and exhibit irregular shape and lamellar eutectic-type morphology.

Higher magnification micrographs of the two microstructure are reported in Figure 3.46 and Figure 3.47 together with the EDXS analysis of the precipitates.



EDXS spot analysis
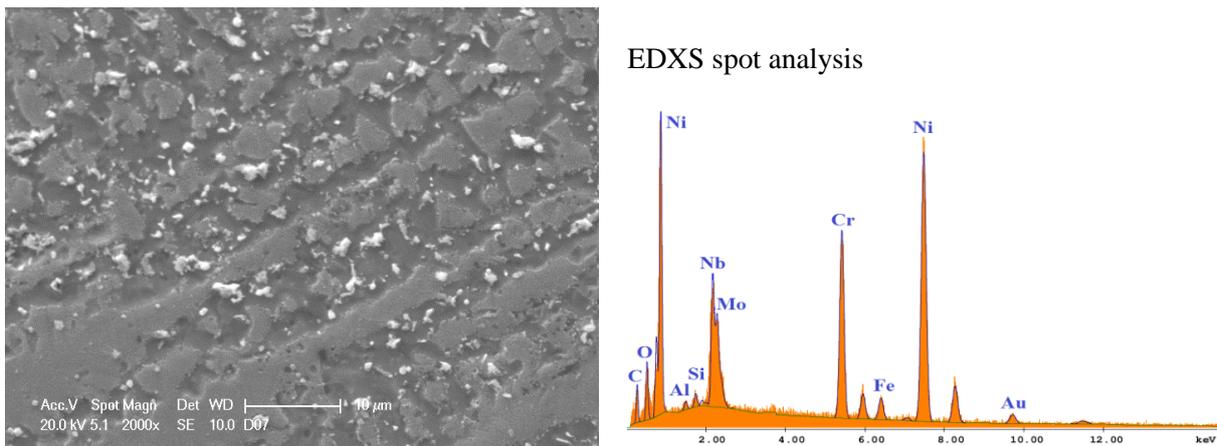
*Figure 3.46. Microstructures of the clad with dilution equal to 3.9% and EDXS spectrum of the precipitate.*



EDXS spot analysis
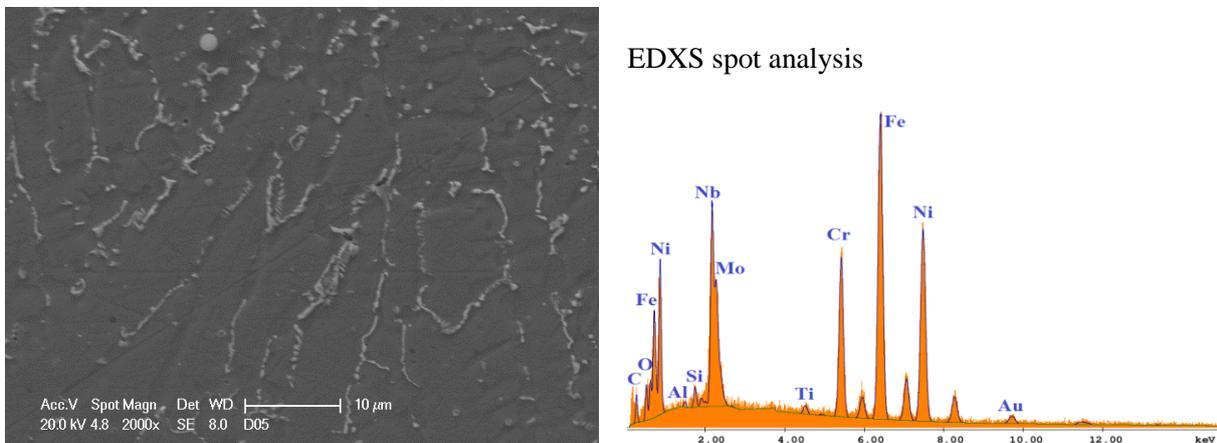
*Figure 3.47. Microstructures of the clad with dilution equal to 45.0% and EDXS spectrum of the precipitate.*

Both of the microstructures show a dendritic γ face-centred cubic phase enriched in Ni, Cr and Fe, which is obviously higher in the clad where substrate dilution is more pronounced. Precipitates of the less diluted clad are rich in Nb and Mo, while Ni, Cr and a small amount of Fe come from the matrix. A significative peak of carbon is also detected, even if quantitative analysis of C with EDXS has not been considered. Precipitates of the more diluted clad are also rich in Nb and Mo, but a higher amount of nickel and iron and a smaller peak of carbon are revealed.

The different microstructures can be justified by analysing the solidification behaviour of the Inconel 625 alloy. Solidification of this alloy begins with the formation of γ dendrites which is enriched in nickel, chromium and iron and depleted in molybdenum and niobium. These elements segregate to the interdendritic regions and, as the solidification proceeds further, the content of Nb and Mo into the interdendritic liquid increases. The solidification process of Inconel 625 usually ends with the formation of the Laves constituents or the niobium carbides (NbC) in these interdendritic regions: Laves phases have generally hcp-structure, irregular shape and contain significant amount of other alloying of impurity elements; carbides appear as blocky and dendritic Chinese-script morphology at the grain boundary [150,151].

The formation of either Laves phases and niobium carbides in the microstructure is mainly influenced by the chemical composition of the alloy. NbC is usually favoured by carbon and consequently by high C/Nb ratios (Figure 3.48); on the opposite, iron and silicon promote the Laves phases: at low C/Nb ratios, Laves and no NbC are formed. However, microstructures without niobium carbides are not so common and requires very low carbon content (*C < 0.01%*) [152].
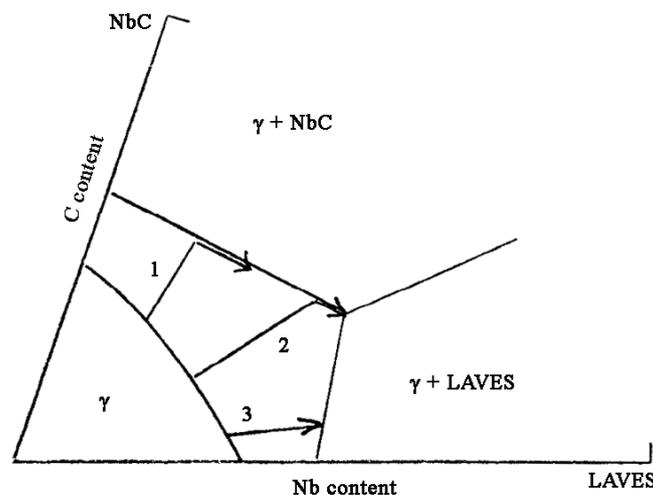


*Figure 3.48. Extract from the pseudo-equilibrium diagram for Alloy 718 (modification of Inconel 625) showing the formation of Laves phase during solidification [152].*

On these bases, interpretation of the microstructures and the effect of dilution is proposed, as follows. The chemical composition of the substrate (mild steel) is reported in Table 2.1. Substrate dilution brings iron, carbon and silicon into the clad, and these elements, as said before, have a concurrent effect. When dilution is limited, the increases of iron and silicon are too low to induce the formation of Laves phases: interdendritic regions shows the formation of niobium carbides having principally blocky morphology. On increasing dilution, Fe and Si promote the formation of both the Laves phases, visible in the microstructure as the irregular-shaped particles, and the NbC having lamellar eutectic-type morphology.

The different phases detected in the interdendritic regions, their different shape and the total amount of eutectic region contribute to the decrease in microhardness of the alloy, as it can be seen in Figure 3.49 where the average microhardness of the clad is reported as a function of the clad dilution.
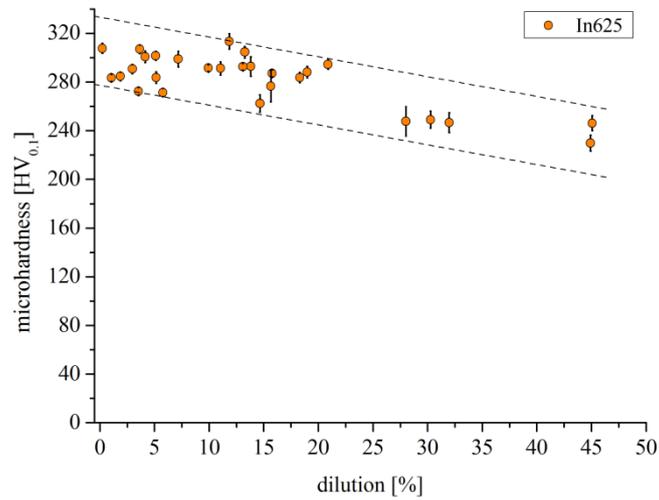


*Figure 3.49. $HV_{0.1}$ Microhardness of the clads as a function of dilution.*

Figures 3.50 show the thermogravimetric curves of the isothermal oxidation up to 3 h at different temperatures (1100 and 1200°C respectively) for clads with different amount of dilution.
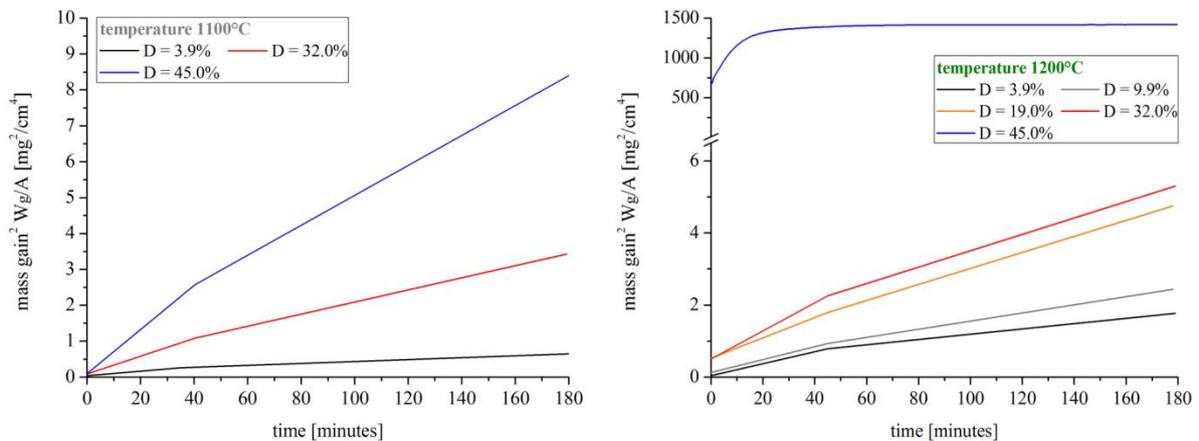


*Figure 3.50. Thermogravimetric curves at 1100°C (left) and 1200°C (right) for different values of clad dilution.*

At first sight, it is well evident that oxidation increases with temperature and dilution as expected: when clads with the same amount of dilution are compared, the square of the mass gain per unit surface area $(W_g/A)^2$ is always higher at 1200°C than at 1100°C. Moreover, at both the oxidizing temperatures, $(W_g/A)^2$ increases on increasing dilution.

From a practical point of view it is interesting to notice that, in terms of weight gain, the increase in substrate dilution from 3.9 to 32.0% (which can be expressed as a variation in the average iron in the alloy from 3.7 to 32.0%) is worse than the increase in the oxidizing temperature from 1100 to 1200°C. This is visible in Table 3.6, where the values of $W_g/A$ after three hours of oxidation are reported.

*Table 3.6. Total mass gain after three hours at different temperatures for different values of dilution.*

| dilution [%] | temperature 1100°C, 3 h mass gain [mg/cm²] | temperature 1200°C, 3 h mass gain [mg/cm²] |
|---|---|---|
| 3.7 | 0.8 | 1.3 |
| 9.9 | - | 1.6 |
| 19.0 | - | 2.2 |
| 32.0 | 1.9 | 2.3 |
| 44.9 | 2.9 | 37.7 |

As a rule for the high temperature oxidations of metals, the data fitting allows to give important information regarding the mechanism of the oxidation process [153]. Excluding the sample with the highest dilution at 1200°C, which shows catastrophic oxidation, the oxidation kinetics follow parabolic trends, as highlighted in Figure 3.50 by the linear trends. In particular, all the oxidation curves can be fitted using a combination of two parabolic functions and show a transition to a lower oxidation rate step after a certain time (about 30 – 50 minutes) during the isothermal holding. Oxidation rates of the different stages are reported in Table 3.7.

*Table 3.7. Oxidation rates in the two stages at different temperatures for different values of dilution.*

| dilution [%] | temperature 1100°C, 3 h 1st stage oxidation rate [mg²/cm⁴min] | 2nd stage oxidation rate [mg²/cm⁴min] | temperature 1200°C, 3 h 1st stage oxidation rate [mg²/cm⁴min] | 2nd stage oxidation rate [mg²/cm⁴min] |
|---|---|---|---|---|
| 3.7 | 0.006 | 0.003 | 0.017 | 0.007 |
| 9.9 | - | - | 0.018 | 0.011 |
| 19.0 | - | - | 0.037 | 0.022 |
| 32.0 | 0.025 | 0.017 | 0.037 | 0.022 |
| 44.9 | 0.061 | 0.042 | * | * |

*catastrophic oxidation

Figure 3.51 shows, as a function of dilution and for the different oxidizing temperatures, the relative decrease in the oxidation rate between the first and the second stage. This value basically expresses the attenuation of the oxidation behaviour during the isothermal test: the higher is this value, the higher is the decrease in the slope of the straight line in Figure 3.50.
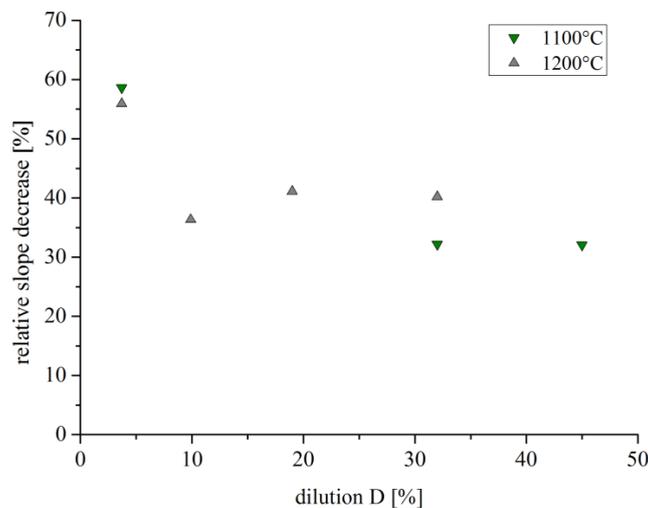


*Figure 3.51. Relative decrease in the oxidation rate when passing from first to second stage as a function of clad dilution.*

On increasing dilution, the attenuation of the oxidation kinetic is lower, leading to a higher mass gain. The drop in the attenuation of the oxidation kinetic is visible at both the oxidizing temperatures and seems to be affected by dilution: for a low value of dilution, which means that the chemical composition of the alloy is close to the one of the cladding material, the attenuation of the oxidation rate is higher and it is not influenced by the testing temperature. On increasing dilution from 3.7 to 9.9%, this value decreases and remains lower at any other value of higher dilution.

As known by literature, high temperature parabolic oxidation signifies that thermal diffusion of ions is controlling the rate of the process. Such a process can be therefore correlated with a uniform diffusion of the reactants through a growing compact scale [154]. The transitions in the oxidation behaviour, which are accompanied by the reduction of the oxidation rates, may be for instance induced by compositional changes of the oxide scale [155,156]. For a better interpretation of this behaviour, characterization of the oxide scales has been carried out.

XRD patterns of the oxidized specimens at different values of dilution are reported in Figure 3.52.
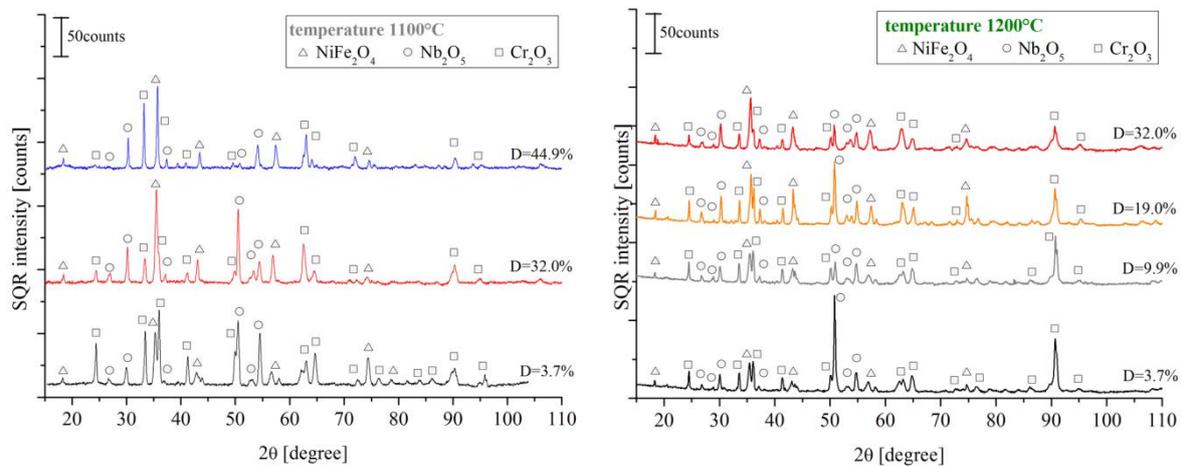


*Figure 3.52. XRD patterns of the oxidized specimens at different values of dilution and for different oxidizing temperatures: 1100°C (left) and 1200°C (right).*

In the sample with the highest amount of dilution treated at 1200°C, where catastrophic oxidation has occurred, XRD analysis was not possible. All the other samples, irrespective of the amount of dilution and the oxidizing temperature, show the presence of three oxides: chromium oxide ($Cr_2O_3$), nickel ferrite ($NiFe_2O_4$) and niobium pentoxide ($Nb_2O_5$). According to the experimental condition adopted, the depth analysed by XRD is representative of the whole oxide scale.

The structure and the morphology of the oxidised surface of clads with different dilution and oxidizing temperatures are reported in Figure 3.53, while a micrograph at a higher magnification of the typical oxidation scale formed is reported together with the results of the EDXS analysis in Figure 3.54.
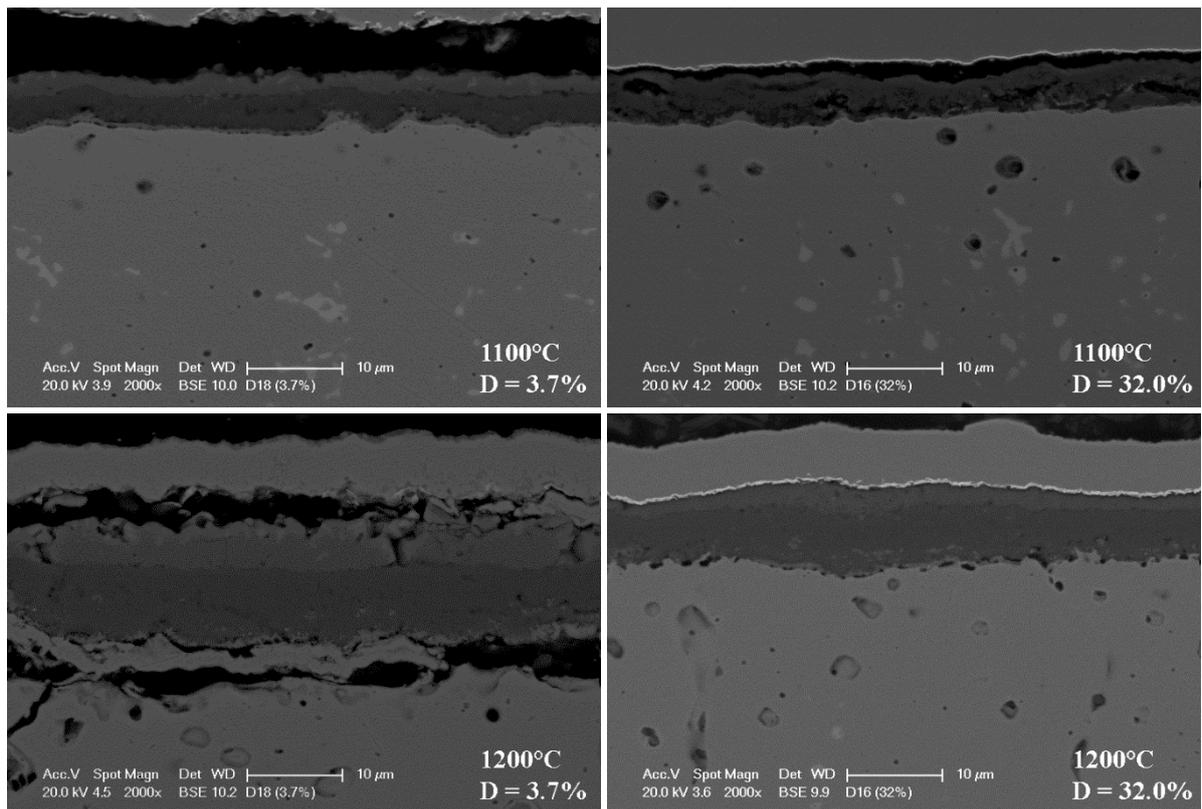
*Figure 3.53. Oxide scales of clad with different dilutions formed at different oxidizing temperatures.*
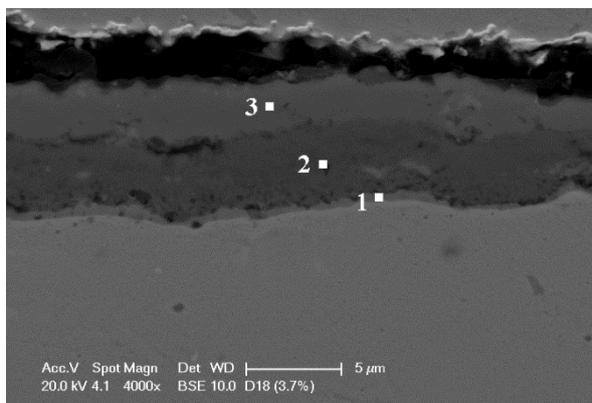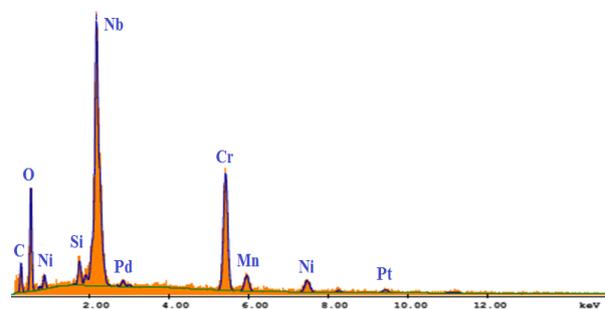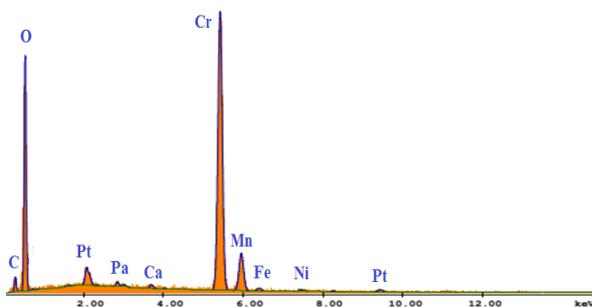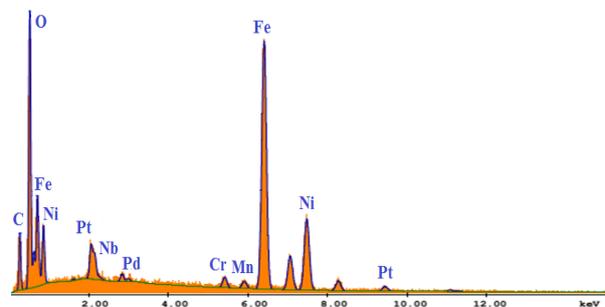


*Figure 3.54. EDXS spot analysis of the different oxide scales: (1) $Nb_2O_5$, (2) $Cr_2O_3$ and (3) $NiFe_2O_4$.*

In all the micrographs, the presence of three different layers forming the oxide scale is highlighted. The outer layer, which is rich in iron and nickel, can be identified by the mixed $NiFe_2O_4$ oxide. The

intermediate layer, formed principally by chromium, is the chromium (III) oxide $Cr_2O_3$. The inner layer, which is significantly thinner than the others, is mostly made of niobium and can be thus identified by the $Nb_2O_5$, confirming the results of XRD analyses.

In order to investigate the formation of this composite oxide scale, tests at different temperature have been executed.

In Figure 3.55, an example of the oxide scale formed at 550°C for 20 minutes, representative of all the samples at different dilution and temperatures, is reported together with the EDXS analysis.
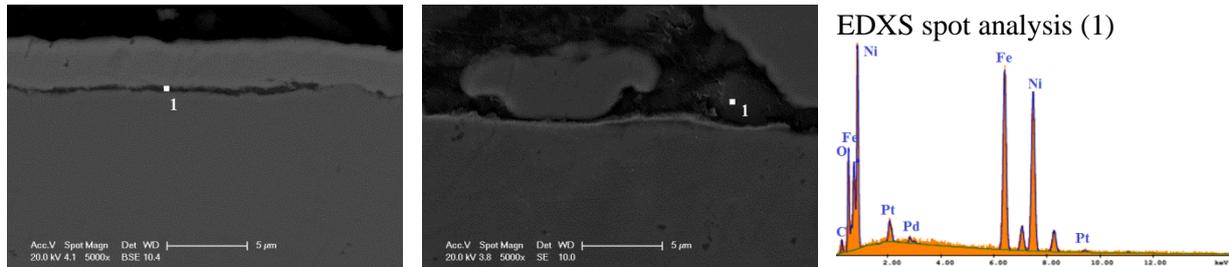


*Figure 3.55. Oxide scale formed at 550°C and respective EDXS analysis.*

Due to the low adhesion between iron-rich oxide and nickel-based substrate, the oxide layer is not continuous and results to be partially detached along the sample surface. However, EDXS spot analysis in the zone where it is well-visible reveals the formation of the mixed $NiFe_2O_4$ oxide in both the samples investigated (high dilution, 32.0%, and low dilution, 3.7%).

In Figure 3.56, an example of the oxide scale formed at 1100°C for 20 minutes, representative of all the samples at different dilution and temperatures, is reported together with the EDXS analysis.
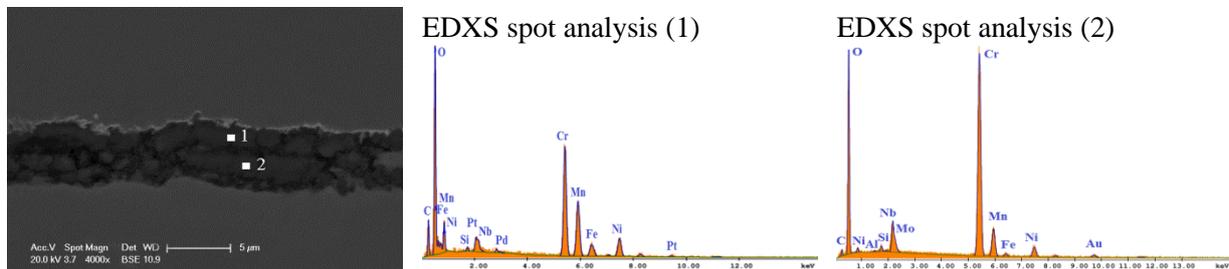


*Figure 3.56. Oxide scale formed at 1100°C and respective EDXS analysis.*

After 20 minutes at 1100°C, the oxide scale reveals both the mixed $NiFe_2O_4$ oxide layer, formed at lower temperature, and the $Cr_2O_3$ oxide layer, which however does not show the typical aspect of a compact and protective layer. Only small traces of the niobium oxide are evidenced by metallographic analysis.

The identification of the oxidation mechanism in a multicomponent alloy in which more than one element can form a stable oxide is always difficult. However, on the basis of these results, a possible interpretation of the oxidation behaviour at the two temperatures for the different values of dilution is given.

As demonstrated by the test at 550°C, the first oxide forming on the alloy surface is the mixed Fe-Ni oxide ($NiFe_2O_4$). Some traces of other reactive components present in In625 alloy, such as Si, Cr or Mo, are revealed by EDXS analysis in the outer layer, but their respective oxide is not detected in the XRD patterns. The partitioning between iron and nickel is not proportional to the chemical composition of the alloy since, unconditionally from the amount of iron dilution, a large presence of Fe is measured.

The formation of this oxide scale starts on heating.. In fact, the initial value of $W_g/A$ when the isothermal stage start is always a little higher than 0. This behaviour is obviously enhanced in the tests made at 1200°C. The formation of this oxide occurs rapidly with a high oxidation rate, which is favoured by a higher oxidizing temperature and by iron dilution.

When the heating-up stage progresses, on a second stage a Cr-rich oxide layer ($Cr_2O_3$) and subsequently a Nb-rich oxide layer ($Nb_2O_5$) start to form. On increasing the temperature above 600-650°C, chemical reactions at the interface between the oxide and the alloy lead to the formation of the thermodynamically more stable phases such us Cr-oxides and Nb-oxides. In fact, as reported in literature, the thermodynamic stability of the oxides principally governs selective oxidation of an element in an alloy. Simply considering the thermodynamic data, in an Inconel 625 alloy the stability of the various oxides can be represented in the following order

$$Si > Nb > Cr > Mo \cong Fe > Ni \qquad (3.48)$$

When the specimens reach the oxidizing temperature and the isothermal holding starts, the formation of the Cr (and Nb) oxide layer has already started (as shown by the test at 1100°C) and some extents of the Cr-rich and Nb-rich layers are already visible. On increasing the time, the $Cr_2O_3$ layer becomes protective and oxidation slows down: oxidation rate decreases and the transition from the first to the second parabolic stages occurs.

### 3.7.3  NiBSi

NiBSi alloy powder has been cladded onto different substrates (mild steel and grey cast iron) in different processing condition to obtain different values of dilution, and a preliminary study of the effect of dilution on microstructure and microhardness has been conducted.

The evolution of the microstructures of the clads on increasing dilution is evidenced in Figures 3.57 - 3.58, where micrographs of the clads produced on the mild steel with different dilution are reported. EDXS analysis of the different constituents has been carried out (Figures 3.59), and results have been summarized in Tables 3.8 – 3.9 as a function of the clad dilution. Due to their low atomic weight, carbon and boron have been excluded from this analysis.

Solidification of the NiBSi alloy starts with the formation of the austenitic primary dendrites (Figure 3.59,a) made of nickel and, on increasing dilution, of iron coming from the substrate. The interdendritic region consists in the γ-nickel-boride eutectic, which can be present in two different forms visible in Figure 3.59 (b) and Figure 3.59 (c), the nickel-boride nickel-silicide eutectic (Figure 3.59,d) and austenite (dark grey region in Figure 3.59,e) [157,158].

The difference between the various constituents is highlighted by the presence of silicon in the EDXS analysis (Tables 3.8 – 3.9): the nickel-boride nickel-silicide eutectic shows the highest percentage of silicon, while it lowers in the γ-nickel-boride. The content of Si in the primary dendrites, averaged on the different values of dilution, is about 2.8% in both the cases (preheated and not preheated substrate), while no significant silicon content is evidenced in austenite, which is principally made of nickel.
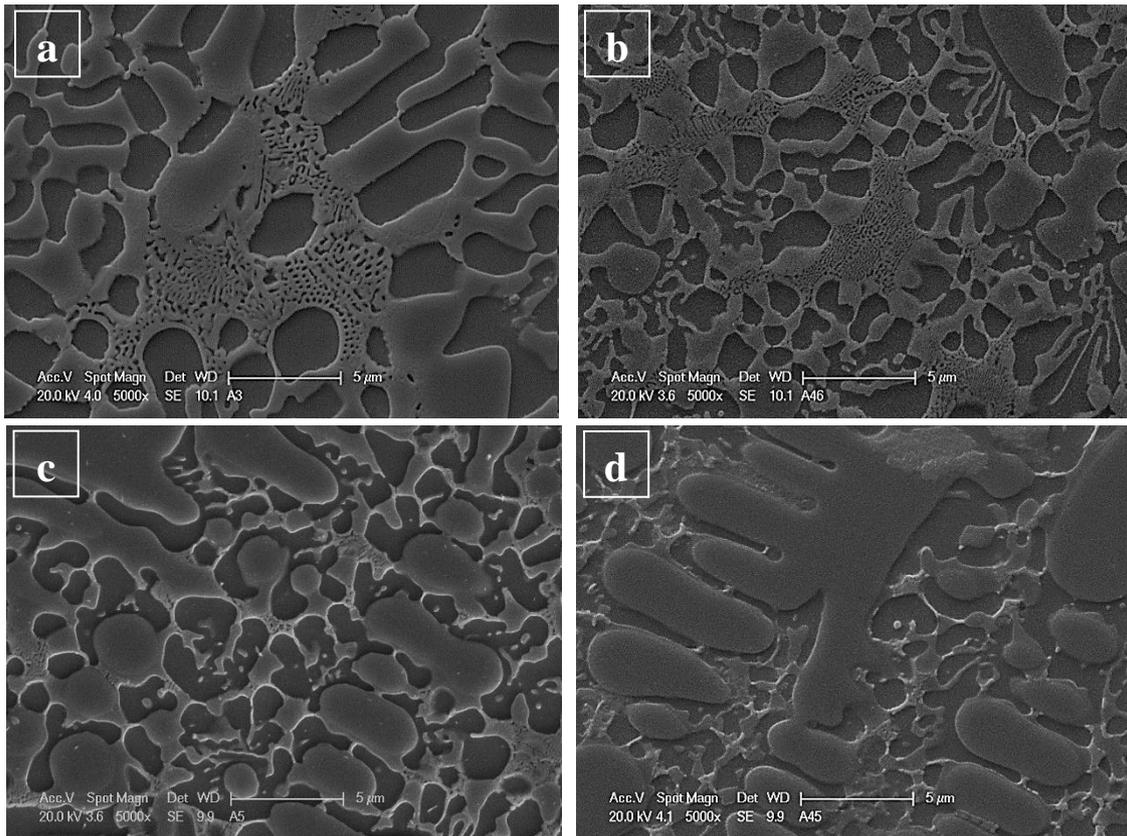
*Figure 3.57. Microstructures of the clads produced on the not preheated mild steel for different values of dilution: (a) D = 1.0%, (b) D = 16.7%, (c) D = 25.0% and (d) D = 30.8%.*
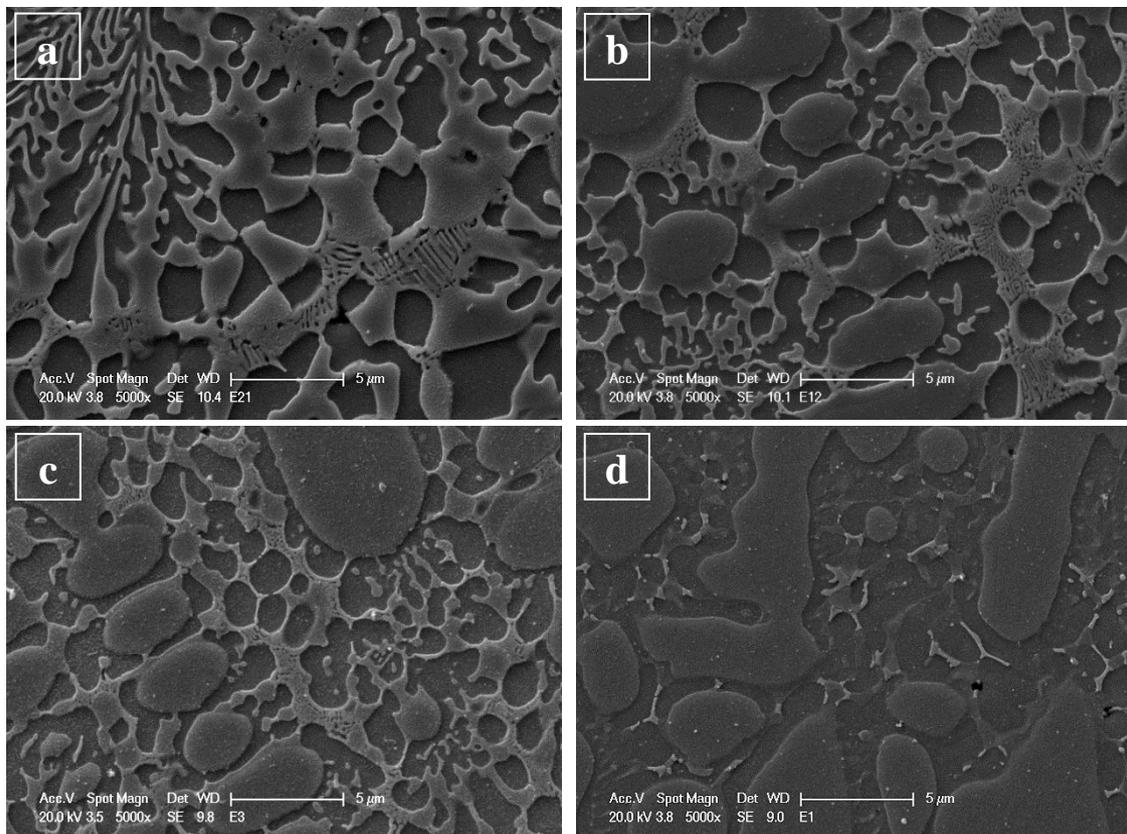


*Figure 3.58. Microstructures of the clads produced on the preheated mild steel for different values of dilution: (a) D = 0.8%, (b) D = 19.9%, (c) D = 28.0% and (d) D = 55.6%.*
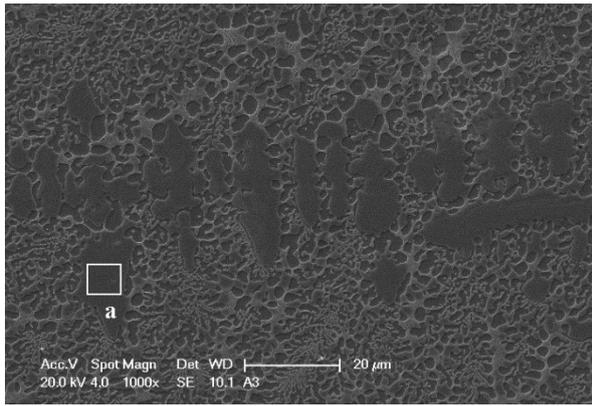
EDXS analysis (a)
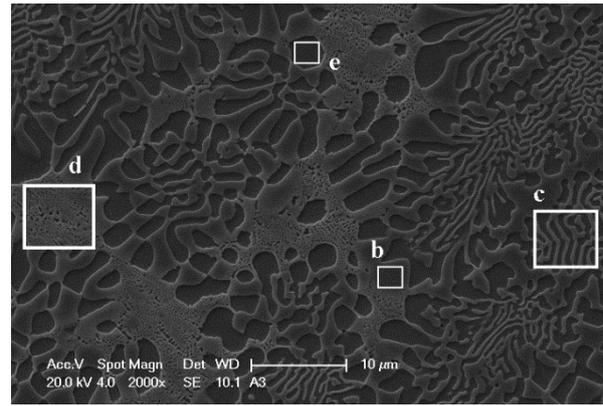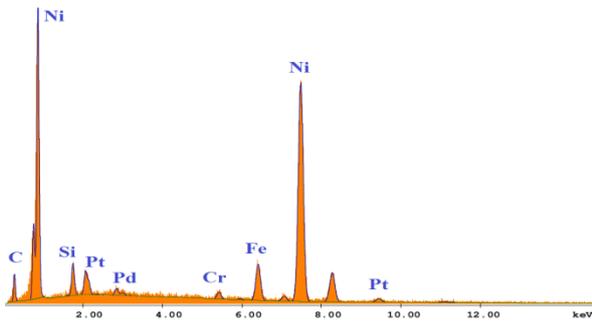


EDXS analysis (b)
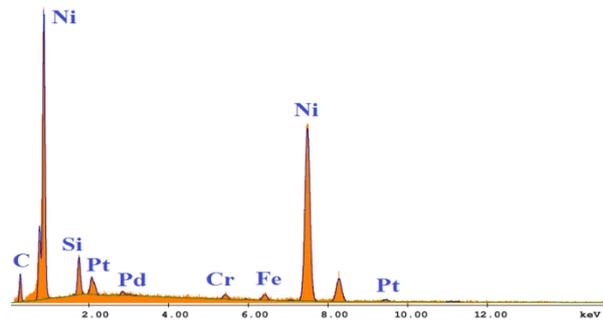


EDXS analysis (d)
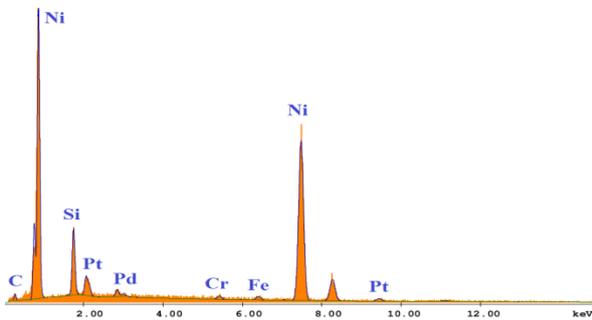


EDXS analysis (e)
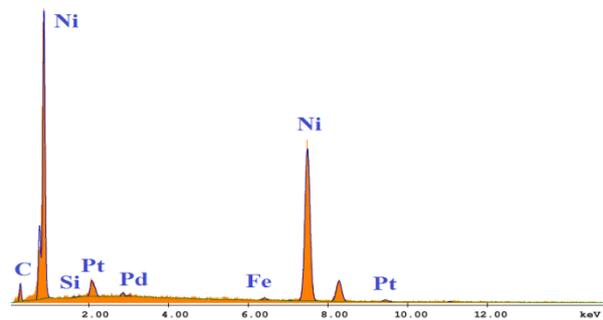


*Figure 3.59. Morphology and EDXS analysis of the different phases observed: (a) austenitic primary dendrites, (b,c) γ-nickel-boride eutectic, (d) nickel-boride nickel-silicide eutectic and (e) austenite.*

*Table 3.8. Quantitative EDXS analysis of the phases observed in clads produced on the not preheated mild steel for different dilution values.*

|  | dilution [%] | Si [%] | Fe [%] | Ni [%] | Cr [%] |
|---|---|---|---|---|---|
| austenitic primary dendrites | 1.0 | 3.5 | 7.9 | 87.4 | 1.2 |
|  | 30.8 | 2.4 | 29.3 | 67.5 | 0.8 |
| Ni-boride Ni-silicide eutectic | 1.0 | 9.7 | 1.1 | 88.3 | 0.9 |
|  | 30.8 | 8.2 | 8.2 | 81.2 | 0.9 |
| γ-Ni-boride eutectic | 1.0 | 5.5 | 1.7 | 91.7 | 1.1 |
|  | 30.8 | 4.5 | 8.5 | 86.2 | 0.8 |
| austenite | 1.0 | 0.2 | 0.8 | 99.0 | - |
|  | 30.8 | - | 7.9 | 91.3 | 0.9 |

*Table 3.9. Quantitative EDXS analysis of the phases observed in clads produced on the preheated mild steel for different dilution values.*

|  | dilution [%] | Si [%] | Fe [%] | Ni [%] | Cr [%] |
|---|---|---|---|---|---|
| austenitic primary dendrites | 0.8 | 3.7 | 4.1 | 91.1 | 1.1 |
|  | 55.6 | 1.8 | 50.4 | 47.2 | 0.6 |
| Ni-boride Ni-silicide eutectic | 0.8 | 9.6 | 2.1 | 87.3 | 1.0 |
|  | 55.6 | 8.3 | 17.1 | 73.8 | 0.7 |
| γ-Ni-boride eutectic | 0.8 | 5.7 | 3.2 | 90.2 | 0.9 |
|  | 55.6 | 2.4 | 25.2 | 71.4 | 1.0 |
| austenite | 0.8 | - | 2.0 | 97.3 | 0.6 |
|  | 55.6 | 0.7 | 25.9 | 72.6 | 0.8 |

On increasing dilution, microstructure evolves in two different ways: first of all, the volumetric partitioning of dendritic and interdendritic region changes. Secondly, the morphology of the eutectic formed is modified.

To investigate the first microstructural change, the percentage of the dendritic region has been measured with Image Analysis using the LOM micrographs for different dilution values, as shown for instance in Figure 3.60 for the clads produced on the preheated substrate.
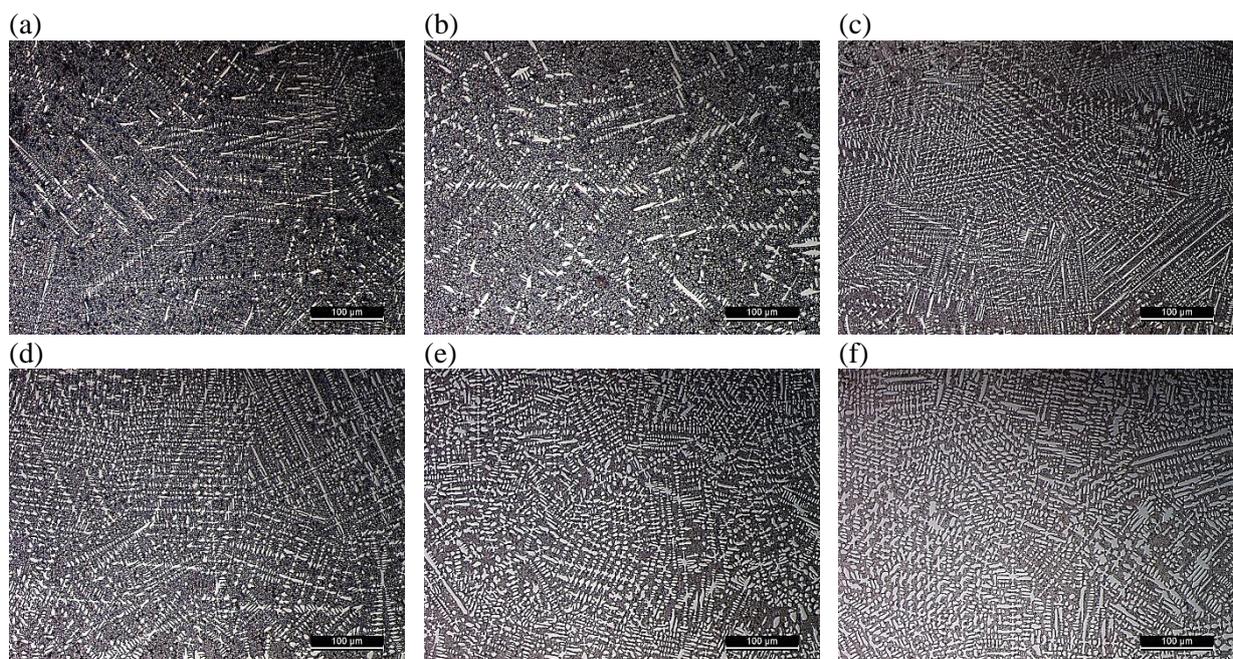


*Figure 3.60. Microstructures of the clads produced on the preheated mild steel with different dilution:*
*(a) D = 0.8%, (b) D = 5.0%, (c) D = 11.6%, (d) D = 19.9%, (e) D = 28.0% and (f) D = 41.0%.*

As it can be seen in Figure 3.61, where the percentage of the dendritic region is plotted as a function of clad dilution, on increasing dilution microstructure becomes more dendritic and consequently the total amount of eutectic decreases. This condition is noticed in both the cases, when substrate is preheated and not preheated.
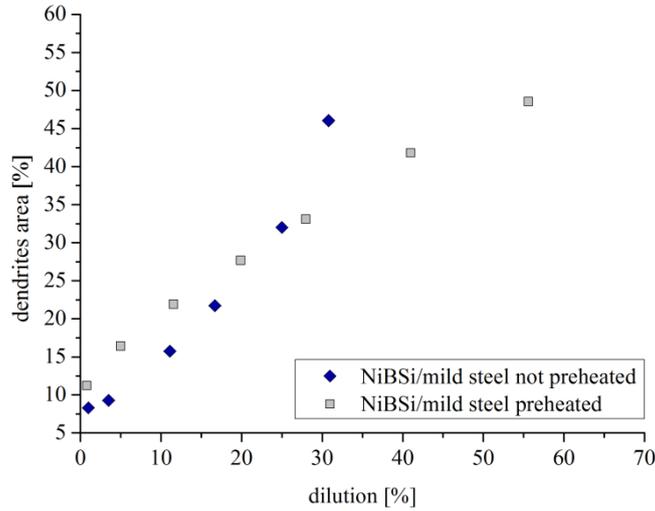
*Figure 3.61. Percentage of the dendritic region as a function of clad dilution.*

The different solidification structure can be justified on the basis of the liquid resulting from dilution. With substrate dilution the chemical composition of the NiBSi alloy is mainly modified by the addition of iron. The change of the chemical composition of the alloy due to dilution is expected to move the resulting composition of the liquid alloy far from eutectic points, thus promoting proeutectic solidification.

The evaluation of the effect of substrate preheating on final microstructure is again a consequence of the increased dilution. In Figure 3.62 is reported a comparison of the percentage of the dendritic region on the clads produced with the same processing parameters on the preheated and not preheated substrate respectively.
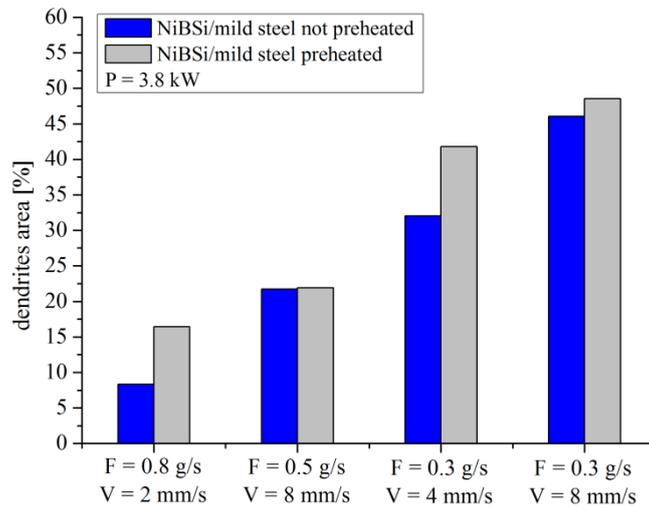


*Figure 3.62. Percentage of the dendritic region for clads produced in different conditions.*

The second microstructural evolution occurring on increasing dilution regards the modification of the eutectic morphology, which is visible in both the conditions of preheated and not preheated substrate. With the increase in dilution, eutectic morphology evolves towards the condition shown in Figure 3.63: the γ-nickel-boride eutectic, which is present in lower percentage, evidences only the form

visible in Figure 3.59 (b), while a silicon-rich precipitate (Figure 3.63,a) starts to be present at the expense of the nickel-boride nickel-silicide eutectic, that tends to disappear.
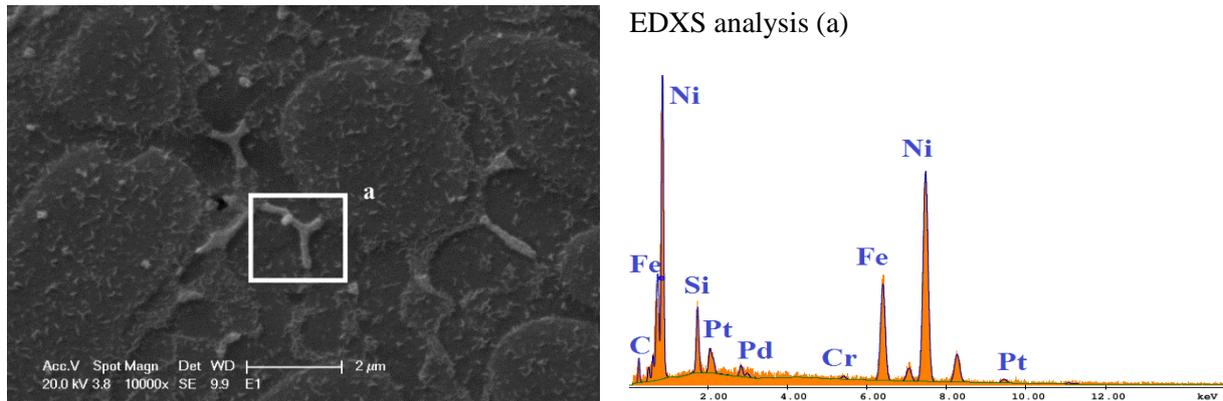


*Figure 3.63. Morphology and EDXS analysis of the silicon-rich eutectic formed when dilution is high.*

These microstructural changes are responsible of the correlation between microhardness and dilution: in fact, on increasing clad dilution, microhardness of the clad decreases (Figure 3.64).
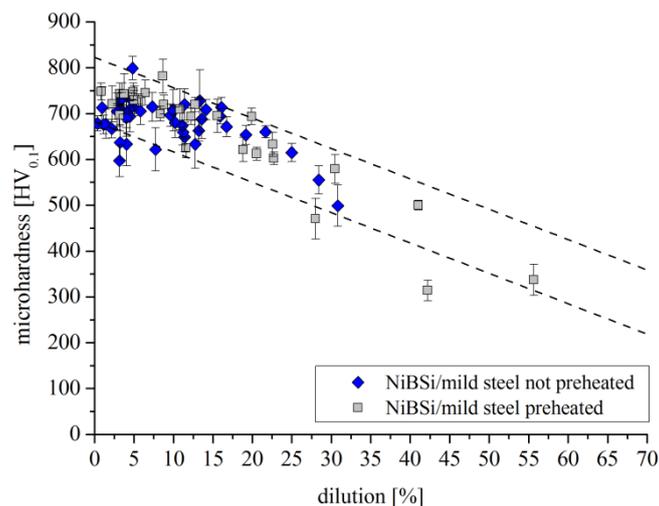


*Figure 3.64. Microhardness of the clads produced on the mild steel as a function of dilution.*

Even if the iron dilution contributes to the solid-solution strengthening of the austenitic primary dendrites [144], the lower quantity and the different morphology of the eutectic constituent formed cause the substantial decrease in clad microhardness, as visible in Figure 3.64.

In Figure 3.65, the microstructures of the clads produced on the grey cast iron substrate for different values of dilution are reported, while the results of the EDXS analysis are shown in Table 3.10.
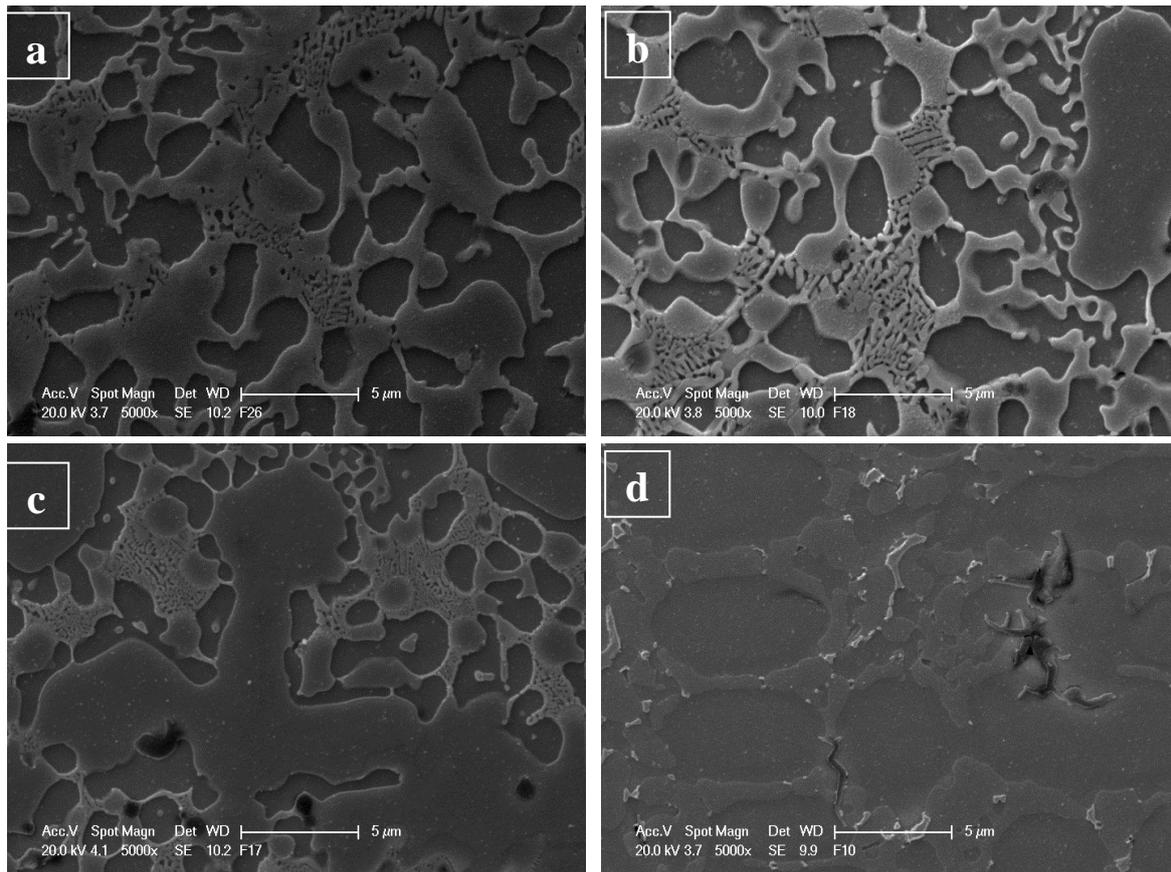
*Figure 3.65. Microstructures of the clads produced on the preheated grey cast iron for different values of dilution: (a) D = 2.1%, (b) D = 16.0%, (c) D = 27.7% and (d) D = 58.7%.*

*Table 3.10. Quantitative EDXS analysis of the phases observed in clads produced on the preheated grey cast iron for different dilution values.*

|  | dilution [%] | Si [%] | Fe [%] | Ni [%] | Cr [%] |
|---|---|---|---|---|---|
| austenitic primary dendrites | 2.1 | 3.6 | 8.9 | 87.5 | - |
|  | 27.7 | 3.1 | 25.5 | 72.4 | - |
| Ni-boride Ni-silicide eutectic | 2.1 | 10.0 | 5.0 | 85.0 | - |
|  | 27.7 | 7.4 | 16.1 | 76.5 | - |
| γ-Ni-boride eutectic | 2.1 | 2.8 | 6.7 | 90.5 | - |
|  | 27.7 | 4.0 | 24.1 | 71.9 | - |
| austenite | 2.1 | - | 5.0 | 95.0 | - |
|  | 27.7 | - | 20.8 | 79.2 | - |

The same microstructural evolution is evidenced for the clads produced on the grey cast iron substrate. For low dilution values, the solidification microstructure consists in the austenitic primary dendrites, the γ-nickel-boride eutectic, present in the form shown in Figure 3.59 (b), the nickel-boride nickel-silicide eutectic and austenite. On increasing dilution microstructure is modified as before: as evidenced by Figure 3.65, the partitioning of dendritic and interdendritic region changes, and a higher amount of austenitic primary dendrites is found.
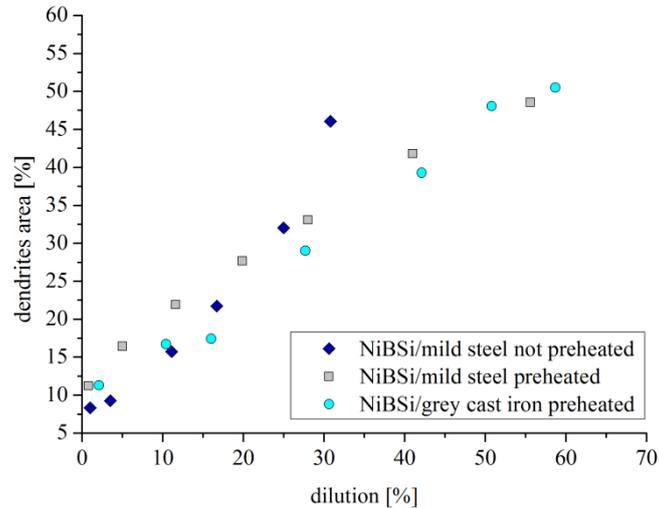
*Figure 3.66. Percentage of the dendritic region as a function of clad dilution.*

The morphology of the eutectic formed also evolves to the γ-nickel-boride eutectic and the silicon-rich precipitates, as shown in Figure 3.65 (d). In addition, on increasing dilution the presence of the graphite coming from the substrate is evidenced. As confirmed by literature, graphite morphology seems to change from spheroidal (Figure 3.65,c) to vermicular and flake (Figure 3.65,d) on decreasing the *G/R* ratio, i.e. on increasing dilution.

The presence of the graphite does not alter the correlation between microhardness and clad dilution (Figure 3.67): on increasing dilution, microhardness of the clads produced with the NiBSi alloy powder decreases.
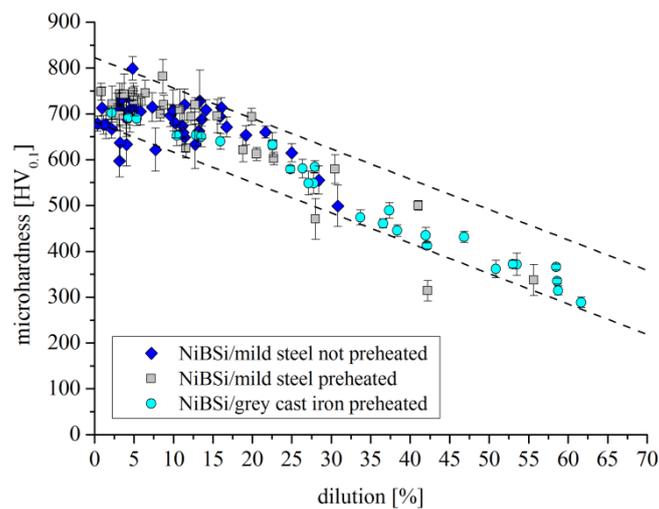


*Figure 3.67. Microhardness of the NiBSi clads as a function of dilution.*

## 3.7.4  Stellites + WC

Mixtures of Stellite12 powder/tungsten carbides and Stellite21 powder/tungsten carbides have been cladded onto a mild steel substrate (preheated at 400°C and not) in different processing conditions (varying the laser power) to obtain different conditions of carbides dissolution.

The EDXS maps of different elements (W, Cr, Co, C and Fe) in the carbide, in the interface and in the matrix are shown in Figure 3.68.
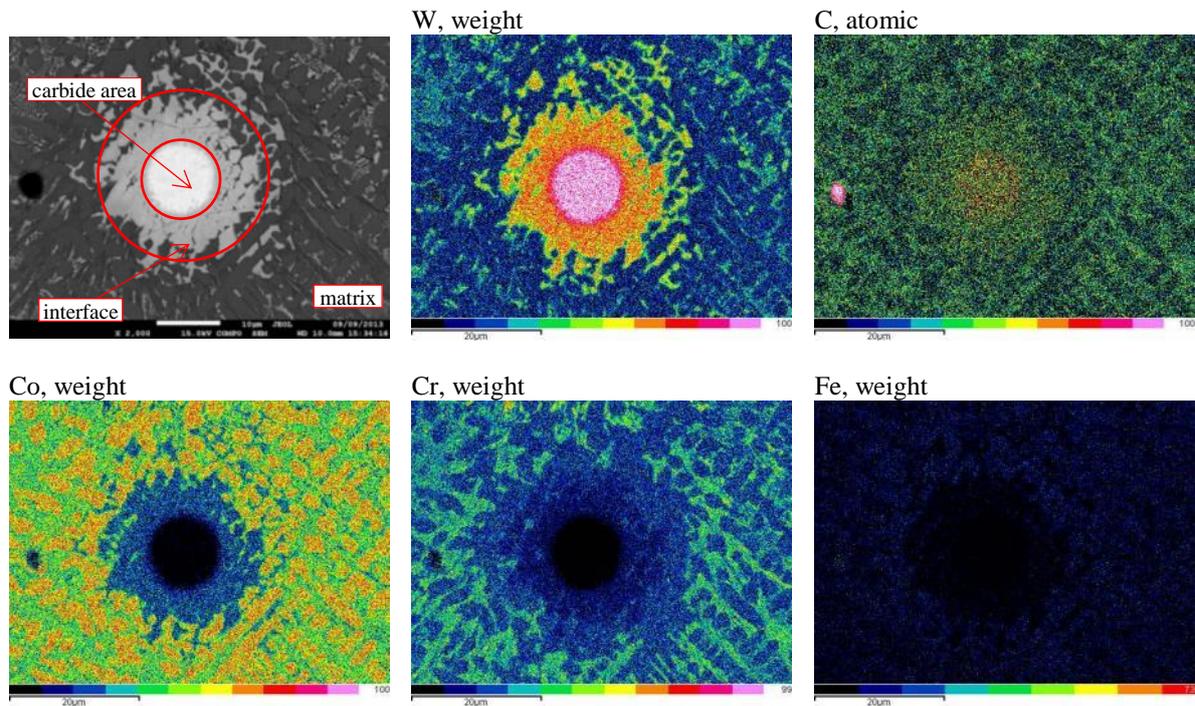


*Figure 3.68. EDXS maps for the different elements present into the material.*

The tungsten carbide is well identified by the W and C maps (Figure 3.68): the microanalysis reveals about 50 atomic % of both tungsten and carbon in the carbide area.

In the interface constituent tungsten, carbon, cobalt and chromium are detected; the continuous shell and the globular particles surrounding WC are W-Cr carbides, while cobalt comes from the interparticle matrix. W-Cr carbides are well compact close to the WC particle and increasingly fragmented on moving from it towards the matrix. The fine eutectic constituent in the matrix is a microstructural constituent of Stellite made of the metallic matrix and two different types of carbides: the white one, Cr-rich ($M_7C_3$), and the dark grey one, Cr-W rich ($M_{23}C_6$).

Iron, which is present in higher amount than in the starting powder because of the substrate dilution, is concentrated in the matrix dendrites.

Dissolution of carbides in the different clads, measured as explained in Appendix 1, is reported in Figure 3.69 as a function of the laser power.
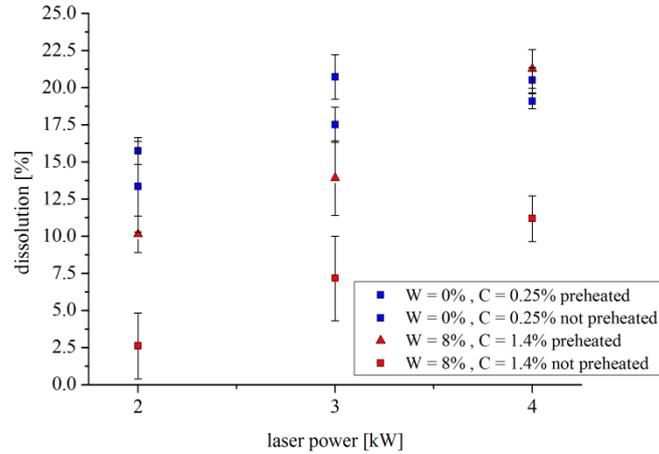
*Figure 3.69. Carbides dissolution as a function of the laser power for the different materials, preheated and not.*

There is a clear influence of the stellite chemical composition on the dissolution of the carbides: for all the processing conditions, the carbides in the clads produced with Stellite12, which contains a high amount of tungsten and carbon, are much less dissolved than those in Stellite21, where no tungsten and 0.25% of carbon are present.

Dissolution is confirmed by the EDXS analysis made on samples produced at 4 kW, 5 mm/s and without preheating. Results reported in Table 3.11 highlight that in both the cases the tungsten and carbon content is higher than in the starting cobalt alloy.

*Table 3.11. Nominal chemical composition of the starting powder used for the matrix and chemical composition measured with EDXS in the matrix of samples made at 4 kW.*

| Material | Particle size | Co | Cr | W | Ni | Fe | Mo | C | Si |
|----------|---------------|------|------|------|------|------|------|------|------|
|          | [μm]          | [%]  | [%]  | [%]  | [%]  | [%]  | [%]  | [%]  | [%]  |
| Stellite21 | powder composition | bal. | 27.0 | - | 2.8 | 1.5 | 5.5 | 0.25 | 1.0 |
| (4kW) | matrix EDXS analysis | 45.1 | 20.7 | 18.0 | 2.0 | 6.6 | 4.5 | 2.9 | 0.2 |
| Stellite12 | powder composition | bal. | 28.5 | 8.0 | 1.5 | 1.0 | - | 1.4 | 1.1 |
| (4kW) | matrix EDXS analysis | 44.5 | 21.6 | 23.0 | 1.2 | 6.2 | - | 3.2 | 0.1 |

In sample made with Stellite21 tungsten and carbon contents increase up to 18.0% and from 0.3 up to 2.9%, respectively, while in the sample made with Stellite12, where dissolution is lower, the tungsten and carbon contents increases from 8.0 up to 23.0% and from 1.4 up to 3.2%, respectively.

While other parameters remain unchanged, dissolution of tungsten carbides always increases with the increase in the laser power. Indeed an increase in the laser power leads to a higher temperature of the melt pool, which enhances dissolution phenomena.

The preheating treatment increases the dissolution of the carbides. In the clads made with the same material and processing conditions, the dissolution of carbides in the preheated clads is higher than the one in the not preheated clads. This behaviour is also due to a higher average temperature reached by the melt pool during the process when the substrate is preheated, which is again responsible of an enhanced dissolution.

Figure 3.70 shows that WC particles are either spherical or irregular. The average percentage of spherical carbides for all the measured clads (independently from the material and the processing conditions) is 71%, which is almost the same percentage present in the starting powder.
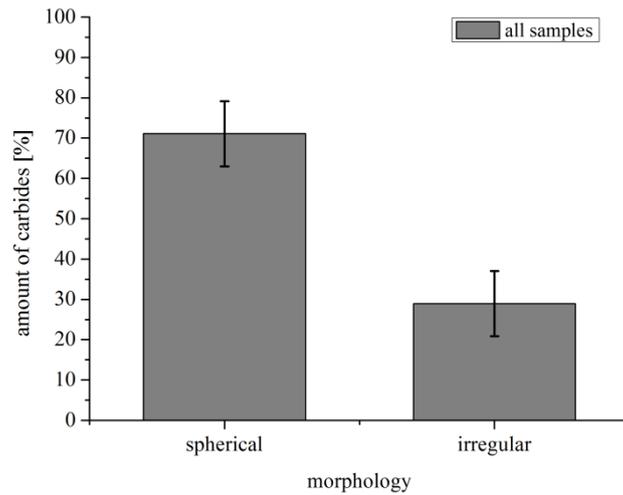
*Figure 3.70. Average percentage of spherical and irregular carbides according to their morphology for all the samples measured.*

This reveals that the dissolution process is not selective in relation to the morphology of the carbide particles.

As previously mentioned, some of the carbides particles display a shell of W-Cr carbides, more or less compact, at the interface with the matrix.

Figure 3.71 shows the amount of carbide particles with and without the interfacial microstructural constituent in all the specimens investigated.
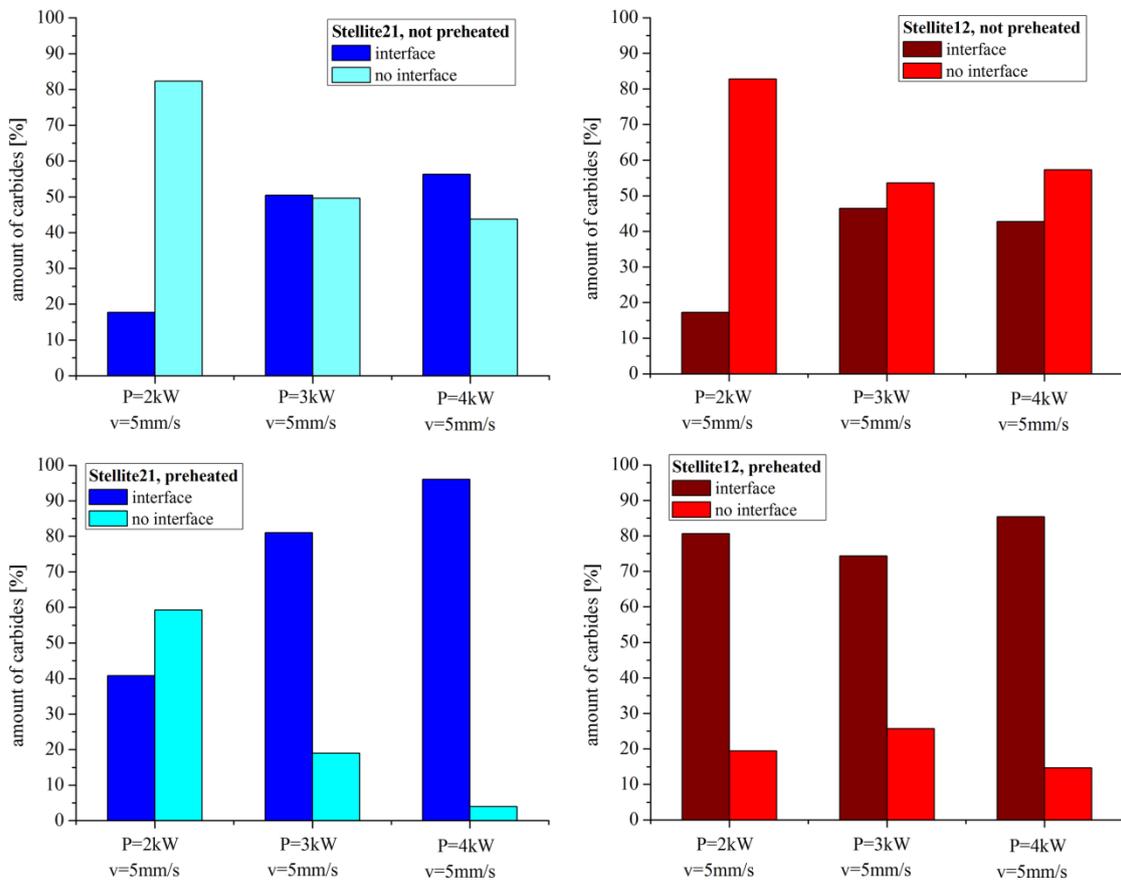


*Figure 3.71. Percentage of carbides with and without the interfacial microstructural constituent according to their processing condition and to the material.*

The microstructure of interface is influenced by the laser power: when the laser power increases, the number of carbides with a clean interface decreases. The effect is more pronounced on passing from 2 kW to 3 kW than from 3 kW to 4 kW.

Preheating enhances the formation of the interfacial microstructural constituent, as confirmed by Figure 3.72, where the average of the results of all the samples produced in the two conditions (preheated and not ) are reported.
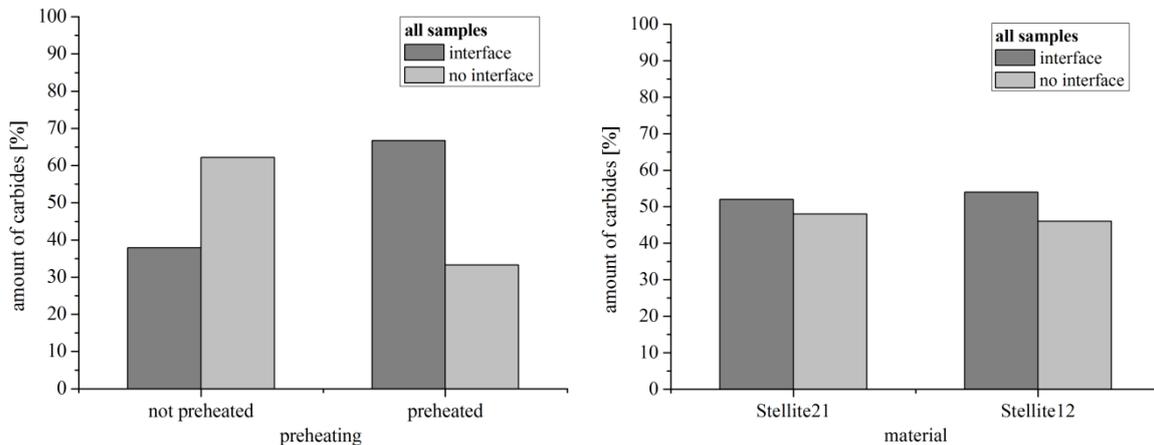


*Figure 3.72. Percentage of carbides with and without the interfacial microstructural constituent according to their preheating conditions (left) and to the different base materials (right) for all the samples measured.*

As it can be seen, when the substrate is not preheated, only the 38% of the carbides analysed present the shell. This trend is inverted when the substrate is preheated: in this case, the shell is shown by the 67% of the analysed carbides. The different chemical composition of the two materials used as a matrix does not seem to systematically affect the formation of interfacial constituent, as confirmed in Figure 3.72, where the average values of all the samples produced with Stellite21 and Stellite12 are reported.

The presence of the shell surrounding either completely or partially the WC particles, may be significant of the capability of the liquid to homogenize the W and C content in the matrix. Such a homogenization is mostly provided by the convective motions activated by the viscosity gradients in the liquid, due to the temperature gradients. These gradients are expected to decrease with the laser power and with preheating of the substrate, and this may justify the less amount of particles surrounded, more or less homogeneously, by the shell on increasing the laser power and on overheating the substrate. The observation that the chemical composition of the cobalt alloy of the matrix does not influence the interface morphology further confirm this conclusion, since the redistribution of C and W atoms released by dissolution occurs mostly in the liquid state than in solid state after solidification.

Dissolution of tungsten carbides is supposed to influence hardness of the coating in two different ways: with the increase in dissolution, hardness should decrease because the $WC/W_2C$ volume fraction decreases; at the same time, the average microhardness of the alloy matrix is expected to increase because of the dissolution of tungsten and carbon.

Moreover, hardness is expected to be influenced by dilution, due to the dissolution of iron and carbon from the substrate.

Hardness of the coating and microhardness of the matrix are reported in Figure 3.73 as a function of dilution.
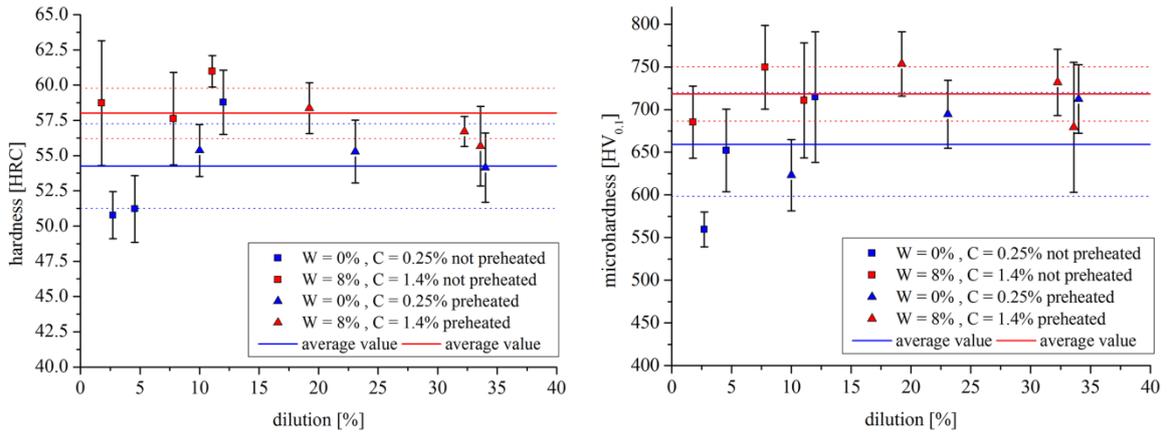
*Figure 3.73. Rockwell C Hardness (left) and matrix $HV_{0.1}$ microhardness (right) as a function of dilution.*

Even in case of deep contamination from the substrate, hardness and microhardness measurements do not show any specific trend with dilution. Dilution does not influence the final microhardness of the matrix and, consequently, it does not influence the hardness of the coating.

Figure 3.74 shows the effect of dissolution of WC particles on hardness and microhardness.
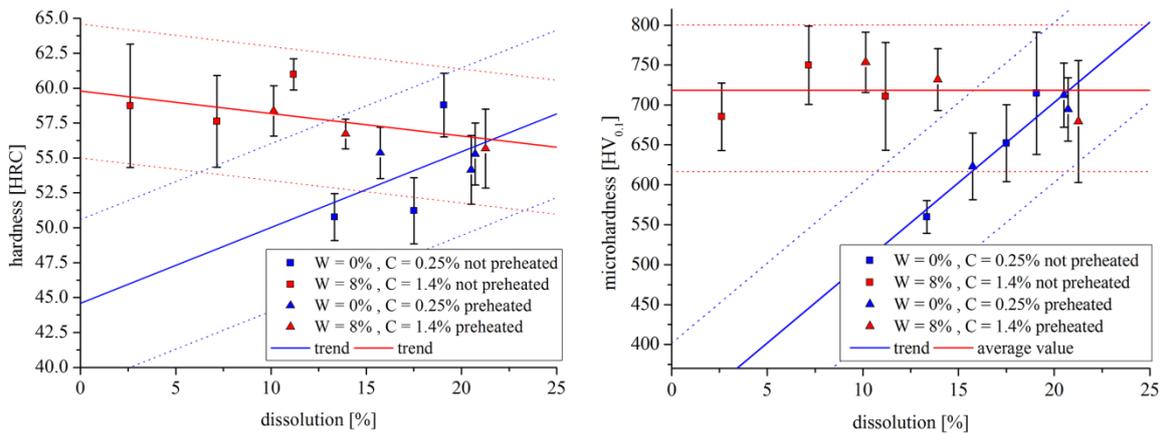


*Figure 3.74. Rockwell C Hardness (left) and matrix $HV_{0.1}$ microhardness (right)as a function of carbides dissolution.*

When dissolution of tungsten carbides takes place into Stellite21, tungsten and carbon dissolve into the alloy matrix and cause an increase in the microhardness, as shown in Figure 3.74. In Stellite12 , where the total amount of dissolution is lower and tungsten and carbon are already present, the dissolution of these two element into the matrix has no effect on the matrix microhardness.

The effect on the matrix microhardness is confirmed also by the hardness tests. Hardness of the coatings made with Stellite21 tends to increase with the increase in dissolution: the depletion in the reinforcement particles volume is balanced by the large enrichment of the alloy matrix by tungsten and carbon. On the other hand, the hardness of the coatings made with Stellite12 slightly decreases when carbides dissolution increases: carbides depletion is not associated with an increase in the microhardness of the matrix alloy, and the only result is the decrease in the coatings hardness.

# Conclusions

The present PhD work, developed in the frame of a cooperation with Höganäs AB, regarded the study of a high power laser cladding process and a preliminary characterization of the coatings produced with this technique using different metallic powders.

At first, the influence of the powder material and the processing conditions on geometrical features and dilution of the clads has been investigated.

Then, the main physical phenomena involved in laser cladding process have been identified and evaluated quantitatively, and an energetic balance of the process has been proposed. The effects of the processing parameters and the cladding material have been discussed.

Lastly, a preliminary study of the coating properties has been performed, with a particular focus on the effect of dilution and, in case of MMC, of carbide dissolution.

The results can be briefly summarized as follows.

Geometry of the clad depends on the main processing parameters and on the cladding material, and models to estimate clad height and width have been obtained. Clad height has a complex correlation with the emerging cross-sectional area of the clad: it is strongly influenced by the feeding rate, the scanning speed, the material density and, slightly, by the laser power through the material efficiency. On the other hand, clad width is correlated with the laser power and the scanning speed. Through these models, clad aspect ratio can be estimated with a good approximation in the range between 5 and 20, within which typical laser cladding coatings are produced.

The analytical correlation between processing parameters and dilution has been obtained. Dilution is mainly influenced by the laser power and the feeding rate, while the effect of scan speed is less pronounced. In specific, dilution increases with the increase in the laser power and the scan speed and with the decrease in the feeding rate. These conclusions are in good agreement with the results of the energetic balance, where the dependence of dilution on the energy and powder available by the system is confirmed: as demonstrated, dilution can be represented by the energy partitioning between the powder and the substrate.

The effects on the models of geometry and dilution of substrate material and preheating have been discussed. Substrate preheating can be seen like a surplus of energy given to the cladding system, and it can be thus represented by an increased laser power. In the specific processing conditions utilized, substrate preheating of 400°C results to be equivalent to an increase in the laser power of 0.67 kW. Substrate material, on the opposite, does not modify the clad geometry, but it heavily affects dilution:

in particular, the thermophysical properties of the substrate influence the energy partitioning between powder and substrate and, as stated before, they consequently affect dilution.

The investigation on the energy redistribution in the laser cladding process confirmed the low energetic efficiency of the process, which is mainly due to the high reflectivity of the liquid metal. No significant variations have been observed due to the powder materials.

The angle of incidence, expressed through clad and melt pool geometry, has been identified as a useful parameter to describe the energy partitioning of the process. By varying the angle of incidence, the energy absorbed by the powder/substrate system does not change, but the energetic distribution of the process is drastically altered: for low angles of incidence, generally thinner clads with high dilution are generated, and most of the absorbed energy is lost by conduction through the substrate. On increasing the angle of incidence, thicker clads are produced with the positive effects of both a lower dilution and a higher energetic efficiency.

Dilution may have detrimental effects on the properties of the coatings.

Dilution in clads produced with the Stellite1 powder leads to a decrease in hardness and microhardness, which is caused by the microstructural evolution of the Co-based alloy. On increasing dilution, cellular to dendritic transition is evidenced. This transition, explained by the lowering of the $G/R$ ratio and the different chemical composition of the alloy, limits the formation of the eutectic constituent, within which carbides are localized, and consequently leads to the decrease in the coating hardness.

In the clads produced with Inconel 625 powder, on increasing dilution, microstructural evolution is evidenced together with the decrease in clad microhardness. In clads with limited dilution, dendritic structure is present with interdendritic regions showing the formation of niobium carbides with blocky morphology; on increasing dilution, the formation of both the Laves phases and the NbC having lamellar eutectic-type morphology is promoted. In addition, dilution has a negative effect on the thermal oxidation behaviour of the alloy. The oxidation rate increases on increasing dilution, and catastrophic oxidation has been observed in the worst processing conditions, i.e. high dilution and high temperature. Even with limited dilution, the relative decrease in the oxidation rate between the first and the second stage, which basically expresses the attenuation of the oxidation behaviour during the test, gets worse.

A clear correlation between microhardness and dilution is revealed also in the clads produced with the NiBSi alloy. Again, this behaviour is caused by the microstructure of the alloy. On increasing dilution, microstructure evolves in two different ways: microstructure becomes more dendritic, since iron dilution modifies the chemical composition of the NiBSi alloy, which is expected to move far from eutectic points, thus promoting proeutectic solidification. Moreover, with the increase in dilution, eutectic morphology evolves towards the formation of the γ-nickel-boride eutectic and a silicon-rich precipitate at the expense of the nickel-boride nickel-silicide eutectic, that tends to disappear.

When grey cast iron is used as a substrate, the NiBSi alloy shows the same microstructural change; in addition, on increasing dilution, the presence of the graphite is evidenced. The morphology of this graphite seems to change from spheroidal to vermicular and flake on decreasing the $G/R$ ratio, i.e. on increasing dilution.

In the MMC coatings produced with a mixture of either Stellite12 or Stellite 21 powder and tungsten carbides, carbides dissolution occurs during laser cladding and influences the final properties of the coatings. Dissolution is largely influenced by the processing conditions investigated. Dissolution gets higher with the increase in the laser power and when substrate is preheated, mainly because of the increase in temperature of the melt pool, which enhances dissolution phenomena. Chemical composition of the Stellite base powder also influences dissolution: a lower content of tungsten and carbon favours the dissolution of the tungsten carbides.

In the matrix where no tungsten and 0.25% of carbon are present, carbides dissolution leads to an increase in the microhardness, which prevails over the decrease in the WC content, thus leading to an increase in the hardness of the coating. On the opposite, matrix microhardness of the stellite rich in tungsten and carbon does not get any benefit from carbides dissolution: as a consequence, hardness of the coating slightly decreases due to the decrease of the WC content.

# Appendix 1

# **Carbides dissolution**

Dissolution of carbides was evaluated in the MMC coatings in different ways. Image analysis was used to measure the ratio between the area of the carbides and the area of the metal matrix in the cross-sectional area of the bead. For every bead, three cross-sectional areas were measured.

Percentage of dissolution ($d$) was evaluated using the equation

$$d = V_{WC} - \left(100 \cdot \frac{A_C}{A_N}\right) \qquad \text{(A.1)}$$

where $V_{WC}$ represents the volumetric percentage of carbides in the coating, equal to 35, $A_C$ is the area of the carbides in the cross-sectional area of the bead and $A_N$ is the part of the cross-sectional area that emerges from the original surface of the clad (Figure A.1).
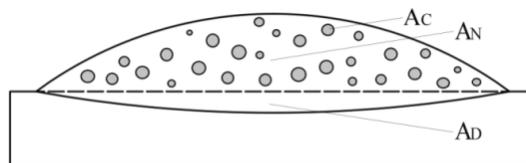


*Figure A.1. Schematic drawing of the clad cross-sectional area: emerging cross-sectional area ($A_N$), submerged cross-sectional area ($A_D$) and area of the carbides in the cross-sectional area ($A_C$).*

As shown by a typical microstructure of the coating, a microstructural constituents may be observed at the interface between the matrix and some of the carbide particles. Carbides were then classified according to the presence of this particular constituent as shown in Figure A.2: for instance, in carbides (b) the interface constituent is absent, while in carbides (a) the interface constituent is present. The relative amounts of these morphologies at the interface were measured by analysing five images containing about 80 carbides each for every clad.
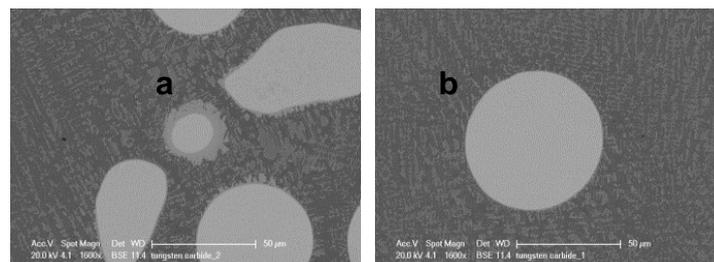


*Figure A.2. Classifications of the carbides according to the presence of the interface constituent: tungsten carbide with (a) and without (b) interface constituent.*

# Appendix 2
# Dilution

Two different methods have been proposed and compared to determine dilution. In the first method ("chemical dilution"), dilution is evaluated by analysing the iron concentration profile with EDXS analysis on the cross section of the clad perpendicular to the laser scan direction. EDXS analysis is not appropriate to get a quantitative measure of carbon content; therefore dilution was investigated by considering iron contamination. Small frame (10 μm x 13 μm) analyses were collected on the cross sections along the clad thickness, from the interface up to the external surface.

Since the iron concentration has a gradient along the clad thickness, the cross-sectional area of the clad was divided into small rectangles having constant height of 10 μm and variable base, up to a distance from interface corresponding to the gradient length, as shown in Figure A.3.
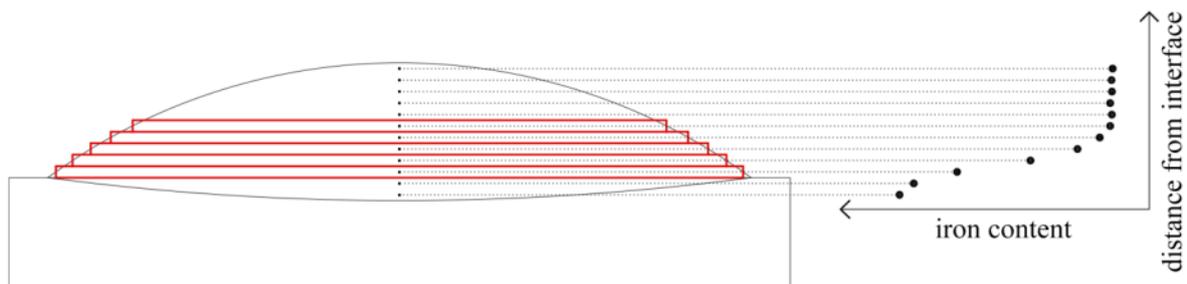


*Figure A.3. Schematic representation of the cross-sectional areas used to define the chemical dilution.*

Under the assumption of a constant chemical composition along the base of the clad (verified by some analyses), each rectangle has the mean iron concentration measured by EDXS. The remaining part of the cross-sectional area where the iron concentration is constant ($A_r$) was measured by Image Analysis. Image Analysis was also used to measure the diluted part of the cross-sectional area ($A_D$), where iron content is almost constant.

Chemical dilution, expressed as the average iron concentration in the clad, is thus given by equation

$$Fe_C = \frac{\sum_i^n A_i \cdot Fe_i}{A} = \frac{\sum_i^{n-1}[(w_{i-1} - 2 \cdot \delta_i) \cdot h \cdot Fe_i] + A_r \cdot Fe_r + A_D \cdot Fe_D}{A} \qquad \text{(A.2)}$$

where $A_i$ is the area of the i-rectangle having $Fe_i$ iron concentration measured with EDXS, $A$ is the cross-sectional area of the clad, $h$ is the rectangles height, $w_i$ is the width of the i-rectangle, $\delta_i$ is the width decrement for every i-rectangle ($\delta_i = h \cdot cotg\alpha$ where $\alpha$ is the contact angle), $A_r$ is the remaining part of the cross-sectional area where the chemical composition is constant and equal to $Fe_r$ and $A_D$ is the diluted part of the cross-sectional area where the chemical composition is equal to $Fe_D$.

In the second method ("geometrical dilution"), the average iron concentration of the clad was calculated with equation

$$Fe_G = \frac{A_N \cdot Fe_{powder} + A_D \cdot Fe_{substrate}}{A} \qquad (A.3)$$

where $A_N$ is the part of the cross-sectional area emerging from the original surface of the plate (related to the molten powder) and $A_D$ is the submerged part of the cross-sectional area (related to the molten substrate), as shown in Figure A.4; $A$ is the cross-sectional area of the clad, $Fe_{powder}$ and $Fe_{substrate}$ are the iron concentration of the powder and of the substrate, respectively.
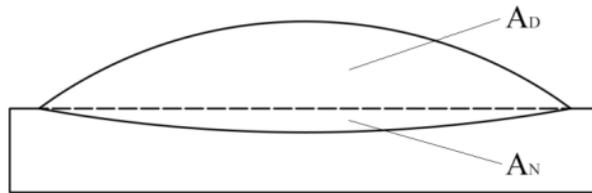


*Figure A.4. Schematic representation of $A_N$ (part of the cross-sectional area emerging from the original surface of the plate) and $A_D$ (submerged part of the cross-sectional area).*

To compare the two methods, the Stellite1 as cladding material and the mild steel as substrate have been used.
The EDXS iron concentration profiles in some of the clads produced in the different conditions are reported in Figure A.5; the horizontal line at 0.93% Fe represents the iron concentration of the starting powder, as measured by the same technique.
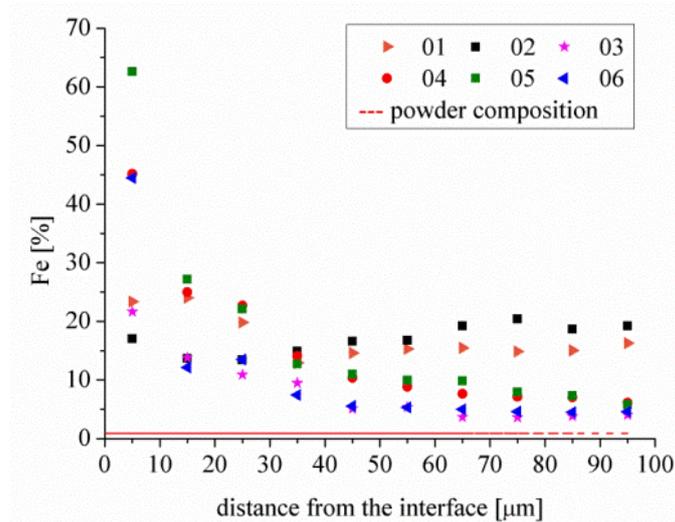


*Figure A.5. EDXS iron concentration profiles of six clad investigated in different processing conditions: laser power ranging from 3 to 4 kW, scan speed ranging from 3 to 4 mm/s, feeding rate ranging from 0.5 to 0.6 g/s.*

The iron concentration of the clads is higher than that of the starting powder along the whole of their thickness. A sharp gradient in the first 30-40 μm is a common feature of all the clads, and demonstrates that even in presence of convective motions within the liquid pool [159] a homogeneous distribution of iron is not completely attained. Beyond the first 100 μm, a steady value is reached.

Geometrical ($Fe_G$) and chemical ($Fe_C$) dilution, calculated using equations (A.1) and (A.2), respectively, are plotted in Figure A.6. The difference between the results of the two methods is very small (less than 0.5%).
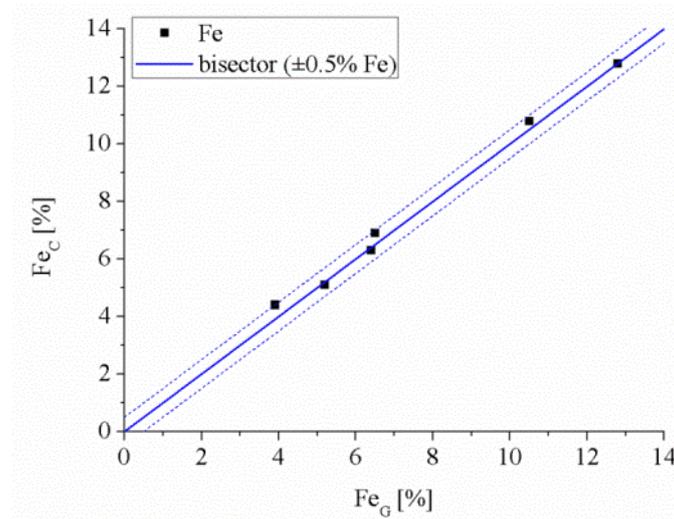


*Figure A.6. Average iron concentration calculated with the chemical method vs. average iron concentration calculated with the geometrical method.*

The results are equivalent and the geometrical method is therefore validated through the results of the chemical analysis. The geometrical method is easier, since it's based on a simple metallographic investigation of the cross section of the clads. On the other hand, the chemical method is much more time consuming but it gives a more detailed information on dilution, highlighting the concentration profile along the clad height, which is definitely inhomogeneous. Both methods deliver a mean iron concentration which is not truly representative, due to the gradient: they underestimate the iron concentration close to interface and slightly overestimate that one in the upper part of the clad. Since in practical applications it is the external part of the clad which interacts with the environment (in case of corrosion and/or oxidation resisting clads) and any other material (in case of wear resisting clads), the slight overestimation provided by the mean value of dilution is conservative and therefore the simple geometrical method, in absence of any special requirements, may be preferred to the chemical one.

# Appendix 3

# Absorption coefficient of the liquid metal $\beta_s$

The aim of this in-situ calorimetric experiment is to determine the absorption coefficient $\beta_s$ of the liquid metal material when irradiated by a laser light. The sample is used as a calorimeter, and the determination of the energy absorbed is obtained through its temperature rise. This is of course possible due to the high thermal conductivity of metallic plate relative to their external cooling by exchange with the atmosphere. Thus, shortly after the laser has passed over the specimen, the absorbed energy conducted from the laser-heated zone is redistributed to give a uniform temperature in the plate. Once this condition has been achieved, the variation of temperature in the isothermal sample is assumed to follow a convective cooling condition described by the following equation

$$h \cdot S \cdot [T(t) - T_a] = -m \cdot c_p \cdot \frac{dT(t)}{dt} \qquad \text{(A.4)}$$

where $h$ is the heat-transfer coefficient, $S$ is the thermal-exchange surface area, $T(t)$ is the temperature of the sample, $T_a$ is the ambient temperature, $m$ is the mass of the sample and $c_p$ is the heat capacity of the sample. The heat capacity is assumed to be linearly proportional to temperature according to the equation

$$c_p = a \cdot T + b \qquad \text{(A.5)}$$

where $a$ and $b$ are two constants, and the temperature dependence of the heat-transfer coefficient h is approximated by

$$h = B \cdot [T(t) - T_a]^{\frac{1}{e}} \qquad \text{(A.6)}$$

where $B$ and $e$ are two constants, which depend on the cooling condition.
Extrapolating the cooling curve back to the time $t_0$ when the laser was switched off, it is possible to obtain the temperature $T(t_0)$ the sample would have reached if all the absorbed energy had been evenly distributed throughout the volume of the sample, assuming negligible the heat losses during the cladding period.
This temperature leads to the determination of the global absorption $\beta_g$ through the formula

$$\beta_g = \frac{m \cdot c_p \cdot [T(t) - T_a]}{P \cdot \tau} \qquad \text{(A.7)}$$

where $P$ is the laser power and $\tau$ represents the interaction time of the laser with the specimen.

Global absorption $\beta_g$ has been measured for the four materials used in the energetic model (NiBSi, 316L, In625 and Stellite1) cladded on the mild steel substrate in five different processing conditions. The experimental setup is shown in Figure A.7.
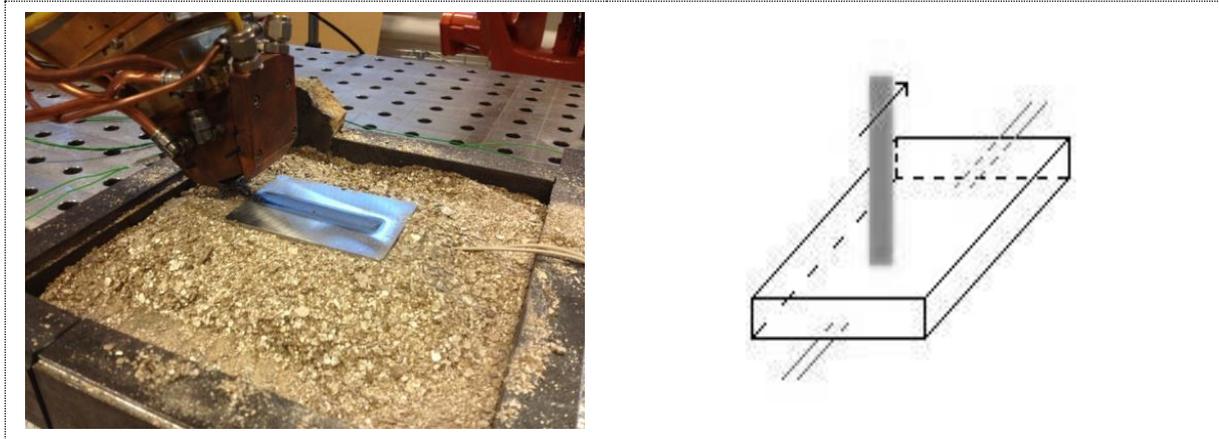


*Figure A.7. Experimental setup of the calorimetric experiment.*

For the temperature measurements, two S-type thermocouples have been spotwelded to the lower surface of the sample in a central position, as shown in Figure A.7. Moreover, five of the six external surfaces of the sample have been surrounded by vermiculite powder in order to have good thermal isolation in all direction except for the upper surface, where convective cooling was taking place.

Thermocouples data have been analyzed with Origin in order to obtain the best fitting and, in turn, the best value of $T(t_0)$. A regression curve was calculated between the time $t_1$ and $t_2$ in order to fit the two measured cooling curves, using the equation (A.4) with the parameters $e$ and $B$ as variables. The time $t_1$ was defined as the time at which the sample had cooled to a nearly isothermal state (determined as a temperature difference between the two thermocouples of less than 1°C), and the time $t_2$ was defined as the time at which the sample was nearly at the equilibrium (determined as a temperature difference between the two thermocouples and the ambient of less than 3°C).

In Figure A.8 the temperatures recorded by the two thermocouples in one of the runs are reported.
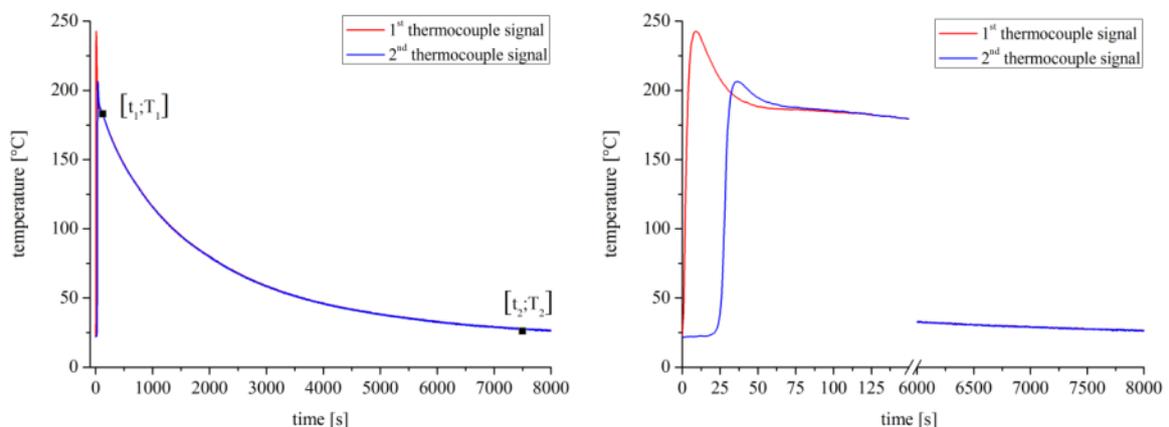


*Figure A.8. Temperatures recorded by the two thermocouples in one of the run.*

The red curve (1st thermocouple signal) is the record of the thermocouple welded to the plate side where the laser scan starts, while the blue one (2nd thermocouple signal) refers to the side where the laser scan ends. When the laser is scanning, both curves show a peak in the temperature signal.

Then, the temperature starts to decrease according to the convective cooling condition. The points corresponding to the previously defined values of $t_1$ and $t_2$ are shown, and between these two points the signals are superimposing.

On the original differential equation (A.4), the method of separation of variables has been applied to get an equation that could be used by the Origin program.

The regression curve has been calculated between the interval $\{t_1;t_2\}$ and the values of $B$ and $e$ giving the best fit (in terms of the regression coefficient) were determined for each experiment.

One of the resulting regression curves has been plotted with the thermocouples curves (Figure A.9), and the value of $T(t_0)$ and of the global absorption $\beta_g$ has been obtained and reported in Table A.1 together with the other parameters used.
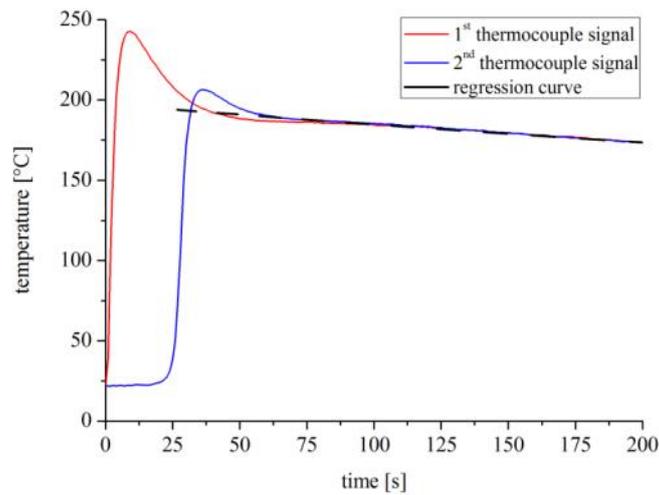


*Figure A.9. Temperatures recorded by the two thermocouples in one of the run and regression curve.*

*Table A.1. Data obtained in the calorimetric experiment.*

| material | $\theta_{in}$ [degree] | $T_0$ [°C] | e | $B \cdot 10^4$ | $\beta_g$ |
|----------|------------------------|-------------|---|----------------|-----------|
| 316L | 34.4 | $150 \pm 2$ | $2.83 \pm 0.39$ | $9.6 \pm 2.8$ | $0.55 \pm 0.01$ |
| | 47.0 | $374 \pm 21$ | $2.46 \pm 0.12$ | $6.3 \pm 0.4$ | $0.44 \pm 0.03$ |
| | 63.5 | $458 \pm 30$ | $2.33 \pm 0.19$ | $5.6 \pm 1.1$ | $0.43 \pm 0.04$ |
| | 42.5 | $287 \pm 12$ | $1.99 \pm 0.38$ | $4.7 \pm 1.6$ | $0.47 \pm 0.02$ |
| | 54.6 | $413 \pm 25$ | $2.04 \pm 0.33$ | $4.5 \pm 1.7$ | $0.37 \pm 0.03$ |
| NiBSi | 35.1 | $139 \pm 6$ | $2.57 \pm 0.30$ | $9.3 \pm 2.6$ | $0.50 \pm 0.03$ |
| | 46.0 | $362 \pm 19$ | $2.52 \pm 0.22$ | $6.7 \pm 1.2$ | $0.42 \pm 0.03$ |
| | 54.6 | $385 \pm 13$ | $2.17 \pm 0.34$ | $5.3 \pm 2.0$ | $0.34 \pm 0.01$ |
| | 39.9 | $270 \pm 3$ | $2.44 \pm 0.21$ | $6.8 \pm 1.2$ | $0.43 \pm 0.01$ |
| | 59.8 | $451 \pm 14$ | $2.22 \pm 0.24$ | $5.3 \pm 1.8$ | $0.43 \pm 0.02$ |
| In625 | 34.4 | $147 \pm 7$ | $2.01 \pm 0.25$ | $6.7 \pm 2.5$ | $0.53 \pm 0.03$ |
| | 38.9 | $204 \pm 12$ | $2.05 \pm 0.15$ | $6.1 \pm 1.2$ | $0.41 \pm 0.03$ |
| | 44.9 | $349 \pm 15$ | $1.89 \pm 0.11$ | $4.4 \pm 0.8$ | $0.40 \pm 0.02$ |
| | 50.9 | $375 \pm 22$ | $1.88 \pm 0.13$ | $4.3 \pm 0.9$ | $0.45 \pm 0.03$ |
| | 60.7 | $454 \pm 39$ | $1.83 \pm 0.13$ | $3.8 \pm 1.1$ | $0.43 \pm 0.05$ |
| Stellite1 | 34.3 | $155 \pm 2$ | $1.95 \pm 0.09$ | $5.2 \pm 1.0$ | $0.56 \pm 0.01$ |
| | 42.3 | $289 \pm 10$ | $1.87 \pm 0.03$ | $4.4 \pm 0.3$ | $0.47 \pm 0.02$ |
| | 47.6 | $386 \pm 2$ | $1.77 \pm 0.10$ | $3.5 \pm 0.6$ | $0.45 \pm 0.01$ |
| | 53.7 | $462 \pm 13$ | $1.77 \pm 0.10$ | $3.3 \pm 0.7$ | $0.43 \pm 0.01$ |
| | 61.8 | $479 \pm 18$ | $1.80 \pm 0.11$ | $3.5 \pm 0.7$ | $0.46 \pm 0.02$ |

The values of $e$ and $B$ that optimize the fitting are similar for all the experiments and the regression coefficients obtained are all of them higher than 0.98. This proves the quality of the fitting method.

The measured value $\beta_g$ represents the fraction of power (or energy) which is absorbed by the cladding system with respect to the input power (or energy), and it can be represented by

$$\beta_g = \frac{P_A}{P} = \frac{P_{abs,mp} + P_{abs,prI} + P_{abs,prII}}{P} \qquad \text{(A.8)}$$

using the definition of $P_A$ (power absorbed by the cladding system) given in Chapter 3.6.1.

To obtain the absorption coefficient of the liquid metal material when irradiated by a laser light ($\beta_s$), equation (A.8) has been rewritten in the following form

$$\beta_S = \frac{\beta_g \cdot P - \eta \cdot \beta_p \cdot P_{att} - \eta \cdot \beta_p \cdot (P - P_{att}) \cdot \frac{P_{att}}{P}}{(P - P_{att}) \cdot \left[1 - \eta \cdot \beta_p \cdot \frac{P_{att}}{P}\right]} \qquad \text{(A.9)}$$

The absorption of the liquid metal material when irradiated by a laser light depends on the laser light (polarization and wavelength), the optical properties of the coating material and the angle between the laser beam and the normal to the melt pool surface (i.e. angle of incidence). For a non-polarized beam, the equation that can be used to correlate $\beta_s$ to these factors is Fresnel's equation

$$\beta_S = \frac{2 \cdot n \cdot \cos\theta_{in}}{(n \cdot \cos\theta_{in} + 1)^2 + (k \cdot \cos\theta_{in})^2} + \frac{2 \cdot n \cdot \cos\theta_{in}}{(n + \cos\theta_{in})^2 + k^2} \qquad \text{(A.10)}$$

where $n$ and $k$ are the refraction index and the extinction coefficient respectively, both optical constants of the cladding material, and $\theta_{in}$ is the angle of incidence.

For a single-bead clad, the angle of incidence can be simply determined from the height of the clad $H$ and the length of the melt pool $L$. However, in the particular configuration used the laser beam is not perpendicular to the substrate surface. Indeed, the laser beam is inclined of an angle $\alpha_L$ (equal to 28°) with the surface of the substrate, as shown in Figure A.10.
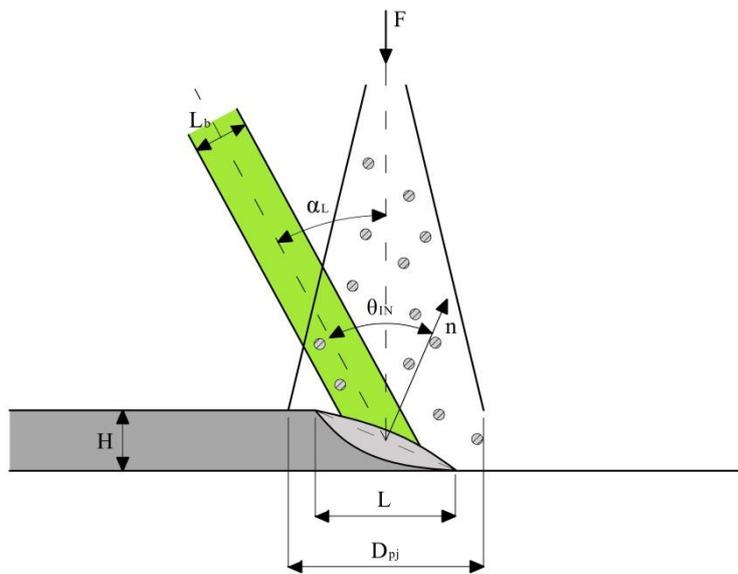


*Figure A.10. Schematic of the particular setup used for this laser cladding process.*

For this reason, the equation used to estimate the angle of incidence is

$$\theta_{in} = \alpha_L + \tan^{-1} \frac{H}{L} \qquad \text{(A.11)}$$

The values of absorption $\beta_s$ for the powder materials studied have been calculated for five clads having different incidence's angles. Results are plotted together with Fresnel's equations, where the optical constants $n$ and $k$ for the different materials have been obtained by minimization of residuals (Figure A.11).
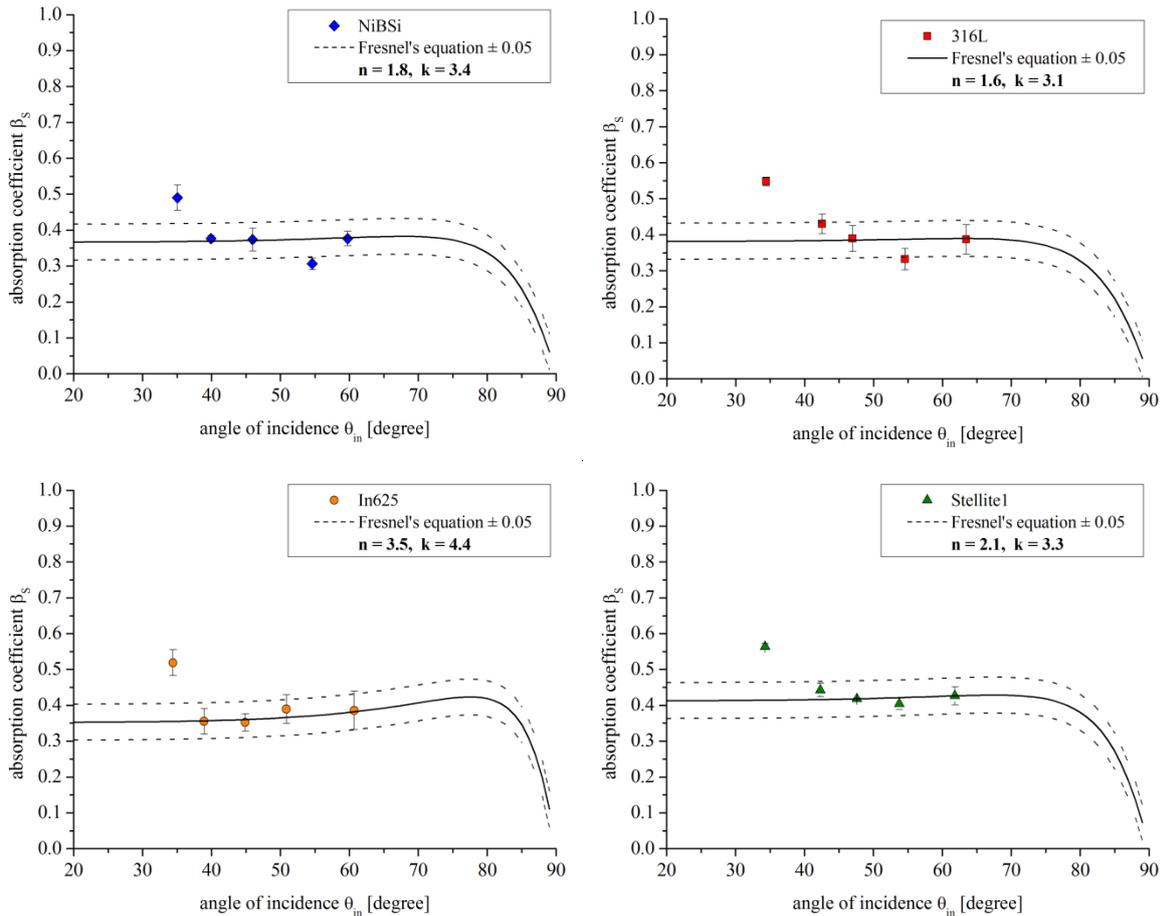


*Figure A.11. Measured values of absorption $\beta_s$ for the four materials together with the estimated Fresnel's curves.*

As supposed, for a non-polarized beam absorption is not influenced significantly by the angle of incidence in the range studied. Once the geometry of the clad is known, equation (A.11) calculated with the obtained values of $n$ and $k$ allows the calculation of the coefficient $\beta_s$.

To prove the quality of the extrapolated values of n and k, these values have been compared with the values of refraction index and extinction coefficient reported in literature for the pure elements, at room temperature, at the wavelength of 808 nm (Table A.2)

*Table A.2. Comparison between the values of n and k reported in literature for Ni, Co and Fe (room temperature, wavelength of 808 nm) and estimated for the four different cladding materials [160].*

| material | n | k |
|---|---|---|
| **estimated** | | |
| NiBSi | 1.8 | 3.4 |
| 316L | 1.6 | 3.1 |
| In625 | 3.5 | 4.4 |
| Stellite1 | 2.1 | 3.3 |
| **literature** | | |
| Ni | 2.2 | 4.9 |
| Co | 2.5 | 4.8 |
| Fe | 2.9 | 3.4 |

Some limited differences are revealed between the estimated and the literature values. However, these small differences can be considered acceptable due to the contrasting conditions of the measurements performed (alloys in liquid state at a high temperature).

# Appendix 4
# Normal spectral absorbance

The schematic diagram of the experimental set-up used for measuring the normal spectral absorbance of powders is reported in Figure A.12.
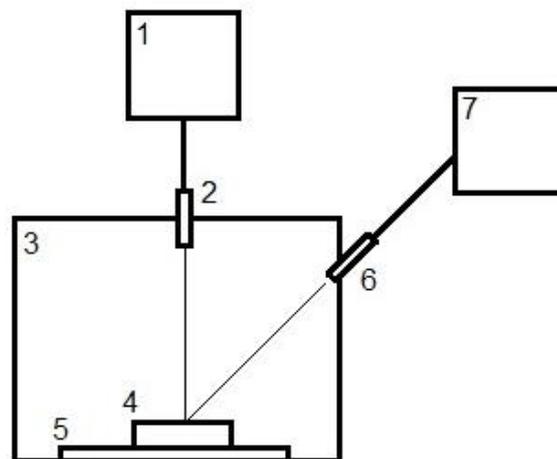


*Figure A.12. Experimental setup of the experiment.*

Radiation is created by DH2000-S Deuterium Tungsten Halogen Light Sources (Figure A.12,1), which combines the continuous spectrum of deuterium and tungsten halogen light sources. Light is carried over a silica fibre optic bundle (Figure A.12,2) into an integrating sphere (Figure A.12,3), where it couples the loose powder surface (Figure A.12,4) deposited on a black substrate (Figure A.12,5) located at the centre of the integrating sphere. The layer of powder is assumed to be thick enough that no detectable light passes through it. The radiation, which is diffusively reflected by the powder, reaches the photo-receiver (Figure A.12,6). The diffused light is collected by another silica fibre and sent to an Ocean Optics USB4000 optical spectrometer (Figure A.12,7), which disperses and records the full reflected spectrum within an integration time of 10 seconds. The calibration was made using a specimen of barium sulphate powder ($BaSO_4$) with known diffuse reflectance ($\approx 1$).

Absorbance has been calculated according to the formula $A = 1 - R$, where $R$ is the reflectance of a material and is defined as the ratio of the reflected radiation to the incident radiation. For every material, the measurements of the whole spectra between 400 nm and 900 nm has been made. For the measurements in the visible region, the halogen lamp has been utilized.

The measurements of the spectral absorbance of the investigated powders (NiBSi, 316L, In625 and Stellite1) are reported in Figure A.13.
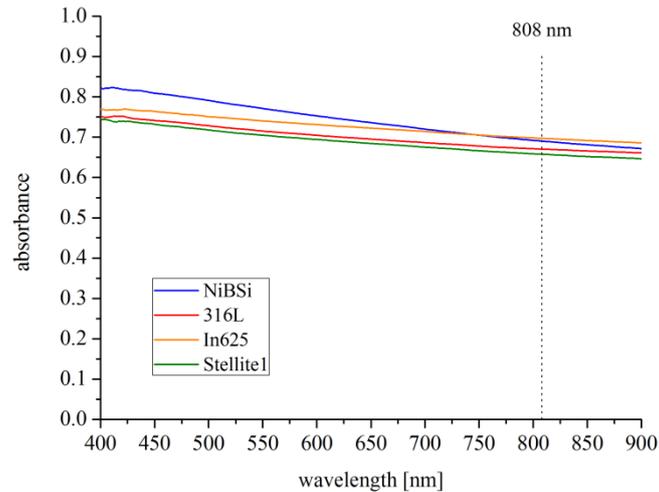
*Figure A.13. Spectral absorbance in the visible region for the different powders.*

As it can be seen, there is basically no difference between the absorbance spectra of the four materials. It has to be remembered that the laser used to produce the clads is a high power diode laser HighLight 4000L, which is operating at the wavelength of 808 nm. At that particular wavelength, the values of the absorbance of the different powder materials are included in the range 0.66 – 0.70%. Values of the measured absorbance $\beta_p$ are reported in Table A.3.

*Table A.3. Absorbance $\beta_p$ of the four powders at the wavelength of 808 nm.*

| material | $\beta_p$ |
|----------|-----------|
| NiBSi | 0.69 |
| 316L | 0.67 |
| In625 | 0.70 |
| Stellite1 | 0.66 |

# Appendix 5

# Trial and error method

Several different approaches can be used to investigate the influence of the processing parameters and their mutual interactions on the characteristics of the clad. Physico-computational models generally use a complex set of coupled equations, since taking into account different physical phenomena occurring in the laser cladding process, such as mass and heat transfer, fluid flow and phase transformation, is required. On the other hand, empirical equations obtained from statistical analysis of experimental data allow to simply and accurately correlate the processing parameters with the clad properties.

In this work, correlation between an individual characteristic of the clad and a combined process parameter has been found using the "trial and error" method, which is a simple approach to estimate the importance of a single laser cladding parameter and/or their mutual interactions.

The combined process parameter $\Phi_i$ has been defined as a combination of the three main processing parameters ($P$, $V$ and $F$) raised to opportune exponents ($x$, $y$ and $z$ respectively), as shown in equation

$$\Phi_i = P^x \cdot V^y \cdot F^z \qquad \text{(A.12)}$$

and the mathematical formula used to describe the correlation between the desired $i$-quantity and the processing parameters have the following form

$$Q_i = A_i + B_i \cdot \Phi_i \qquad \text{(A.13)}$$

where $Q_i$ is the investigated quantity and $A_i$ and $B_i$ are fitting constants.

The best fit in terms of regression coefficient for equation (A.13) has been calculated by varying the exponents $x$, $y$ and $z$ between -5 and 5 with an interval of 0.5 while, if not differently specified, no limitations have been set for the fitting constants $A_i$ and $B_i$.

# Appendix 6
# Melt pool temperature

The temperature of the melt pool has been estimated for the clads produced with four powders (NiBSi, 316L, In625 and Stellite1) on the mild steel using the equation proposed by Pinkerton and Li [130] and modified by the author

$$T_{mp} = \frac{P_A}{4 \cdot \pi \cdot k(T) \cdot D_{eq}} + T_S \qquad \text{(A.14)}$$

where $P_A$ is the power absorbed by the cladding system, $k(T)$ is the thermal conductivity of the cladding material, which is function of the temperature, $D_{eq}$ is the equivalent diameter of the melt pool and $T_s$ is the solidus temperature of the cladding material. This equation is obtained by approximating the heated pool region as a sphere with uniform heat generation and with one half of its surface at the solidus temperature, then by adapting the standard one-dimensional steady state solution to allow for surface conduction only over half of the surface.

The equivalent diameter of the melt pool has been calculated using equation (A.15) as the diameter of the melt pool assuming it to be circular

$$D_{eq} = \sqrt{\frac{4 \cdot A_{mp}}{\pi}} \qquad \text{(A.15)}$$

The solidus temperature of the different materials investigated has been found in literature [143,144]. These values are reported in Table A.4.

*Table A.4. Solidus temperature of the four materials.*

| material | $T_S$ [°C] |
|----------|------------|
| NiBSi    | 1040       |
| 316L     | 1375       |
| In625    | 1290       |
| Stellite1 | 1280      |

The thermal conductivity has been estimated through the work of Nishi et al. [161], who measured the values of thermal conductivity of molten iron, cobalt, and nickel and their variation with $T$ in a defined temperature range with the laser flash method. These equations and the respective measurement ranges are

$$k_{Fe} = 2.15 \cdot 10^{-2} \cdot (T - 1818) + 33.3 \qquad 1818 \le T \le 1868 \qquad \text{(A.16)}$$

$$k_{Co} = 2.79 \cdot 10^{-2} \cdot (T - 1768) + 30.4 \qquad 1768 \le T \le 1838 \qquad \text{(A.17)}$$

$$k_{Ni} = 2.30 \cdot 10^{-2} \cdot (T - 1728) + 53.0 \qquad 1728 \le T \le 1908 \qquad \text{(A.18)}$$

where $T$ represents the temperature measured in K.

For this work, the equations (A.16), (A.17) and (A.18) are assumed to be valid not only in the measured temperature region, but also for higher or lower temperatures, and the same linear temperature dependence in supposed.

The thermal conductivity of molten iron has been used for the calculation of the Fe-based alloy (316L), the thermal conductivity of molten cobalt has been used for the calculation of the Co-based alloy (Stellite1) and the thermal conductivity of molten nickel has been used for the calculation of both the Ni-based alloy (NiBSi and In625).

Since the thermal conductivity, which is temperature dependent, is included in the equation (A.14) to calculate $T_{mp}$, iterative method has been applied to combine the values of $k(T)$ and $T_{mp}$.

With this technique, melt pool temperature in different processing conditions has been estimated. To prove the quality of the estimation, the melt pool temperature has been plotted versus the wetting angle $\alpha_{wet}$ (Figure A.14,left) and the aspect ratio (Figure A.14,right). Indeed, the temperature of the melt pool should be correlated to the geometry of the final clad: a higher melt pool temperature generates higher wettability of the substrate surface by the liquid metal, leading consequently to a lower wetting angle.
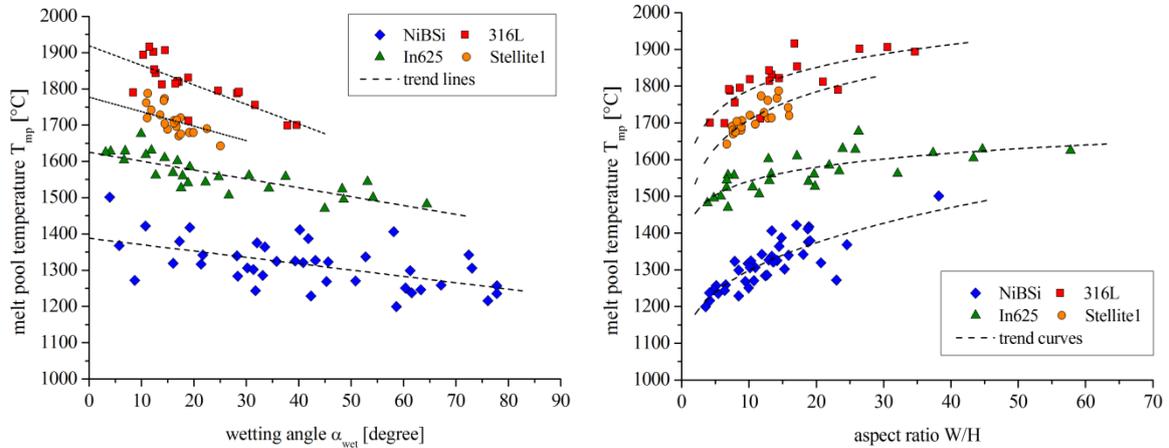


*Figure A.14. Estimated melt pool temperature as a function of the wetting angle and the aspect ratio respectively.*

When compared to the quantity $\alpha_{wet}$, it can be seen that the molten pool temperature decreases on increasing the wetting angle (Figure A.14), thus confirming the appreciable result in temperature estimation.

In addition, according to the different cladding materials used, different correlations were revealed. This is mainly due to the different solidus temperature of the materials, which strongly affects the calculation of $T_{mp}$.

Together with the wetting angle, substrate wettability can be evaluated from the aspect ratio of the clad. These two quantities are in fact correlated by equation

$$\frac{W}{H} = \frac{2}{tan\left(\frac{\alpha_{wet}}{2}\right)} \qquad (A.19)$$

which approximates the variation of the *W/H* ratio as a function of $\alpha_{wet}$ (Figure A.15).
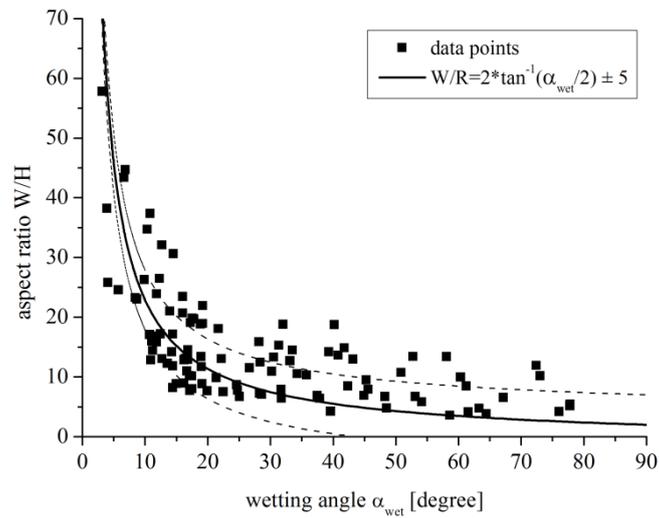


*Figure A.15. Aspect ratio values as a function of the wetting angle plotted together with equation (A.19).*

Consequently, for the same reason, an increase in the aspect ratio value is justified by an increase in the melt pool temperature (Figure A.14,right): higher wettability of the substrate produces a wider clad, that is the reason of the increased aspect ratio.

# Appendix 7

# Specific heat

Heat capacities of the powders and substrate used in the energetic model have been calculated using the Neumann and Kopp's rule. This rule states that for a given alloy, the heat capacity $c_p$ per unit mass (expressed in $Jg^{-1}K^{-1}$) can be calculated from the equation

$$c_p = \sum_{i=1}^{N} c_{p,i} \cdot f_i \qquad (A.20)$$

where $N$ is the total number of alloy constituents and $c_{p,i}$ and $f_i$ are the heat capacity and the mass fraction of the $i$-th constituent respectively.

Since heat capacity is a temperature-dependent quantity, specific heats of different elements at different temperatures have been used, assuming linear variation between the data points available in literature [162,163].

Calculated heat capacities are reported in Figure A.16.
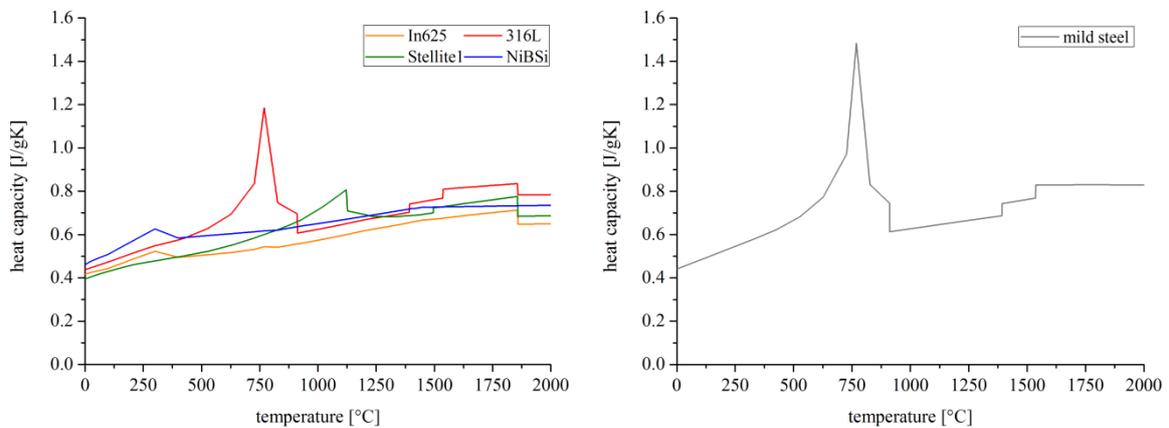


*Figure A.16. Estimated heat capacities of the powder materials (left) and the substrate material (right).*

# References

1. Holmberg, K., and A. Matthews, *Coatings tribology: properties, techniques and applications in surfaces engineering*. **2009**, Oxford, UK: Elsevier.
2. Davis, J.R., *Surface engineering for corrosion and wear resistance*. **2001**, Materials Park, Ohio, USA: ASM International.
3. Peterson, M.B., and W.O. Winer, *Wear control handbook*. **1980**, New York, NY, USA: American society of mechanical engineers.
4. Strafford, K.N., P.K. Datta, and C.G. Googan, *Coatings and surface treatment for corrosion and wear resistance*. **1984**, Chichester, UK: Horwood.
5. Rickerby, D.S., and A. Matthews, *Advanced surface coatings: a handbook of surface engineering*. **1991**, Glasgow; London, UK: Blackie.
6. Mayr, P., *Surface engineering*. **1993**, Oberursel, D: DGM Informationsgesellschaft.
7. Stevens, K., *Surface engineering to combat wear and corrosion*. **1997**, London, UK: Institute of Materials.
8. Tuominen, J., *Engineering coatings by laser cladding – The study of wear and corrosion properties*. Ph.D. Thesis, Tampere University of Technology. **2009**, Tampere, Finland.
9. Vilar, R., *Laser alloying and laser cladding*, in *Lasers in materials science*, R.P. Agarwala, **1999**, Trans Tech Publications Ltd: Switzerland. p. 229-252.
10. Steen, W.M., and J. Mazumder, *Laser material processing*. **2010**, London, UK: Springer-Verlag.
11. Toyserkani, E., A. Khajepour, and S. Corbin, *Laser cladding*. **2005**, Boca Raton, Florida, USA: CRC Press LLC.
12. Schneider, M., *Laser cladding with powder. Effect of same machining parameters on clad properties*. Ph.D. Thesis, University of Twente. **1998**, Enschede, The Netherlands.
13. Avco Everett Research Laboratory Inc. 1976. US Patent n. 3 952 180.
14. MacIntyre, R.M., *Laser hardfacing of gas turbine blade shroud interlocks*. in Proceedings of the 1st International Conference Lasers in Manufacturing. **1983**. Bedford.
15. MacIntyre, R.M., *Laser hard-surfacing of turbine blade shroud interlocks*. in Proceedings of the 2nd International Conference of Lasers in Materials Processing. **1983**. Metals Park.
16. MacIntyre, R.M., *The use of lasers in Rolls-Royce*. in Proceedings of the NATO ASI Laser Surface Treatment of Metals. **1986**. Dordrecht.
17. Doran, S.B., *The laser where flexibility ultimately means economy*. in Production Magazine. **1987**.
18. Ion, J.C., *Laser processing of engineering materials. Principles, procedures and industrial applications*. **2005**, Burlington, MA, USA: Elsevier Butterworth-Heinemann.

19. Mazumder, J., and E. Stiles, *Fabrication of designed materials using direct metal deposition*. in Proceedings of ICALEO. **2000**. Dearborn.

20. Fessler, J.R., R. Merz, A.H Nickel, and F.B. Prinz, *Laser deposition of metals for shape deposition manufacturing*. in Proceedings of the Solid Freeform Fabrication Symposium. **1996**. Austin.

21. Mazumder, J., J. Choi, K. Nagarathnam, J. Koch, and D. Hetzner, *The direct metal deposition of H13 tool steel for 3-D components*. JOM, **1997**. 49(5): p. 55-60.

22. Jiang, W., R. Nair, and P. Molian, *Functionally graded mold inserts by laser-based flexible fabrication: processing modeling, structural analysis, and performance evaluation*. Journal of Materials Processing Technology, **2005**. 166: p. 286–293.

23. Liu, W., and J.N. DuPont, *Fabrication of functionally graded TiC/Ti composites by Laser Engineered Net Shaping*. Scripta Materialia, **2003**. 48: p. 1337–1342.

24. Shin, K.-H., H. Natu, D. Dutta, and J. Mazumder, *A method for the design and fabrication of heterogeneous objects*. Materials and Design, **2003**. 24: p. 339–353.

25. Yakovlev, A., E. Trunova, D. Grevey, M. Pilloz, and I. Smurov, *Laser-assisted direct manufacturing of functionally graded 3D objects*. Surface & Coatings Technology, **2005**. 190: p. 15–24.

26. Yadroitsev, I., P. Bertrand, B. Laget, and I. Smurov, *Application of laser assisted technologies for fabrication of functionally graded coatings and objects for the International Thermonuclear Experimental Reactor components*. Journal of Nuclear Materials, **2007**. 362: p. 189–196.

27. Arcella, F.G., and F.H. Froes, *Producing titanium aerospace components from powder using laser forming*. JOM, **2000**. 52(5): p. 28-30.

28. Capshaw, B., *Improved performance for motorsports applications through laser powder deposition technology*. in Proceedings of International Conference on Metal Powder Deposition for Rapid Manufacturing. **2002**. San Antonio.

29. Xue, L., and M. Islam, *Free-form laser consolidation for producing functional metallic components*. in Proceedings of ICALEO. **1998**. Orlando.

30. Xue, L., J.Y. Chen, M. Islam, J. Pritchard, D. Manente, and S. Rush, *Laser consolidation of Ni-base IN-738 superalloy for repairing gas turbine blades*. in Proceedings of ICALEO. **2000**. Dearborn.

31. Backes, G., E.W. Kreutz, A. Gasser, E. Hoffmann, S. Keutgen, K. Wissenbach, and R. Poprawe, *Laser-shape reconditioning and manufacturing of tools and machine parts*. in Proceedings of ICALEO. **1998**. Florida.

32. Mazumder, J., J. Choi, K. Nagarathnam, J. Koch, and D. Hetzner, *The direct metal deposition of H13 tool steel for 3D components*. JOM, **1997**. 49(5): p. 55-60.

33. Xue, L., and M. Islam, *Laser consolidation – a novel one-step manufacturing process from CAD models to net-shape functional components*. in Proceedings of International Conference on Metal Powder Deposition for Rapid Manifacturing. **2002**. Providence.

34. Hu, Y.P., C.W. Chen, and K. Mukherjee, *Development of a new laser cladding process for manufacturing cutting and stamping dies*. Journal of Materials Science, **1998**. 33(5): p. 1287-1292.

35. Marchione, R., *Industrial applications of laser cladding*. in Proceedings of the International Conference on Metal Powder Deposition for Rapid Manufacturing. **2002**. Providence.

36. Bohrer, M., H. Basalka, W. Birner, K. Emiljanow, M. Goede, and S. Czerner, *Turbine blade repair with laser powder fusion welding and shape recognition*. in Proceedings of the

International Conference on Metal Powder Deposition for Rapid Manufacturing. **2002**. Providence.

37. Gaumann, M., S. Henry, F. Cleton, J.-D. Wagniere, and W. Kurz, *Epitaxial laser metal forming: analysis of microstructure formation*. Materials Science and Engineering A, **1999**. 271(1/2): p. 232-241.

38. Bruck, G.J., *Fundamentals and industrial applications of high power laser beam cladding*, Proceedings of SPIE. **1988**. Dearborn.

39. Jasim, K.M., R.D. Rawlings, and D.R.F. West, *Thermal barrier coatings produced by laser cladding*. Journal of Materials Science, **1990**. 25: p. 4943-4948.

40. Axen, N., and K.-H. Zum Gahr, *Abrasive wear of TiC-steel composite clad layers on tool steel*. Wear, **1992**. 157: p. 189-201.

41. De Damboreana, J., and A.J. Vazquez, *Laser cladding of high-temperature coatings*. Journal of Materials Science, **1993**. 28: p. 4775-4780.

42. Beidi, Z., Z. Xiaoyan, T. Zengyi, Y. Shuguo, and C. Kun, *Coarse cemented WC particle ceramic-metal composite coatings produced by laser cladding*. Wear, **1993**. 170: p. 161-166.

43. Wang, P.-Z., Y.-S. Yang, G. Ding, J.-X. Qu, and H.-S. Shao, *Laser cladding coating against erosion-corrosion wear and its application to mining machine parts*. Wear, **1997**. 209: p. 96-109.

44. Carvalho, P.A., A.M. Deus, R. Colaco, and R. Vilar, *Laser alloying of zinc with aluminum: solidification behavior*. Acta Materialia, **1998**. 46(5): p. 1781-1792.

45. Katipelli, L.R., A. Agarwal, N.B. Dahotre, *Laser surface engineered TiC coating on 6061 Al alloy: microstructure and wear*. Applied Surface Science, **2000**. 153: p. 65–78.

46. Dubourg, L., H. Pelletier, D. Vaissiere, F. Hlawka, and A. Cornet, *Mechanical characterisation of laser surface alloyed aluminium–copper systems*. Wear, **2002**. 253: p. 1077–1085.

47. Zhang, D.-W., and T.C. Lei, *The microstructure and erosive–corrosive wear performance of laser-clad Ni–Cr$_3$C$_2$ composite coating*. Wear, **2003**. 255: p. 129–133.

48. Dubourg, L., D. Ursescu, F. Hlawka, and F. Hlawka, *Laser cladding of MMC coatings on aluminium substrate: influence of composition and microstructure on mechanical properties*. Wear, **2005**. 258: p. 1745–1754.

49. Rajput D., K. Lansford, L. Costa, and W. Hofmeister, *Molybdenum-on-chromium dual coating on steel*. Surface & Coatings Technology, **2009**. 203: p. 1281–1287.

50. Ready, J.F., *LIA handbook of laser materials processing*. **2001**, Orlando, FL, USA: Magnolia Publishing, Inc.

51. Hoadley, A.F.A., and M. Rappaz, *A thermal model of laser cladding by powder injection*. Metallurgical Transactions B, **1992**. 23B: p. 631-642.

52. Soares, O.D.D., and M. Perez-Amor, *Applied laser tooling*. **1987**, Dordrecht, The Netherlands: Martinus Nijhoff Publishers.

53. Vuoristo, P., J. Tuominen, and J. Nurminen, *Laser coating and thermal spraying - process basics and coating properties*. in Proceedings of the International Thermal Spray Conference. **2005**. Kokkola.

*54.* Hofman, J.T., *Development of an observation and control system for industrial laser cladding*. Thesis, University of Twente. **2009**, Enschede, The Netherlands.

55. Costa Rodrigues, G., H. Vanhove, and J.R. Duflou, *Direct diode lasers for industrial laser cutting: a performance comparison with conventional fiber and CO$_2$ technologies*. Physics Procedia, **2014**. 56: p. 901-908.

56.  Zervas, M.N., and C.A. Codemard, *High power fiber lasers: a review*. IEEE Journal of Selected Topics in Quantum Electronics, **2014**. 20(5).

57.  Sarin, V.K., *Comprehensive hard materials*. **2014**, Oxford, UK: Elsevier.

58.  Yaedu, A.E., and A.S.C.M. D'Oliveira, *Cobalt based alloy PTA hardfacing on different substrate steels*. Materials Science and Technology, **2005**. 21(4): p. 459-466.

59.  Li, L.J., and J. Mazumder, *A study of the mechanism of laser cladding processes*. in Proceedings of the Symposium Laser Processing of Materials. **1984**. Los Angeles.

60.  Powell, J., P.S. Henry, and W.M. Steen, *Laser cladding with preplaced powder: analysis of thermal cycling and dilution effects*. Surface Engineering, **1988**. 4(2): p. 141-149.

61.  Gedda, H., A. Kaplan, and J. Powell, *Melt-solid interactions in laser cladding and laser casting*. Metallurgical and Materials Transactions, **2005**. 36B(5): p. 683-689.

62.  Gedda, H., J. Powell, G. Wahlstrom, W.-B. Li, H. Engstrom, and C. Magnusson, *Energy redistribution during $CO_2$ laser cladding*. Journal of Laser Applications, **2002**. 14(2): p. 78-82.

63.  Lin, J., and Hwang, B.-C., *Coaxial laser cladding on an inclined substrate*. Optics & Laser Technology, **1999**. 31: p. 571-578.

64.  Lin, J., *A simple model of powder catchment in coaxial laser cladding*. Optics & Laser Technology, **1999**. 31: p. 233-238.

65.  Picasso, M., and M. Rappaz, *Laser-powder-material interactions in the laser cladding process*. Journal de Physique IV, **1994**. C4: p. 27-33.

66.  Amara, E.H., F. Hamadi, L. Achab, and O. Boumia, *Numerical modelling of the laser cladding process using a dynamic mesh approach*. Journal of Achievements in Materials and Manufacturing Engineering, **2006**. 15(1-2): 100-106.

67.  Hoadley, A.F.A., A. Frenk, and C.F. Marsden, *A process overview of laser hardfacing*. in Surface engineering – processes and applications, K.N. Strafford, R.St.C. Smart, I. Sare, C. Subramanian, **1995**, Technomic Publishing Company, Inc: Lancaster (USA). p. 171-186.

68.  Picasso, M., C.F. Marsden, J.-D. Wagniere, A. Frenk, and M. Rappaz, *A simple but realistic model for laser cladding*. Metallurgical and Materials Transactions B, **1994**. 25B: p. 281-291.

69.  Becker, R. and G. Sepold, *Micro-coating by a laser powder feed process*. Advanced Powder Technology, **1991**. 2(3): p. 181-189.

70.  Liu, C.-Y., and J. Li, *Thermal processes of a powder particle in coaxial laser cladding*. Optics & Laser Technology, **2003**. 35: p. 81–86.

71.  Haferkamp, H., H. Schmidt, J. Gerken, and T. Püster, *Application of laser powder cladding and the risk of residual powder*. in Proceedings of ECLAT. **1994**. Bremen-Vegesack.

72.  Marsden, C.F., A. Frenk, J.D. Wagniere, and R. Dekumbis, *Effects of injection geometry on laser cladding*. in Proceedings of ECLAT. **1990**. Coburg.

73.  Moures, F., E. Cicala, P. Sallamand, D. Grevey, B. Vannes, and S. Ignat, *Optimisation of refractory coatings realised with cored wire addition using a high-power diode laser*. Surface & Coatings Technology, **2005**. 200: p. 2283–2292.

74.  Nurminen, J., *Hot-wire laser cladding*. Thesis, Tampere University of Technology. **2008**, Tampere, Finland.

75.  Wiklund, G., and J. Flinkfeldt, *Laser cladding combined with MIG-equipment*. in Proceedings of NOLAMP. **1997**. Luleå.

76.  Syed, W.U.H., and L. Li, *Effects of wire feeding direction and location in multiple layer diode laser direct metal deposition*. Applied Surface Science, **2005**. 248: p. 518–524.

77. Kim, J.-D., and Y. Peng, *Plunging method for Nd:YAG laser cladding with wire feeding*. Optics and Lasers in Engineering, **2000**. 33: p. 299-309.

78. Yelistratov, A., and F. Sciammarella, *Laser surfacing with wire feeding*. Welding Journal, **2005**. 84(12): p. 36-39.

79. Yelistratov, A., *Direct diode laser deposition with strip feeding*. Welding Design & Fabrication, **2006**. 79(10).

80. Bouaifi, B., and J. Bartzsch, *Surface protection by laser beam deposition with hot wire addition*. Welding and Cutting, **1993**. 4: p. E70-E72.

81. Nurminen, J., J. Riihimäki, J. Näkki, and P. Vuoristo, *Comparison of laser cladding with powder and hot and cold wire techniques*. in Proceedings of ICALEO. **2006**. Scottsdale.

82. Hinse-Stern, A., D. Burchards, and D.L. Mordike, *Laser cladding with preheated wires*. in Proceedings of ECLAT. **1992**. Göttingen.

83. Wetzig, A., B. Brenner, V. Fux, and E. Beyer, *Induction assisted laser-cladding a new and effective method for producing high wear resistant coatings on steel components*. in Proceedings of ICALEO. **1998**. Orlando.

84. Beyer, E., B. Brenner, and S. Nowotny, *Overview of hybrid technology*. in Proceedings of PICALO. **2004**. Orlando.

85. Zhou, Z., H. Shirasawa, N. Eguchi, and A. Ohmori, *Microstructures and characterization of zirconia-yttria coatings formed in laser and hybrid spray process*. Journal of Thermal Spray Technology, **1999**. 8(3): p 405-413.

86. Antou, G., G. Montavon, F. Hlawka, A. Cornet, C. Coddet, and F. Machi, *Modification of ceramic thermal spray deposit microstructures implementing in situ laser remelting*. Surface and Coating Technology, **2003**. 172: p. 279-290.

87. Suutala, J., J. Tuominen, and P. Vuoristo, *Laser-assisted spraying and laser treatment of thermally sprayed coatings*. Surface and Coating Technology, **2006**. 201: p. 1981-1987.

88. Miyamoto, I., S. Fujimori, and K. Itakura, *Mechanism of dilution in laser cladding with powder feeding*. in Proceedings of ICALEO. **1997**. San Diego.

89. Pinkerton, A.J., and L. Li, *Multiple-layer cladding of stainless steel using a high-powered diode laser: an experimental investigation of the process characteristics and material properties*. Thin Solid Films, **2004**. (453–454): p. 471–476.

90. Lalas, C., K. Tsirbas, K. Salonitis, and G. Chryssolouris, *An analytical model of the laser clad geometry*. International Journal of Advanced Manufacturing Technology, **2007**. 32: p. 34-41.

91. De Oliveira, U., V. Ocelik, and J.Th.M. De Hosson, *Analysis of coaxial laser cladding processing conditions*. Surface & Coatings Technology, **2005**. 197: p. 127–136.

92. Ocelik, V., U. De Oliveira, M. De Boer, and J.Th.M. De Hosson, *Thick Co-based coating on cast iron by side laser cladding: analysis of processing conditions and coating properties*. Surface & Coatings Technology, **2007**. 201: p. 5875–5883.

93. Kumar, S., S. Roy, C.P. Paul, and A.K. Nath, *Three-dimensional conduction heat transfer model for laser cladding process*. Numerical Heat Transfer, Part B, **2008**. 53: p. 271-287.

94. Kaplan, A.F.H., and G. Groboth, *Process analysis of laser beam cladding*. Journal of Manufacturing Science and Engineering, **2001**. 123: p. 609-614.

95. Nan, L., W. Liu, and K. Zhang, *Modeling for laser-material interaction to predict and control the cross sectional area of coaxial laser cladding with powder*. in Proceedings of the International conference on Advanced Design and Manufacture. **2006**. Harbin.

96. Pelletier, J.M., M.C. Sahour, M. Pilloz, and A.B. Vannes, *Influence of processing conditions on geometrical features of laser claddings obtained by powder injection*. Journal of Materials Science, **1998**. 28: p. 5184-5188.

97. Sun, S., Y. Durandet, and M. Brandt, *Correlation between melt pool temperature and clad formation in pulsed and continuous wave Nd:YAG laser cladding of Stellite 6*. Proceedings of PICALO. **2004**. Melbourne.

98. Hu, Y., C, Chen, and K, Mukherjee, *Innovative laser-aided manufacturing of patterned stamping and cutting dies: processing parameters*. Malerials and Manufacturing Processes, **1998**. 13(3): p. 369-387.

99. Frenk, A., M. Vandyoussefi, J.-D. Wagniere, A. Zyrd and W. Kurz, *Analysis of the laser-cladding process for Stellite on steel*. Metallurgical and Materials Transactions B, **1997**. 28B: p. 501-508.

100. Qian, M., L.C. Lim, Z.D. Chen, and W.L. Chen, Parametric studies of laser cladding processes. Journal of Materials Processing Technology, 1997. 63: p. 590-593.

101. Felde, I., T. Reti, K. Zoltan, L. Costa, R. Colaco, R. Vilar, and B. Verö, *A simple technique to estimate the processing window for laser clad coatings*. in Proceedings of the International Surface Engineering Congress and IFHTSE Congress. **2002**. Columbus.

102. Bruck, G.J., *High-power laser beam cladding*. JOM, **1987**. 39(2): p. 10-13.

103. Fathi, A., E. Toyserkani, A. Khajepour, and M. Durali, *Prediction of melt pool depth and dilution in laser powder deposition*. Journal of Physics D: Applied Physics, **2006**. 39: p. 2613-2623.

104. Del Val, J., R. Comesaña, F. Lusquiños, M. Boutinguiza, A. Riveiro, F. Quintero, and J. Pou, *Laser cladding of Co-based superalloy coatings: comparative study between Nd:YAG laser and fibre laser*. Surface & Coatings Technology, **2010**. 204: p. 1957–1961.

105. Komvopoulos, K., and K. Nagarathnam, *Processing and characterization of laser-cladded coating materials*. Journal of Engineering Materials and Technology, **1990**. 112: p. 131-143.

106. Steen, W.M., and C.G.H. *Courtney, Hardfacing of Nimonic 75 using 2kW continuous-wave $CO_2$ laser*. Metals Technology, **1980**. 7(6): p. 232-237.

107. Hofman, J.T., D.F. de Lange, B. Pathiraj and J. Meijer, *FEM modelling and experimental verification for dilution control in laser cladding*. Journal of Materials Processing Technology, **2011**. 211: p. 187-196.

108. Y. Huang, *Characterization of dilution action in laser-induction hybrid cladding*. Optics & Laser Technology, **2011**. 43: p. 965-973.

109. Pickin, C.G., S.W. Williams, and M. Lunt, *Characterisation of the cold metal transfer (CMT) process and its application for low dilution cladding*. Journal of Materials Processing Technology, **2011**. 211: p. 496-502.

110. Zhao, G., C. Cho, and J.-D. Kim, *Application of 3-D finite element method using Lagrangian formulation to dilution control in laser cladding process*. International Journal of Mechanical Sciences, **2003**. 45: p. 777–796.

111. Salehi, D., and M. Brandt, *Melt pool temperature control using LabVIEW in Nd:YAG laser blown powder cladding process*. International Journal of Advance Manufacturing Technology, **2006**. 29: p. 273-278.

112. Majumdar, J.D., and I. Manna, *Laser-assisted fabrication of materials*. **2013**, Berlin, D: Springer-Verlag.

113. Drezet, J.-M., S. Pellerin, C. Bezencon, and S. Mokadem, *Modelling the Marangoni convection in laser heat treatment*. Journal de Physique IV, **2004**. 120: p. 299-306.

114. Sheikh, M.A., *Modelling & simulation of laser material processing: predicting melt pool geometry and temperature distribution*. in Proceedings of International Conference MS'07. **2007**. Kolkata.

115. Frenk, A., and W. Kurz, *High speed laser cladding: solidification conditions and microstructure of a cobalt-based alloy*. Materials and Science Engineering, **1993**. A173: p. 339-342.

116. Zhou, S., Y. Huang, X. Zeng, and Q. Hu, *Microstructure characteristics of Ni-based WC composite coatings by laser induction hybrid rapid cladding*. Materials Science and Engineering A, **2008**. 480: p. 564–572.

117. Mohanty, P.S., and J. Mazumder, *Solidification behavior and microstructural evolution during laser beam–material interaction*. Metallurgical and Materials Transactions B, **1998**. 29B: 1269-1279.

118. Huang, F.X., Z.H. Jiang, X.M. Liu, J.S. Lian, and L. Chen, *Effects of process parameters on microstructure and hardness of layers by laser cladding*. ISIJ International, **2011**. 51(3): p. 441–447.

119. Böllinghaus, T., and H. Herold, *Hot cracking phenomena in welds*. **2005**, Berlin, D: Springer-Verlag.

120. Katayama, S., *Handbook of laser welding technologies*. **2013**, Cambridge, UK: Woodhead Publishing Limited.

121. Fu, Y., A. Loredo, B. Martin, and A.B. Vannes, *A theoretical model for laser and powder particles interaction during laser cladding*. Journal of Materials Processing Technology, **2002**. 128: p. 106-112.

122. Gedda, H., *Laser cladding: an experimental and theoretical investigation*. Ph.D. Thesis, Luleå University of Technology. **2004**, Luleå, Finland.

123. Partes, K., T. Seefeld, G. Sepold, and F. Vollertsen, *Increased efficiency in laser cladding by optimization of beam intensity and travel speed*. in Proceedings of SPIE, **2005**. 6157: p. O1-O11.

124. Marsden, C.F., A. Frenk, and J.-D. *Wagniere, Power absorption during the laser cladding process*. in Proceedings of ECLAT. **1992**. Göttingen.

125. Bergström, D., *The absorption of laser light by rough metal surfaces*. Ph.D. Thesis, Luleå University of Technology. **2008**, Luleå, Finland.

126. Mahrle, A., and E. Beyer, *Theoretical aspects of fibre laser cutting*. Journal of Applied Physics D, **2009**. 42: 175507(9pg).

127. Ordal, M.A., R.J. Bell, R.W. Alexander Jr., L.A. Newquist, and M.R. Querry, *Optical properties of Al, Fe, Ti, Ta, W, and Mo at submillimeter wavelengths*. Applied Optics, **1988**. 27(6): p. 1203-1209.

128. Ollier, B., N. Pirch, E.W. Kreutz, and H. Schlüter, *Cladding with laser radiation: properties and analysis*. in Proceedings of ECLAT. **1992**. Göttingen.

129. Gutu, I., C. Petre, I.N. Mihailescu, M. Taca, E. Alexandrescu, and I. Ivanov, *Surface treatment with linearly polarized laser beam at oblique incidence*. Optics & Laser Technology, **2002**: 34: p. 381–388.

130. Pinkerton, A.J., and L. Li, *An analytical model of energy distribution in laser direct metal deposition*. in Proceedings of The Institution of Mechanical Engineers Part B - Journal of Engineering Manufacture, **2004**. 218: p. 363-374.

131. Kou, S., *Welding metallurgy*. **2003**, Hoboken, New Jersey, USA: John Wiley & Sons, Inc.

132. Maiman, T.H., *The laser odyssey*. **2000**, Blaine, WA, USA: Laser Press.

133. Patel, C.K.N., *Interpretation of CO2 optical master experiments*. Physical Review Letters, **1964**. 12(21): p. 588-590.

134. Geusic, J.E., H.M. Marcos, and L.G. van Uitert, *Laser oscillations in Nd-doped yttrium aluminum, yttrium gallium and gadolinium garnets*. Applied Physics Letters, **1964**. 4(10): p. 182-184.

135. Anon, *Laser "punches" holes in diamond wire-drawing dies*. Laser Focus, **1966**. 2(1): p. 4-7.

136. Platte, W.N, and J.F. Smith, *Laser techniques for metals joining*. Welding Journal Research Supplement, **1963**. 42(11): p. 481s-489s.

137. Sullivan, A.B.J., and P.T. Houldcroft, *Gas-jet laser cutting*. British Welding Journal, **1967**. 14(8): p. 443-445.

138. DeMichelis, C., *Laser interaction with solids – a bibliographical review*. IEEE Journal of Quantum Eletronics, **1970**. QE-6(10): p. 630-641.

139. Caterpillar Tractor Co., *Method and apparatus for fusibly bonding a coating material to a metal article*. **1977**, GB Patent no. 1 482 044.

140. Davis, S.J., K.G. Watkins, G. Dearden, E. Fearon and J. Zeng, *Optimum deposition parameters for the direct laser fabrication (DLF) of quasi-hollow structures*. in Proceedings of Photon Conference. **2006**. Manchester.

141. Van de Hulst, H.C., *Light scattering by small particles*. **1981**, New York, NY, USA: Dover Publications, Inc.

142. Poirier, D.R., and G.H. Geiger, *Transport phenomena in materials processing*. **1994**, Warrendale, PA, USA: The Minerals, Metals & Materials Society.

143. *ASM Handbook Vol. 2, Properties and selection: irons, steels, and high performance alloys*. **2005**, Materials Park, Ohio, USA: ASM International.

144. Davis, J.R., *Nickel, cobalt and their alloys*. **2000**, Materials Park, Ohio, USA: ASM International.

145. Tinoco, J., *On the spray forming of metals, the formation of porosity and the heat evolution during solidification*. Ph.D. Thesis, Casting of Metals Royal Institute of Technology. **2003**, Stockholm, Sweden.

146. Zanzarin, S., *Laser cladding di polvere di superlega e acciai inossidabili*. Master Thesis, University of Trento. **2012**, Trento, Italy.

147. Betteridge, W., *Cobalt and its alloys*. **1982**, New York, NY, USA: Wiley.

148. Huang, F.X., Z.H. Jiang, X.M. Liu, J.S. Lian and L. Chen, *Effects of process parameters on microstructure and hardness of layers by laser cladding*. ISJI International, **2011**. 51: p. 441 – 447.

149. Kou, S., *Welding metallurgy*. **2003**, New Jersey, USA: John Wiley & Sons.

150. Abioye, T.E., *Laser deposition of Inconel 625/Tungsten Carbide composite coatings by powder and wire feedstock*. Ph.D. Thesis, University of Nottingham. **2014**, Nottingham, England.

151. DuPont, J.N., *Solidification of an Alloy 625 overlay*. Metallurgical and Materials Transactions A, **1996**. 27A: p. 3612-3620.

152. Floreen, S., G.E. Fuchs, and W.J. Yang, *The metallurgy of Alloy 625*. in Proceedings of the 4th International Symposium on Superalloys 718, 625, 706 and Derivatives. **1994**. Pittsburgh.

153. Birks, N., and G.H. Meier, *Introduction to high temperature oxidation of metals*. **1983**, London, England: Edward Arnold.

154. Kofstad, P., *High temperature corrosion*. **1988**, London, England: Elsevier Applied Science.

155. Molinari, A., G. Straffelini, A. Tomasi, A. Biggi, and G. Corbo, *Influence of microstructure and chromium content on oxidation behaviour of spin cast high speed steels*. Materials Science and Technology, **2001**. 17: p. 425-430.

156. Molinari, A., G. Straffelini, A. Tomasi, A. Biggi, and G. Corbo, *Oxidation behaviour of ledeburitic steels for hot rolls*. Materials Science and Engineering, **2000**. A280: p. 255-262.

157. Seger, R., *Effect of tungsten carbides properties of overlay welded WC/NiSiB composite coatings*. Master Thesis, KTH Royal Institute of Technology. **2004**, Stockholm, Sweden.

158. Diabb, J., A. Juarez-Hernandez, R. Colas, A.G. Castillo, and E. Garcia-Sanchez, *Boron influence on wear resistance in nickel-boron alloys*. Wear, **2009**. 267: p. 550-555.

159. Picasso, M., and A.F.A. Hoadley, *Finite element simulation of laser surface treatments including convection in the melt pool*. International Journal of Numerical Methods for Heat & Fluid Flow, **1994**. 4: p. 61-83.

160. Johnson, P.B., and R.W. Christy, *Optical constants of transition metals: Ti, V, Cr, Mn, Fe, Co, Ni, and Pd*. Physical Review B, **1974**. 9: p. 5056-5070.

161. Nishi, T., H. Shibata, Y. Waseda, and H. Ohta, *Thermal conductivities of molten iron, cobalt, and nickel by laser flash method*. Metallurgical and Materials Transactions A, **2003**. 34(12): p. 2801-2807.

162. http://kinetics.nist.gov/janaf/. Internet. **2013**. *National Institute of Standards and Technology, Thermochemical Tables*.

163. Iida, T., and R.I.L. Guthrie, *The physical properties of liquid metals*. **1988**, Oxford, England: Clarendon.

# Congresses

34th Convegno Nazionale AIM; Trento (Italy), November 7th – 9th, 2012. "Studio preliminare del processo di laser cladding di polvere di acciaio inossidabile". Oral presentation.

24th Convegno Nazionale Trattamenti Termici; Piacenza (Trento), October 17th – 18th, 2013. "Studio della diluizione di rivestimenti di stellite su acciaio al carbonio prodotti per laser cladding di polveri". Oral presentation.

33rd International Congress on Applications of Lasers & Electro-Optics; San Diego (USA), October 19th – 23rd, 2014. "Study of carbide dissolution into the matrix during laser cladding of carbon steel plate with tungsten carbides-stellite powders". Poster presentation.

Conference on Heat Treatment 2015 and the 22nd IFHTSE Congress; Venezia (Italy), May 20th – 22nd, 2015. "Influence of processing parameters on geometrical features of clad produced by high power diode laser cladding of carbon steel with different powders". Poster presentation.

# Publications

Zanzarin S., L. Maines, S. Bengtsson, and A. Molinari, *Studio preliminare del processo di laser cladding di polvere di acciaio inossidabile*. in Proceedings del 34° Convegno Nazionale AIM. **2012**. Trento.

Zanzarin S., L. Maines, S. Bengtsson, and A. Molinari, *Studio della diluizione di rivestimenti di stellite su acciaio al carbonio prodotti per laser cladding di polveri*. in Proceedings del 24° Convegno Nazionale Trattamenti Termici. **2013**. Piacenza.

Zanzarin S., S. Bengtsson, L. Maines, and A. Molinari, *Influence of heat input and powder density on energetic efficiency of high power diode laser cladding of carbon steel with AISI316L powder*. La Metallurgia Italiana, **2014**. 9: p. 3 - 9.

Zanzarin S., S. Bengtsson, and A. Molinari, *Study of carbide dissolution into the matrix during laser cladding of carbon steel plate with tungsten carbides-stellite powders*. Journal of Laser Applications, **2015**. 27: p. S29209 - S29216.

Zanzarin S., S. Bengtsson, and A. Molinari, *Influence of processing parameters on geometrical features of clad produced by high power diode laser cladding of carbon steel with different powders*. in Proceedings of the European Conference on Heat Treatment 2015 and the 22nd IFHTSE Congress. **2015**. Venezia.

Zanzarin S., S. Bengtsson, and A. Molinari, *Study of dilution in laser cladding of a carbon steel substrate with Co alloy powders*. Powder Metallurgy, in press.

# Acknowledgments

A thought to Sven, Mattias and all the Höganäs team for the opportunity and the support.

A thought to Professor Molinari, for his teachings.

A thought to Lorena, Gloria, Luca, and Professor Pellizzari, for their help.

A thought to Cinzia and her family, for everything.

A thought to my labmates, good friends. A thought to Lorena, for editing.

A thought to Luca, my mentor.

A thought to my family.

A thought to all my friends, for being so special. A thought to Ilaria.